Design and development of bismuth-based ternary oxides and their hybrid composites for solar-driven photocatalytic degradation of pharmaceutical pollutants

Thèse

Rokesh Karuppannan

Doctorat en génie chimique
Philosophiæ doctor (Ph. D.)

Québec, Canada

Design and development of bismuth-based ternary oxides and their hybrid composites for solar-driven photocatalytic degradation of pharmaceutical pollutants

Thèse

Rokesh Karuppannan

Sous la direction de

Trong-On Do, Directeur de recherche

Résumé

La technique de photocatalyse solaire offre une solution prometteuse pour une élimination efficace des polluants pharmaceutiques émergents comme les antibiotiques dans les eaux usées. Les matériaux photocatalytiques à base de semi-conducteurs jouent un rôle crucial dans la dégradation complète de ces nouveaux polluants pharmaceutiques. À ce propos, de nouveaux photocatalyseurs nanocomposites ont montré une performance catalytique importante par rapport aux photocatalyseurs classiques dans la dégradation des antibiotiques dans l'eau. Ces photocatalyseurs nanocomposites surmontent des défis notamment une photo-absorption insuffisante, une mauvaise séparation de charge, un transfert de charge lent, une recombinaison de charge importante, une mauvaise réaction de surface, une stabilité faible et une récupération difficile. Dans ce contexte, nous avons développé des hybride matériaux photocatalytiques nanostructuré et nanocomposite tout en exploitant leur performance pour la dégradation des antibiotiques sous la lumière solaire.

Un nouveau matériau de pérovskite ferroélectrique à base de bismuthate de calcium ($CaBiO_3$) nanostructuré avec une disproportion de différentes multicharges Bi^{3+} et Bi^{5+}, a été développé via des méthodes de complexation de glycine et d'échange d'ions. La disproportion efficace obtenue de charge Bi^{3+}/Bi^{5+} et l'arrangement bien organisé du cristal octaédrique de BiO_6 ont offert une photo-absorbance efficace du visible ainsi qu'une photogénération et une séparation importante de porteurs de charge dans $CaBiO_3$. En outre, les matériaux $CaBiO_3$ développés présentent une nanostructure avec une surface spécifique plus élevée qui offre des propriétés de surface améliorées en faveur de la réaction catalytique. De plus, les matériaux à base de $CaBiO_3$ sont étudiés pour la dégradation des antibiotiques de ciprofloxacine et de tétracycline sous la lumière solaire.

Un nanocomposite efficace de $BiVO_4$-APS-C_{60} a été développé en intégrant les nanoparticules C_{60} fonctionnalisées par aminosilicate à la surface de nanocouches ultrafines de $BiVO_4$. L'intégration de C_{60} sur $BiVO_4$ a élargi l'absorption de la lumière dans le domaine du visible et a également offert une génération et une séparation efficaces des porteurs de charge photo-induits. En fait, l'aminosilicate a établi une forte interaction interfaciale entre C_{60} et $BiVO_4$, ce qui a fourni un transfert de charge efficace et une stabilité remarquable du

composite $BiVO_4$-APS-C_{60}. Par conséquent, $BiVO_4$-APS-C_{60} a montré une activité photocatalytique beaucoup plus élevée vis-à-vis la dégradation de ciprofloxacine sous irradiation solaire.

Le nanocomposite Bi_2WO_6/NH_2-UiO-66 a été développé par l'incorporation de NH_2-UiO-66 sur Bi_2WO_6 ayant une forme micro/nanoflorale dans le but d'améliorer l'activité photocatalytique pour la dégradation de ciprofloxacine sous l'irradiation de la lumière solaire. L'activité photocatalytique améliorée, expliquée par la formation d'une hétérojonction avec un fort contact interfacial entre Bi_2WO_6 et NH_2-UiO-66, a permis d'élargir le domaine d'absorption lumineuse, de réduire la recombinaison de paires électron-trou photogénérées et d'accélérer le transfert des porteurs de charges. L'hétérojonction Bi_2WO_6/NH_2-UiO-66 suit le mécanisme de transfert de charge de type Z-schème et possède des sites hautement réactifs offrant une forte propriété redox au composite Bi_2WO_6/NH_2-UiO-66.

Abstract

The solar photocatalytic technique is a promising solution for the effective removal of antibiotics, which are emerging pharmaceutical pollutants in water and wastewater. The semiconductor based photocatalytic materials plays crucial role in achieving the complete degradation of these pharmaceutical pollutants. In this direction, the design of nanostructured hybrid photocatalysts shows superior catalytic performance as compared to the conventional photocatalysts towards the effective degradation of antibiotic molecules in water. These nanostructured hybrid photocatalysts overcome the limitations of weak photo-absorption, poor charge separation, slow charge transfer, high charge recombination, limited surface reaction, lesser stability and difficult recovery. In this context, we have developed potential nanostructured and nanocomposite photocatalytic materials and explored their performance in degradation of antibiotics under solar light.

Novel ferroelectric perovskite material, nanostructured calcium bismuthate ($CaBiO_3$) with distinct Bi^{3+} and Bi^{5+} multi-charge disproportion was developed via glycine-complexation and ion-exchange methods. The efficient Bi^{3+}/Bi^{5+} charge disproportion and well-organized BiO_6 octahedral crystal arrangement provided an enhanced visible photo-absorbance and higher charge carrier generation and separation to $CaBiO_3$ system. The developed $CaBiO_3$ materials exhibited nanostructure with higher surface area which provided enhanced surface properties for catalytic reactions. Moreover, the developed $CaBiO_3$ materials were potentially explored for degradation of ciprofloxacin and tetracycline antibiotic drugs under solar light.

An efficient $BiVO_4$-APS-C_{60} nanocomposite was developed by integrating aminosilicate functionalized C_{60} nanoparticles on the surface of ultrathin $BiVO_4$ nanolayers. The integration of C_{60} on $BiVO_4$ broadened the light absorption spectrum in the visible light range and offered an enhanced generation and separation of the photoinduced charge carriers. The aminosilicate group established a strong interfacial interaction between C_{60} and $BiVO_4$, which provided remarkable charge transfer efficiency and stability for $BiVO_4$-APS-C_{60} composite. The as-synthesized $BiVO_4$-APS-C_{60} displayed high photocatalytic activity towards ciprofloxacin degradation under solar light irradiation.

Bi_2WO_6/NH_2-UiO-66 nanocomposite was designed incorporating NH_2-UiO-66 with Bi_2WO_6 micro/nanoflower for enhanced photocatalytic activity towards ciprofloxacin degradation under solar light irradiation. The improved photocatalytic activity attributed to the formation of heterojunction with strong interface contact between Bi_2WO_6 and NH_2-UiO-66, broadened the photoabsorbance range, reduced photogenerated electron-hole pair recombination, and accelerated charge carrier transfer. The Bi_2WO_6/NH_2-UiO-66 heterojunction follows Z-scheme charge transfer mechanism with high surface reactive sites providing strong redox property to Bi_2WO_6/NH_2-UiO-66 composite.

Table of Contents

List of Figures

List of Schemes/Tables

List of Abbreviations

A	Electron-acceptor
APS	Aminopropyl triethoxysilane
BET	Brunauer Emmett Teller
BE	Binding energy
BQ	Benzoquinone
CB	Conduction band
CIP	Ciprofloxacin
CTAB	Cetrimonium bromide
D	Electron-donor
EDX	Energy dispersive X-ray spectroscopy
EM	Electron microscopy
ESR	Electron spin resonance spectroscopy
FTIR	Fourier transform infrared spectroscopy
GC	Gas chromatography
IPA	Isopropyl alcohol
SPR	Surface plasmon resonance
MS	Mass spectroscopy
MeOH	Methanol
MOF	Metal organic framework
NC	Nanocomposite
NHE	Normal hydrogen electrode
NMR	Nuclear magnetic resonance spectroscopy
NP	Nanoparticle

NRR	Nitrogen reduction reaction
OV	Oxygen vacancies
PC	Photocatalyst
PEC	Photoelectrochemical
PL	Photoluminescence
PS	Photocatalytic system
PVP	Polyvinylpyrrolidone
QE	Quantum efficiency
SC	Semiconductor
SEM	Scanning electron microscopy
TEC	Tetracycline
TEM	Transmission electron microscopy
TEOA	Triethanolamine
UV-Vis	Ultraviolet-visible spectroscopy
VB	Valence band
XPS	X-ray photoelectron spectroscopy
XRD	X-ray diffraction analysis

Acknowledgment

I want to thank Prof. Trong- On Do for giving me the great opportunity to pursue the Doctoral Program at Université Laval. His continuous motivation and immense knowledge greatly supported me throughout the course of my doctorate. He has provided me with the necessary infrastructure, resources and freedom to explore my ideas and has encouraged me to do innovative and creative research. I am grateful for his continued mentorship and valuable pieces of advice to complete the research project.

I also want to express my gratitude to Prof. Sakar Mohan, a former member of Prof. Do's group. His career advice and recommendations have helped me a lot in achieving my goals. He gave me a deep insight into the fundamentals of photocatalysis and writing research articles. Furthermore, I extend my gratitude to my group members, Dr. Chinh Chien Nguyen, Dr. Nhu-Nang Vu, Dr. Arnaud Gandon, Dr. Manh-Hiep Vu, Duc-Trung Nguyen, Vishnu Nair Gopalakrishnan, Jorge Becerra, Pejman Monazzam, Toan-Anh Quach, Anis Chouat and Edward F. Pena for their great support, good atmosphere at work and valuable discussions.

I want to thank the administrative staff, Ms. Ann Bourassa, Ms. France Cayouette and Ms. Nadia Dumontier as well as all professors of the Department of Chemical Engineering for their excellent assistance and great support. I also want to thank the technicians, Mr. Jean-Nicolas Ouellet, Mr. Jérôme Noël and Mr. Marc Lavoie for their precious advice and instructions in the laboratory works and equipment operation. Additionally, I want to thank Mr. Alain Adnot for his help with XPS, Mr. Jean Frenette for XRD and Mr. Richard Janvier for electron microscopy analyses.

I gratefully acknowledge the Natural Science and Engineering Research Council of Canada (NSERC) through Strategic Project (SP), Discovery Grants and Exp Inc for their financial support. I also want to thank the Department of Chemical Engineering, Université Laval for additional financial support.

Finally, I want to acknowledge my parents Karuppannan and Vijaya for their encouragement and great support throughout my studies helping me to stay on top of things.

Foreword

The present PhD thesis includes seven chapters. It is constructed based on the combination of scientific articles whose first author is the author this thesis. All the articles have been published or submitted at the time of thesis submission.

Introduction and Chapter 2 are written by partially incorporating the book chapters "Design of photocatalysts for the degradation of emerging pharmaceutical contaminants in water" Elsevier Publisher 2021, 475-502 published by K. Rokesh, M. Sakar, Trong-On Do and "Nanocomposite photocatalysts for the degradation of contaminants of emerging concerns" Springer Publisher 2021, 85-112 published by K. Rokesh, M. Sakar, Trong-On Do.

Chapter 4 presents "Calcium bismuthate ($CaBiO_3$): a prospective sunlight driven perovskite photocatalyst for the degradation of emerging pharmaceutical contaminants" published by K. Rokesh, M. Sakar, Trong-On Do in ChemPhotoChem, 2020, 4, 373-380.

Chapter 5 presents "Integration of aminosilicate functionalized-fullerene (C_{60}) QDs on bismuth vanadate ($BiVO_4$) nanolayers for the photocatalytic degradation of pharmaceutical pollutant" submitted by K. Rokesh, M. Sakar, Trong-On Do in Catalysis Today 2021, 10.1016/j.cattod.2021.10.006.

Chapter 6 reports "Amine-functionalized metal-organic framework integrated bismuth tungstate (Bi_2WO_6/NH_2-UiO-66) composite for the enhanced solar-driven photocatalytic degradation of ciprofloxacin molecules" submitted by K. Rokesh, M. Sakar, Trong-On Do in New Journal of Chemistry 2021,10.1039/D1NJ03977F.

The candidate carried out the experimental works and collected data of all these works under the supervision of Prof. Trong-On Do. The first version of all manuscripts was written by the candidate, the other authors revised the manuscripts prior to submission.

Introduction

1.1 Antibiotics: emerging pharmaceutical pollutants

Water is one of the major resources for the survival of different ecological systems on earth. Now, with rapid population expansion and industrialization, the water demand has increased dramatically. The burgeoning world population also leads to a massive intake of chemical substances at different levels; the number of chemical industries and the growing discharge of chemicals into the environment is therefore increasing quickly. Therefore, maintaining the quality of water sources is highly necessary towards keeping healthy ecosystems and assurance of safe drinking water. The common water pollutants includes dyes, pesticides, poly-aromatic compounds, polychlorinated compounds and persistent organic pollutants and they have been significantly identified and removed by appropriate measures and techniques[1]. But recently the scientific communities identified the presence of pharmaceutical residues in water/wastewater and their harmful effects on human life and other ecosystems have received huge attention worldwide. Till date, the pharmaceutical compounds are not covered under any pollution regulations and their effects on the biological and human system are not studied well[2]. However, the occurrences of these pharmaceutical products are rising in global water bodies is shown in **Figure 1.1**[3].

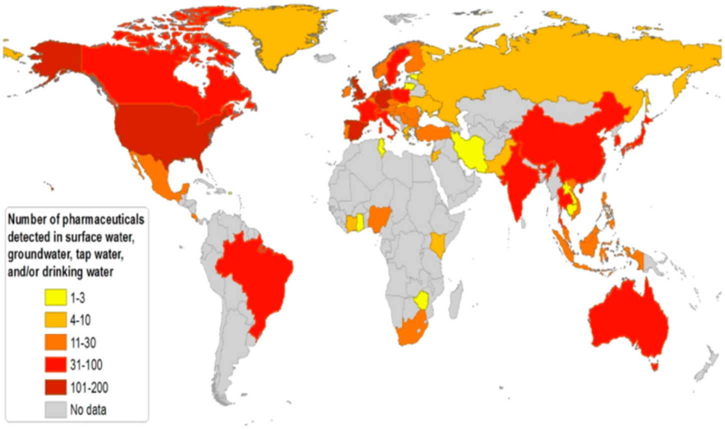

Figure 1.1. The number of pharmaceutical compounds detected in surface waters, groundwater and tap/drinking water worldwide[3].

Pharmaceutical industry is one of the most important and largest industries worldwide and at the same time, a large number of contaminations is being generated by the pharmaceutical production. These pharmaceutical products are disseminated in higher quantities to the environment intentionally and/or accidentally. Subsequently, these pharmaceutical compounds can be found in different environmental compartments such as soil, water surfaces and even in drinking water. Especially, these pharmaceutical products are frequently detected in natural and wastewater system[2, 4]. The quantity of pharmaceutical pollutants and their metabolites collection in water bodies are not high-pitched (ng to mg per liter), however, these pharmaceutical molecules are specifically designed to initiate biological responses at very low concentration levels. Therefore, it may lead to some adverse effects on biological systems and human health such as aquatic toxicity, high resistance bacteria, acute and chronic disease, hormonal and endocrine disruption. Also, most of the pharmaceutical drugs possess very stable chemical structure and non-biodegradable properties. Therefore, the detection of pharmaceutical compounds in the water system has evolved as a growing concern worldwide, which is essentially due to their potential toxicity and hazard to the living ecosystems and humans beings[5].

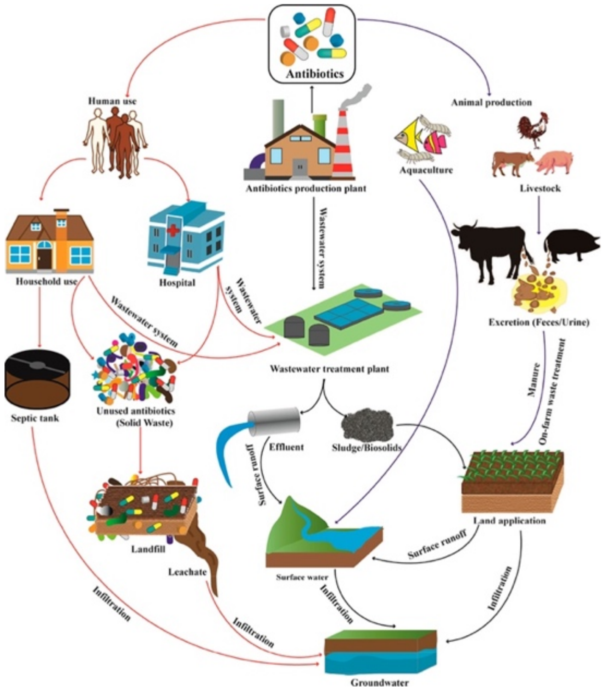

Figure 1.2. Potential sources of antibiotic release and entry into water systems[6].

Among the various pharmaceutical products, antibiotics have received more attention as they generate serious toxicity and produce long-term chronic effects to humans and ecosystems, and the antibiotic residues generate serious environmental health issues such as antimicrobial resistivity, antibiotic resistive bacteria and gene mutations. The potential sources of antibiotic dissemination into water bodies are shown in **Figure 1.2**. According to the World Health Organization (WHO), the antimicrobial resistance is an emerging problem, which generates multi-drug resistant infections to human and animals[7, 8]. Therefore, antibiotics are considered as “contaminants of emerging concerns” or “emerging pharmaceutical pollutants” due to their potential toxicity and their rising occurrence in global water bodies. In addition, the antibiotic residues in the environment could result into various adverse effects and generate stable organic by-products, which are difficult to degrade by the conventional waste-water treatment processes and they could cause the generation of secondary pollutions as well as lead to increase the population of antibiotic resistant bacteria. Hence, there is an urgent need to address these emerging concerns and develop an efficient and sustainable technique for degradation of these antibiotic pollutants from water and wastewater. There are numerous techniques available to remove antibiotic chemicals from water, which include adsorption, photocatalysis, ozonolysis, filtration and biological processes as depicted in **Figure 1.3**[5, 9, 10].

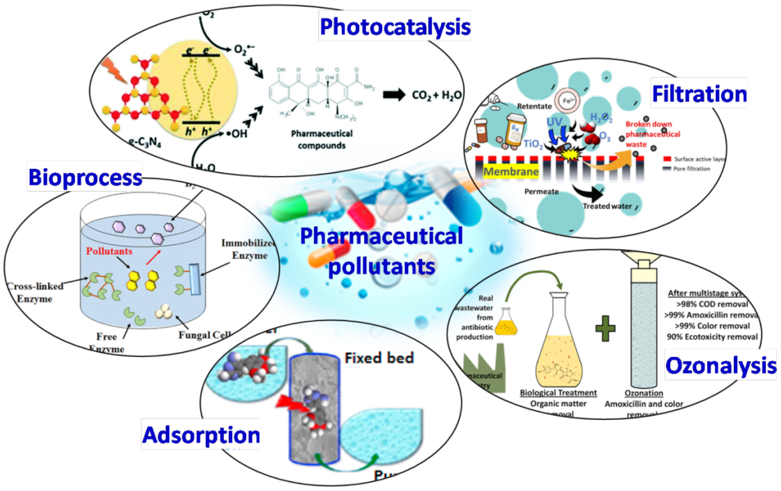

Figure 1.3. Various processes for the degradation/removal of pharmaceutical pollutants from water.

Of these techniques, the semiconductor based solar photocatalytic technique deserves a great consideration because of its potential redox ability and superior degradation performance, high mineralization efficiency and less/harmless products generation, being exclusively performed under solar light[11, 12]. However, the photocatalytic efficiency of semiconductor photocatalysts mainly depends upon several crucial factors such as band gap, band structure, charge separation, charge transfer, redox potential and surface properties[13]. Accordingly, considerable efforts have been made to tuning these properties by designing nanostructured hybrid photocatalysts with controlled preparation methods[14]. These nanostructured hybrid materials fundamentally offer enhanced surface and catalytic properties delivered by large surface area, rich active sites, extended photoabsorbance, high charge generation, improved charge separation, efficient charge transfer and strong redox properties[11, 14-16]. Hence, these nanostructured and nanocomposite photocatalysts effectively degrade and mineralize the antibiotics in water in presence of sunlight.

1.2 Objective of thesis

This thesis aims at designing nanostructured and nanocomposite photocatalysts with high performance using potential semiconductor materials for the degradation of emerging pharmaceutical pollutants under sunlight.

First objective is to provide a detailed review of the current progress in the design of nanostructured composite photocatalysts for antibiotic degradation. Promising materials for higher photocatalytic performance and their nanostructure designs are proposed.

Second objective is to develop and explore promising photocatalysts toward pharmaceutical pollutants degradation. It encompasses designs of $CaBiO_3$ nanosheet, $BiVO_4$-APS-C_{60} and Bi_2WO_6/NH_2-UiO-66 nanocomposite and their photocatalytic performance in antibiotic degradation under solar light.

Third objective is to suggest a potential material for efficient solar-driven photocatalytic degradation of pharmaceutical pollutants.

1.3 Structure of thesis

Introduction

In this part, the emerging environmental issues concerning pharmaceutical pollutant generation and potential solar energy assisted photocatalytic technique to deal with these environmental problems.

Chapter 2: Literature review

In this chapter, the fundamentals of semiconductor-based photocatalysis are discussed in detail. In addition, the construction and performance of nanostructured and nanocomposite photocatalysts and design of new photocatalytic materials towards the degradation of emerging pharmaceutical antibiotic pollutants from water.

Chapter 3: Characterization techniques

This chapter describes the fundamentals of various advanced characterization techniques used to investigate the physical and chemical properties of the developed catalytic materials.

Chapter 4: Calcium bismuthate ($CaBiO_3$): a prospective sunlight driven perovskite photocatalyst for the degradation of emerging pharmaceutical contaminants

$CaBiO_3$ is a new ferroelectric perovskite structured material with co-existing Bi^{3+}/Bi^{5+} charge disproportion. It showed synthesis method-dependent structural features and defects, as well as excellent photocatalytic activity towards the degradation of ciprofloxacin and tetracycline antibiotic under solar light.

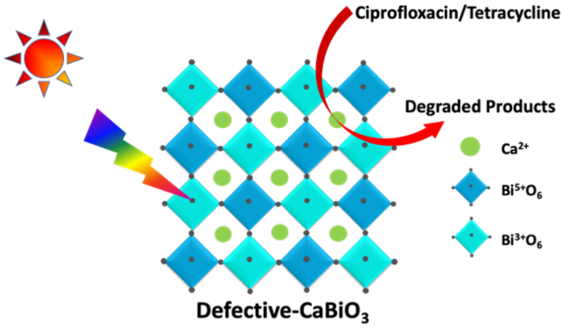

Chapter 5: Integration of aminosilicate functionalized fullerene (C_{60}) QDs on bismuth vanadate ($BiVO_4$) nanolayers for the photocatalytic degradation of pharmaceutical pollutant

An efficient $BiVO_4$-APS-C_{60} composite was developed by integrating the aminosilicate functionalized C_{60} nanoparticles on the surface of ultrathin $BiVO_4$ nanolayers. The strong integration and interfacial contact of $BiVO_4$-APS-C_{60} resulted in a superior photocatalytic activity towards ciprofloxacin degradation in presence of solar light.

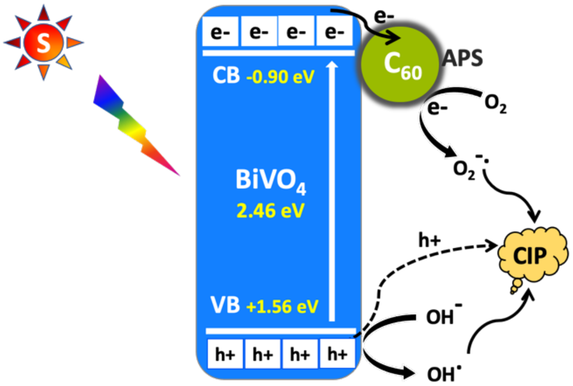

Chapter 6: Amine-functionalized metal-organic framework integrated bismuth tungstate (Bi_2WO_6/NH_2-UiO-66) composite for the enhanced solar-driven photocatalytic degradation of ciprofloxacin molecules

Bi_2WO_6/NH_2-UiO-66 nanocomposite was designed incorporating NH_2-UiO-66 with Bi_2WO_6 micro/nanoflower for improved photocatalytic activity towards ciprofloxacin degradation under solar light irradiation. The Z-scheme heterojunction with strong interface contact improved charge separation, offered faster charge transfer and strong redox property to Bi_2WO_6/NH_2-UiO-66 composite.

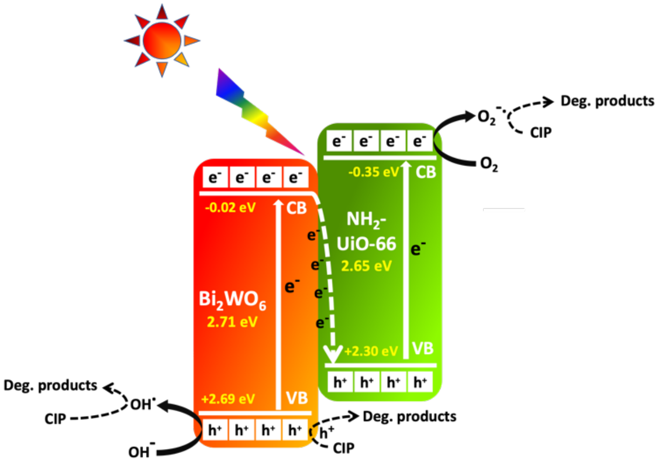

Conclusions and future work

This part summarizes the conclusion of the research works presented in this thesis and proposed some materials for future works.

Chapter 2 : Literature review

2.1 Fundamental of photocatalysis

Photocatalysis is a semiconductor based photoinduced advanced oxidation process. It utilizes solar energy to perform the potential redox reactions for degrading antibiotic contaminants. The photocatalytic process proceeds through the following four main steps: photo-absorption, charge separation, charge transfer and redox reaction. A semiconductor photocatalyst has valence band (VB) and conduction band (CB) separated by an energy gap known as band gap energy (Eg). Generally, the semiconductor photocatalyst undergoes the photo-absorption that excites the electrons from valence band to conduction band, leaving holes in the valence band. This charge separation further leads to the promotion of electrons from conduction band to the photocatalyst surface to perform the reduction reaction and the holes to perform the oxidation reaction[17-19]. It should be noted that both the oxidation and reduction (redox) reactions are fundamental processes in photocatalysis, which essentially lead to the primary and secondary degradation processes as depicted in **Figure 2.1**.

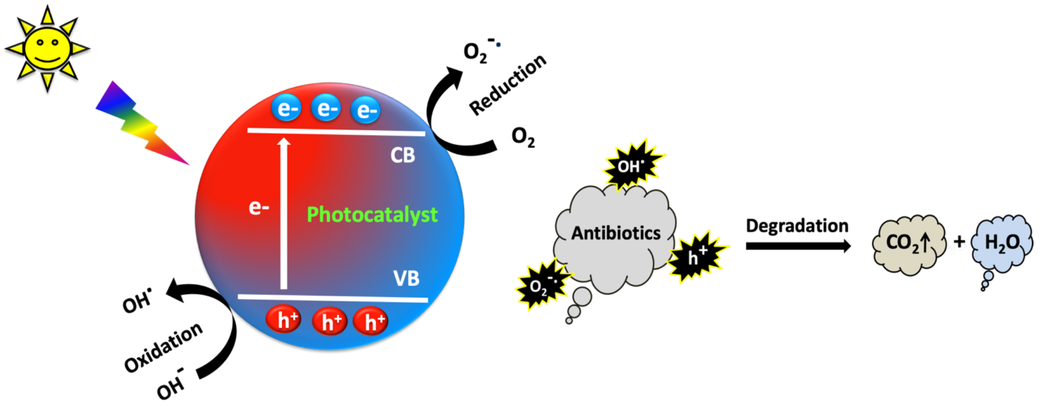

Figure 2.1. The process of photocatalytic degradation of antibiotics.

The primary reaction involves the direct oxidization of the antibiotic molecules by photogenerated holes (h^+). The secondary reaction involves free radicals, while the oxidization of water molecules with photogenerated holes produce hydroxyl radicals ($^{\bullet}$OH), it's consequently initiates the oxidation reaction. On the other hand, the photogenerated electron can be entrapped by oxygen molecule, leading to the formation of superoxide radicals ($O_2^{\bullet-}$) and oxidize the antibiotic molecule. Among them, the hydroxyl radicals have attracted more attention in photocatalytic degradation process due to their strong oxidation potential and as they yield non-selective destruction, which will be able to convert a wide range of contaminants without any additives. Therefore, the photocatalytic redox reaction with free radicals generation is able to oxidize and completely mineralize the antibiotic pollutants[20, 21].

2.2 Semiconductor photocatalyst

The photo-response semiconductor materials plays a key role in the photocatalytic process due to their band structure, crystal and surface properties[22]. The semiconductor photocatalysts with suitable band gap and band alignment can provide an efficient photoabsorbance and potential charge diffusion. The high order of crystallinity and crystal defects tend to reduce the probability of recombination of photo-generated electron-hole pairs and provide efficient charge transfer in the system. Their large surface area means higher colloid dispersion and surface-active sites, which facilitate the enhanced adsorption of reactant molecules and higher photocatalytic activities[13, 23, 24]. However, the semiconductor based photocatalytic materials possess several limitations such as wide band gap energy, high number of structural defects, poor charge carrier's separation, greater charge recombination, low charge transfer and poor surface properties. In addition, the photo-corrosion properties of the semiconductor photocatalysts also limit the stability and overall efficiency of the photocatalytic system[25, 26].

2.3 Nano-photocatalyst

Nanotechnology has made ground-breaking impact on photocatalytic material design and development. Nanomaterials have large surface area, diverse morphology, enriched surface, catalytic and physio-chemical properties and easy fabrication[27]. All these properties are beneficial for the significant development of novel nano/nanostructured photocatalysts. Exclusively, a nanostructured photocatalyst is providing diverse and potential routes towards enhancing the photocatalytic efficiencies by many folds. Nanoscale design generally favors the surface-dependent photocatalytic activity as it provides more specific surface area and reactive sites. Also, the nanostructured photocatalysts facilitate the generation of larger amounts of photogenerated electron-hole pair separation, which essentially reduces the charge recombination and improves the photocatalytic activity. The nanoparticles facilitate the fast charge carrier migration to the surface due to the core to surface of catalyst distances being shorter than in bulk materials(**Figure 2.2**)[27].

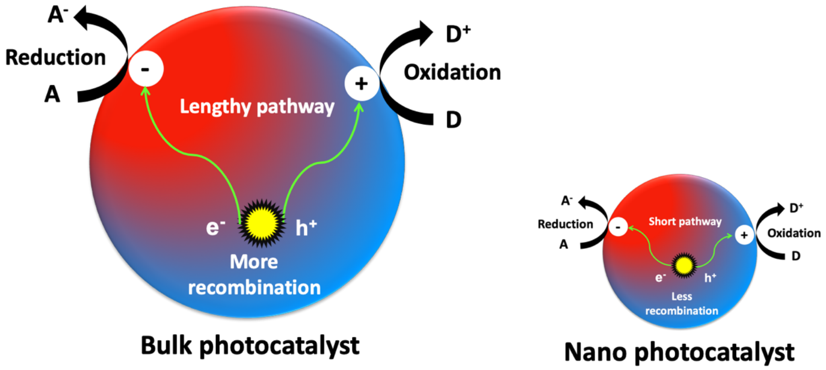

Figure 2.2. Charge carrier's migration and recombination process in bulk and nano-photocatalysts.

The migration of charge carriers requires a potential gradient for fast and effective charge transfer, which is closely correlated with morphology, structure and surface properties of semiconductor photocatalyst. A notable development has been made in the morphology and size-controlled synthesis. Investigations were even carried out on the relationship between the morphological or structural characteristics and the photocatalytic properties. For example, the nanoaggregates have resulted in significant advances in tailoring the photocatalytic performances. The synthesis of aggregates is mainly dependent on the templates, surfactants and additives. For instance, the mesoporous titanium dioxide (TiO_2) nanoaggregates were synthesized from titanium glycolate precursor via three different post-treatment methods such as hydrothermal, calcination and hydrothermal-calcination techniques. These post-treatment techniques obviously influenced the TiO_2 nanoaggregates and their structural formation, and thereby influenced their catalytic performance as well. Accordingly, the as-developed mesoporous TiO_2 nanoaggregates were studied for their adsorption- and photocatalysis-mediated performances towards the removal of ciprofloxacin (**Figure 2.3**)[28].

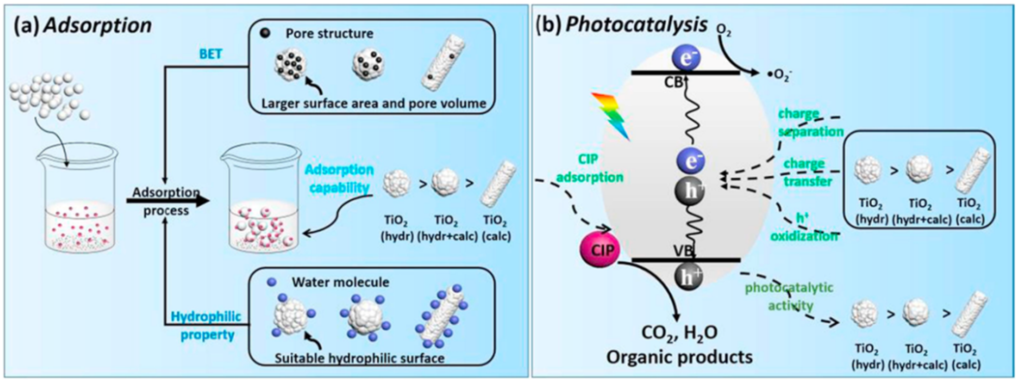

Figure 2.3. The adsorption and photocatalytic performance of mesoporous TiO_2 nanoaggregates[28].

Similarly, ZnO nanoaggregates were synthesized using polyol-aqueous medium by optimizing the polyol and water composition. The photocatalytic performance of ZnO nanoaggregates was examined on ciprofloxacin photodegradation under simulated solar light irradiation also compared with different nanostructures[29]. Further, Zn_2GeO_4 hollow spheres were fabricated via in-situ template-engaged approach, with increasing reaction time Zn_2GeO_4 nanorods (400-600 nm size) were gradually transformed into Zn_2GeO_4 nanobundles. As-compared to bulk Zn_2GeO_4 (solid state synthesis), the template assisted hollow spheres Zn_2GeO_4 was found to show efficient photocatalytic activity and excellent photostability on metronidazole degradation due to their hollow structure and high specific surface area[30].

2.4 Ultrathin photocatalyst

The ultrathin two-dimensional materials present significant advantages in photocatalytic performance and solar energy conversion due to their unique structural and electronic properties[31, 32]. The ultrathin materials tend to possess distinct photoexcitation processes thus yielding diverse photocatalytic activities, because of the abundant surface structural features and strong quantum confinement effects. It is well-known that the photocatalytic performance is closely interrelated with morphology, structure and dimension of photocatalysts. The atomically thin materials provide ultra-high specific surface area, which allows efficient photo absorption. Also, the ultrathin nature permits fast photo-excited charge carriers transfer from core to surface of the photocatalyst thereby reducing recombination and increasing charge separation[33]. Relatively, the ultrathin materials are reduced to single-unit cell thickness, hence establishing a higher conduction band dispersion than compared to bulk materials. Ultrathin photocatalysts with two-dimensional assemblies were found to have high catalytic efficiency due to their unique architecture and structural properties, increasing the two-dimensional conductivity and providing superior structural stability[31, 34]. For example, the ultrathin TiO_2 nanoflakes with average thickness of 1.66 nm displayed strong photoabsorbance and faster charge carriers transfer due to the ultrathin thickness and two-dimensional structure which yields ultra-high fraction of surface atoms and increased charge density concentration on TiO_2 nanosheet surface. These materials resulted in 450 times higher photocatalytic conversion as compared to bulk TiO_2 towards the carbon dioxide reduction to formate (**Figure 2.4**)[35].

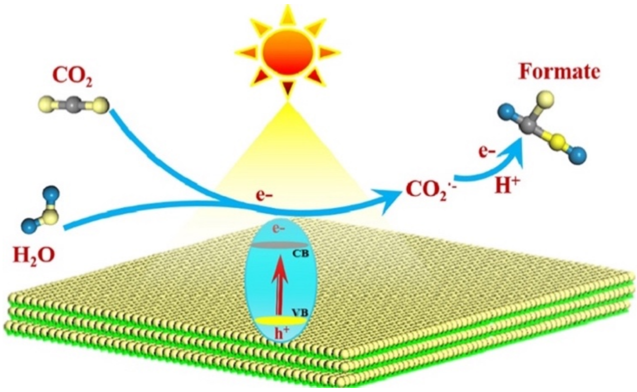

Figure 2.4. Carbon dioxide photoreduction on ultrathin TiO_2 nanoflakes[35].

Similarly, ultrathin Bi_2WO_6 sheets with average thickness of 3-4 nm exhibited higher photocatalytic activity than Bi_2WO_6 nanodisks in both organic pollutant degradation and water oxidation. The two-dimensional crystal structure and electronic properties facilitated fast hole transport which provided stronger oxidation ability to ultrathin Bi_2WO_6. In addition, in the ultrathin structure, photogenerated charge carriers rapidly migrates to the surface, resulting in greatly lowered recombination rate and enhanced photocatalytic activity[36]. Hence, the ultrathin photocatalyst design provides high surface area and efficient charge carrier transfer thus potentially improving the adsorption and photocatalytic degradation of antibiotics.

2.5 Nanocomposite photocatalyst

In general, a single component semiconductor photocatalyst shows a limited solar light absorption, poor charge separation, higher rate of charge recombination, low charge transfer efficiency and photo-corrosion[21, 37]. To develop nanocomposite photocatalysts, a nanostructured semiconductor can be coupled with single or multiple nanoscale materials with specific properties (metal or metallic compound , semiconductor, carbon materials)[38, 39]. It is realized that the surface and structural properties of semiconductor-metal/semiconductor-metallic/semiconductor-semiconductor/semiconductor-carbon are the key features to construct potential heterojunction composites. A large surface area and high-efficient interface with effective contacts are important tools for the improved charge transfer and reduced recombination in the system. An optimal band gap and band edge alignment also determine the separation and transport efficiency of photogenerated charge carriers, which should be considered during the fabrication of heterojunction nanocomposites. Then the suitable materials should be chosen to couple them in order to achieve high-efficient and stable photocatalysts[21, 26, 37-43]. Hence, a nanocomposite photocatalyst can potentially overcome the above drawbacks of single component semiconductor photocatalyst and even provide additional benefits. Besides, the designing of such hybrid nanocomposite systems functioning with distinctive photocatalytic mechanisms such as Schottky, plasmonic, Z-scheme and p-n heterojunction, etc. Therefore, nanocomposite materials designing play a vital role in improving photocatalytic performance and so up to now many nanocomposite photocatalysts have been developed and applied for antibiotic degradation.

2.5.1 Semiconductor-metal/metallic composites

The incorporation of metal/metallic nanoparticles with semiconductors is one of the most effective routs to achieve higher photocatalytic performance. Most of the efficient nanocomposite photocatalysts are generally obtained by loading of metal/metallic nanoclusters onto the surface of semiconductor nanostructure. The semiconductor-metal/metallic nanocomposite photocatalysts offered two benefits: (i) improved charge separation at the semiconductor-metal interface by the formation of Schottky barrier and (ii) increased absorption visible photoabsorbance via the surface plasmon resonance effect (**Figure 2.5**)[44].

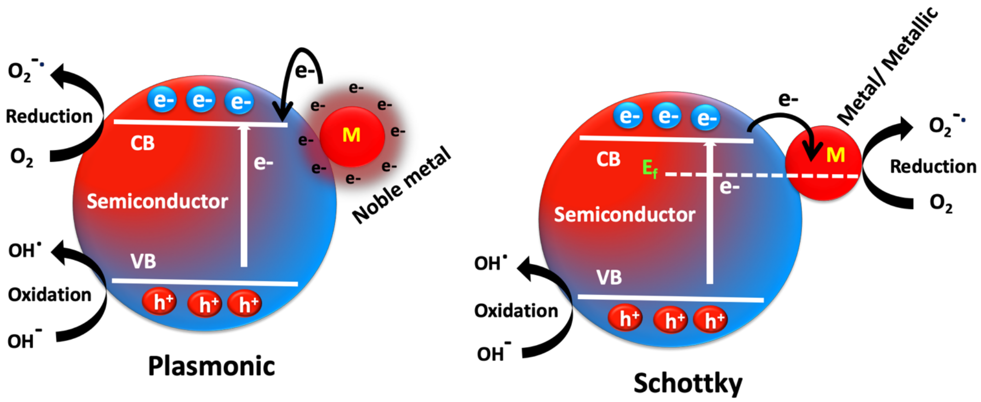

Figure 2.5. Schematic illustration of plasmonic-photocatalyst and Schottky-photocatalyst working mechanism.

i) Schottky photocatalysts

The development of semiconductor-metal composite established a Schottky barrier via Fermi level equilibration between metals and semiconductor interface. Due to the existence of the Schottky barrier, the Fermi level equilibrium alignment of metal and semiconductor leads to the creation of a "built-in electric field" near the interface, which is favors the rapid charge carrier separation in the system[44]. Notably, the efficiency of Schottky barrier is also governed by the difference in the work function of metal and semiconductor involved in the system. For example, the silicate supported CdS/Pt heterostructure composite was fabricated and Pt nanoparticles were photo-deposited on silicate integrated CdS nanosphere. The Schottky barrier formation between Pt and CdS enhanced the electron-hole pairs separation and suppressed reverse migration of electrons from photoexcitation, thereby improved photocatalytic activity and degradation of tetracycline[45]. On the other hand, the metal carbides are demonstrated to be the promising candidates for photocatalytic applications because of their metal-like properties and good electrical-thermal stability. In this direction, the fabrication of Ag_3PO_4/Ti_3C_2 Schottky photocatalyst was greatly improved the photocatalytic activity and photo-stability of Ag_3PO_4 towards the degradation of tetracycline. In consequence of the surface hydrophilic functional groups of Ti_3C_2 tend to construct a strong interfacial contact with Ag_3PO_4, it facilitated to have a strong Schottky junction between Ag_3PO_4 and Ti_3C_2 towards enhancing the charge carriers separation and stability of the photocatalyst (**Figure 2.6**)[46].

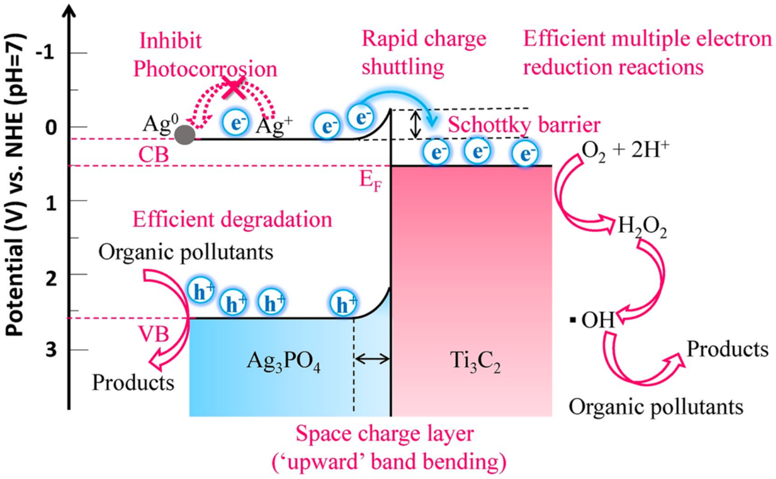

Figure 2.6. The Schottky barrier formation and photocatalytic degradation mechanism of Ag_3PO_4/Ti_3C_2[46].

ii) Plasmonic photocatalysts

On other hand, the metal components (i.e., noble metals) in the metal/semiconductor heterostructure could also enhance the light absorption of semiconductors through a surface plasmon resonance (SPR) effect. The SPR effect of noble metals could be described as the collective oscillation of surface electrons, when the frequency of photons matches with frequency of surface electrons the oscillation established against the restoring force of positive nuclei, then it would be transferred to the semiconductor. Thereby, enhanced photo-absorption and photocatalytic activity of the nearby semiconductor photocatalyst can be observed. In such plasmonic photocatalyst, the resonance photon wavelength varies with different metals. Also, the surface plasmon absorption is strongly dependent on the particle size and morphology of the metals. In this direction, gold, silver and platinum have been widely investigated plasmonic metal for improving the photocatalytic performance with various semiconductor. Among them, gold and silver are most commonly used plasmonic metals as they show tunable plasmonic resonance in the visible region[47, 48]. For example, the WO_3/Ag plasmonic composites were developed by photo-deposition of Ag NPs onto the WO_3 nanoplates surface. The silver metal particle assigned to SPR effect, which essentially broadened the visible absorption range of WO_3/Ag composites and improved the photocatalytic degradation of antibiotic sulfanilamide. The photocatalytic results showed that the WO_3/Ag composites accomplished much better activity than pure WO_3, which reached highest removal efficiency of 96.2% in 5 h[49]. Similarly, the Ag/Bi_3TaO_7 plasmonic photocatalyst showed significantly higher photocatalytic efficiency up to 85.42% of tetracycline removal in 120 min under visible light irradiation, which was ~1.5-fold higher as compared to the pristine Bi_3TaO_7. The improved photocatalytic efficiency was endorsed to the surface plasmon resonance effect of metallic silver (Ag) nanoparticles. Meanwhile, the potential incorporation of Ag nanoparticles into Bi_3TaO_7 surface established the inner-electromagnetic field, which boosted the photogenerated charge carriers separation[50]. Also, this mechanism was found to be suitable for the bimetal-semiconductor composite of Au/Pt/g-C_3N_4 photocatalyst. Under visible light, Au nanoparticles established charge separation and transfer the electrons into g-C_3N_4 semiconductor. The surface plasmon resonance effect of Au and electron-sink function of Pt nanoparticles were found to improve the optical absorption property and photogenerated charge carriers separation in g-C_3N_4 (**Figure 2.7**), which synergistically supporting to photocatalytic degradation of tetracycline antibiotic and observed 93.0% degradation efficiency in 180 min[51].

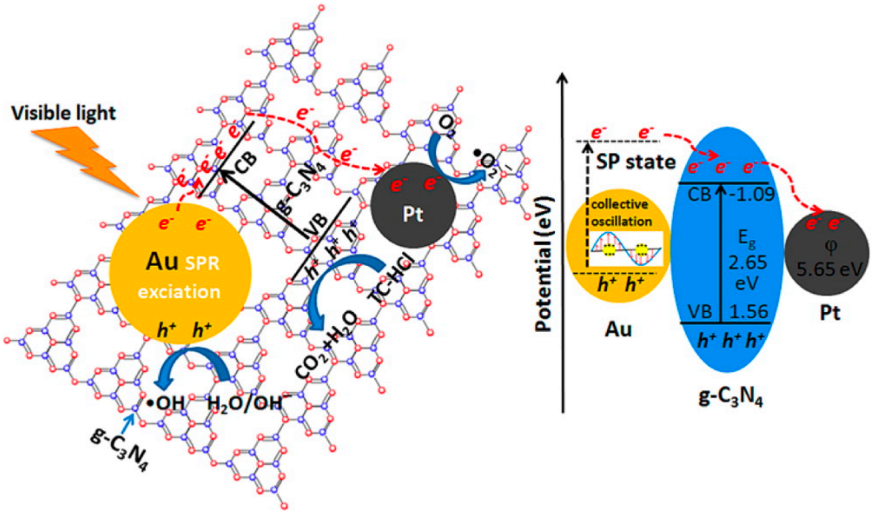

Figure 2.7. The enhancement of photocatalytic activity of Au/Pt/g-C_3N_4 nanocomposites was attributed by SPR effect of gold under visible light irradiation[51].

2.5.2 Semiconductor-semiconductor composites

The semiconductor-semiconductor architecture greatly improves the efficiencies of the photocatalytic system because it offers highly distinctive charge collection and separation. The semiconductor-semiconductor heterojunction composite is mainly established two different type of effective architecture correspondingly p-n junction and Z-scheme heterojunction photocatalyst for improving charge separation and photocatalytic activity (**Figure 2.8**). The fabrication of semiconductor-semiconductor heterojunctions composite includes two steps; firstly, the main component which acts as host, then the second component, which will be well distributed on the surfaces on host to fabricate the semiconductor-semiconductor effective heterostructure composite. The designing and construction of semiconductor-semiconductor composite offers several benefits (i) efficient photoinduced charge separation and charge transfer, (ii) longer charge carrier life-time and less charge recombination, (iii) provides separate active sites and (iv) extended light absorbance range[52, 53].

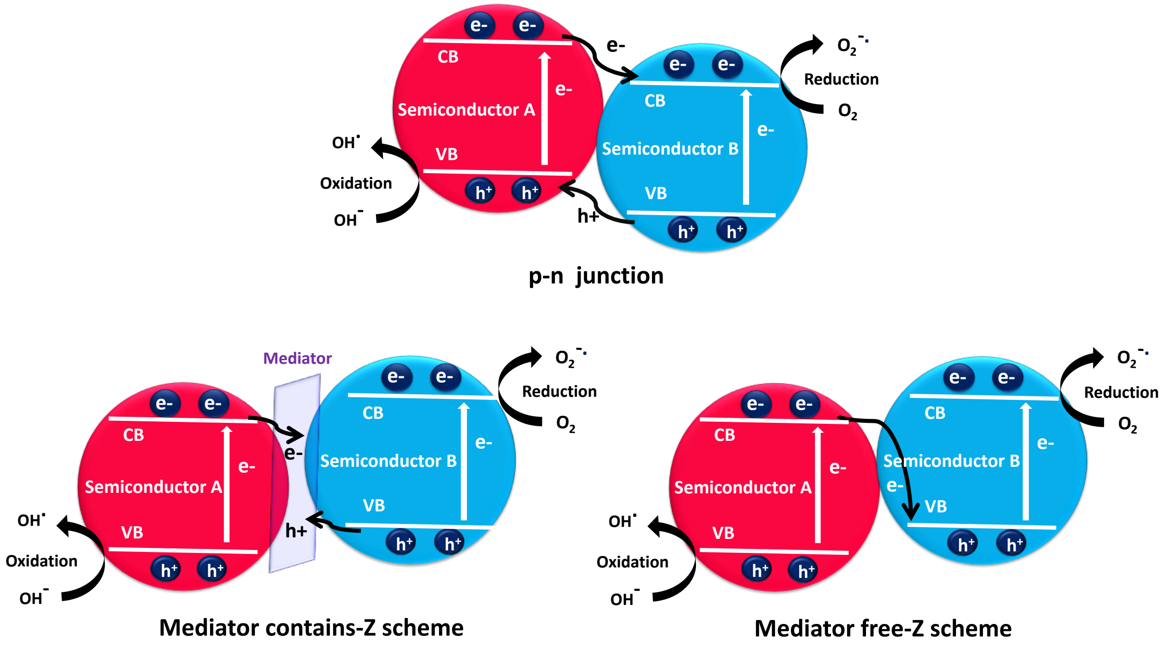

Figure 2.8. Schematic illustration of p-n junction-photocatalyst and Z-Scheme-photocatalysts (mediator and mediator-free) mechanism.

i) p-n junction photocatalysts

The p-n heterojunction photocatalyst can be established by the coupling of p-type and n-type semiconductors. In p-n junction semiconductor composite, the semiconductors with different band levels interface could form integral potential with easy charge separation, which can promote photogenerated electron-hole pairs separation and their transfer to the surroundings.

The p-n junction mechanism follows the transfer of photogenerated electrons from a semiconductor with more negative conduction band into a semiconductor with less negative conduction band. Meantime, the photogenerated holes from the semiconductor with a lower valence band will jump into semiconductor with higher valence band. The generated p-n junction formation can efficiently promote the charge separation and inhibit the charge recombination towards enhancing the photocatalytic performance[54]. For instance, the CoO/g-C_3N_4 p-n heterojunction photocatalysts were prepared via CoO nanoparticles were uniformly distributed on the wrinkled g-C_3N_4 surface to formed efficient p-n heterojunction photocatalyst. As-fabricated CoO/g-C_3N_4 p-n heterojunction photocatalyst performance was explored on tetracycline degradation (90% in 60 min) and showed a superior visible-light photocatalytic activity as compared to individual g-C_3N_4 and CoO. The superior photocatalytic activity was ascribed to the fast charge separation were attributed to the inner electric field created by the formation of a p-n heterojunction between CoO and g-C_3N_4 **(Figure 2.9**).

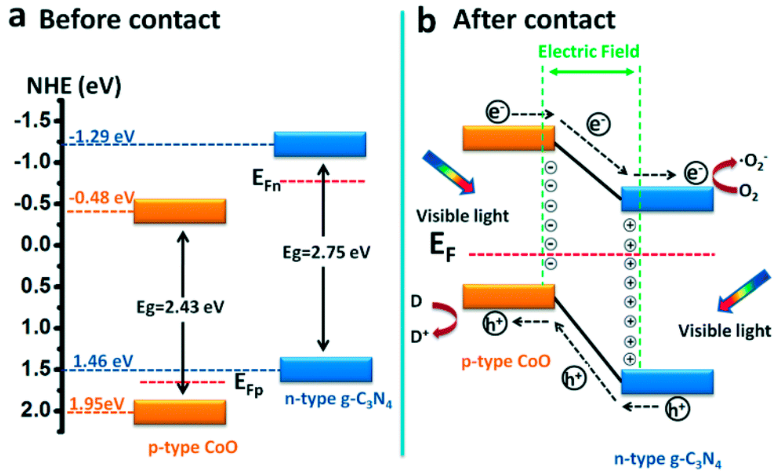

Figure 2.9. The band alignment and charge transfer mechanism of CoO/g-C_3N_4 p-n heterojunction (a) before contact and (b) after contact[55].

Moreover, the CoO nanoparticles aggregation was repelled by the introduction of g-C_3N_4, which improved the photocatalytic stability of CoO/g-C_3N_4 p-n heterojunction[55]. Further, a stable p-n heterojunction CuS/$BiVO_4$ photocatalyst developed through in suit growth of CuS nanoparticles over the surface of $BiVO_4$ and it showed enhanced visible light absorption and effective photoinduced charge carrier's separation. The CuS/$BiVO_4$ heterostructure also offered high surface area and large number surface-active sites for the effective photocatalytic process. Accordingly, the $CuS/BiVO_4$ composites showed 86.7% ciprofloxacin degradation under visible light. The degradation efficiency was 2.59 and 16.54 times higher than that of pristine $BiVO_4$ and CuS, respectively[56]. Recently, a novel organic-inorganic polyaniline/silver molybdate ($PANI/Ag_2MoO_4$) p-n heterojunction nanocatalyst was successfully fabricated via in-situ deposition method over Ag_2MoO_4 on PANI. The p-n heterojunction consequently induced efficient photogenerated charge separation and migration due to the formation of internal electric field at heterojunction. This developed composite completely degraded the neurotoxic fluoroquinolone antibiotic of ciprofloxacin under UV light within 40 min. In addition, PANI was beneficial towards improving both the photocatalytic activity and stability of Ag_2MoO_4[57].

ii) Z-scheme photocatalysts

The construction of Z-scheme photocatalysts is exhibiting more benefits on the photocatalytic performance, which possess more advantages such as increased light harvesting, spatial separation of reduction and oxidation sites, strong redox ability. Z-scheme heterojunctions were constructed to overcome the limitation of the lower redox potential of the p-n heterojunction system. As compared to p-n heterojunction, the Z-scheme photocatalyst possesses the same band structure configuration but opposite charge transfer mode. During light irradiation, the photogenerated electrons transfer from semiconductor with lower conduction band into semiconductor with higher valence band holes and continuous redox reaction was occurred at semiconductors interfaces. Meantime, the photogenerated electrons with strong reduction abilities in the conduction band of semiconductor and holes with strong oxidation abilities in the valence band of the semiconductor are preserved. As a result, Z-scheme photocatalyst is found to have separate reductive and oxidative sites and lesser charge recombination for driving the photocatalytic reactions[58, 59].

a) Mediator containing Z-scheme photocatalysts

The mediator contains Z-scheme photocatalyst or all-solid-state Z-scheme photocatalytic system constructed by two different semiconductor photocatalysts with solid electron mediator at the interface of semiconductors. The higher charge-carrier separation and transfer both are succeeded by solid-state mediator at the interface of the semiconductors. Mostly, the noble-metals (Ag, Au,.) and reduced graphene oxide (RGO) were used as solid-state electron mediator[58]. For example, the construction of Ag_2O supported reduced GO enwrapped TiO_2 nanobelt nanocomposite led to the formation of a solid-state Z-scheme photocatalytic system, which significantly suppressed the photo-corrosion and promoted the charge separation in the composite. The photocatalytic performance of the developed Z-scheme RGO-Ag_2O/TiO_2 composite was studied on tetracycline degradation under UV light, visible light, near-infrared light and simulated solar light irradiation. The RGO incorporation between Ag_2O and TiO_2 was potentially improved photogenerated electrons transfer from Ag_2O to TiO_2 in Z-scheme system, which prolonged the lifetime of the photogenerated charge carrier (**Figure 2.10**). In addition, the reasonable spatial configuration and hole protective mechanism of Z-scheme photocatalytic system were realized to prevent the Ag_2O nanoparticles from photo-corrosion[60].

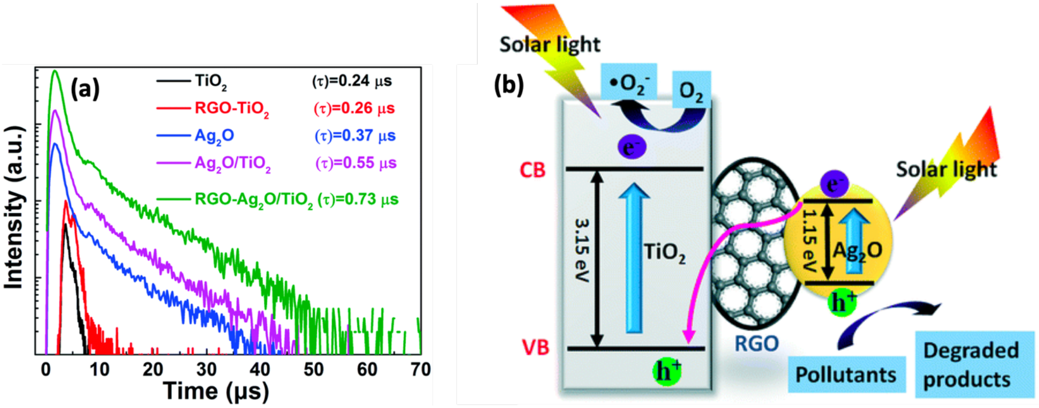

Figure 2.10. (a) Time-resolved transient photoluminescence spectra and (b) Z-scheme charge transfer mechanism of RGO-Ag_2O/TiO_2 nanocomposite[60].

Interestingly, a novel magnetic Z-scheme photocatalyst $WO_3/Fe_3O_4/C_3N_4$ was potentially developed and investigated on tetracycline degradation and found to degrade the tetracycline around 90% in 120 min. The introduction of Fe_3O_4 offered the magnetic properties, where it can also act as a conducting mediator between the WO_3 and g-C_3N_4 components, which can also participate on photo-generated charge carrier separation and transfer. Accordingly, the percentage of Fe_2O_3 and WO_3 in the$WO_3/Fe_3O_4/C_3N_4$ Z-scheme system, their impact on tetracycline degradation was systematically studied[61]. Recently, the plasmonic metal Ag bridged 2D/2D $Bi_5FeTi_3O_{15}$/g-C_3N_4 Z-scheme heterojunction photocatalysts with powerful interfacial charge transfer was established through ultrasound process. The as-developed 2D/2D heterostructure composite exhibited a notable improved photocatalytic activity on tetracycline degradation under visible-light (~70% in 60 min) and simulated solar irradiation (~85% in 20 min). It was explained that the incorporation of Ag nanoparticles between the interlayers of $Bi_5FeTi_3O_{15}$/ultrathin g-C_3N_4 nanosheets established the high-speed charge-transfer channel and accelerated the charge transfer in the constructed 2D/2D heterostructure (**Figure 2.11**)[62].

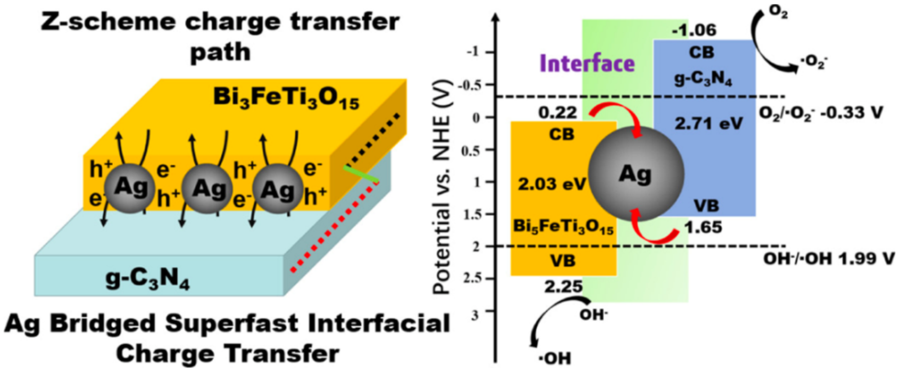

Figure 2.11. The Z-scheme superfast interfacial charge transfer of 2D/2D $Bi_5FeTi_3O_{15}$/g-C_3N_4 heterostructure[62].

b) Mediator-free Z-scheme photocatalysts

The Z-scheme photocatalysts gained great interests because of its stronger redox capacity and enriched photocatalytic performance. However, the mediator containing Z-scheme photocatalysts system usually constructed using two different semiconductors with electron mediators at the interface, but the backward reactions and poor stability are significantly affecting the photocatalytic performance of this system. Therefore, the mediator-free Z-scheme or direct Z-scheme system designing relatively established more promising practical applications than compared with mediator-containing Z-scheme system. The direct Z-scheme photocatalyst usually constructed with two semiconductor photocatalysts without mediator, one acts as strong oxidation photocatalyst and the other acts as strong reduction photocatalyst. The oxidation photocatalysts possess low valence band position and exhibit strong oxidation ability, while the reduction photocatalysts usually have a high conduction band position and display strong reduction ability. Moreover, the mediator free Z-scheme photocatalyst possesses more advantageous as compare to the mediator-containing Z-scheme system as they provide the limited backward reaction, higher stability, fast and simple charge transfer[59]. For example, an efficient direct Z-scheme based on $CuInS_2/Bi_2WO_6$ heterojunction with intimate interface contact was constructed via the direct growth of Bi_2WO_6 on $CuInS_2$ microspheres. The efficient intimate interface contact offered direct charge transfer pathways in the $CuInS_2/Bi_2WO_6$ Z-scheme heterojunction. Such arrangement remarkably promoted the photo-generated electron-hole separation and led to the higher photocatalytic performance (**Figure 2.12**). Accordingly, the developed Z-scheme $CuInS_2/Bi_2WO_6$ heterojunctions showed a higher tetracycline removal efficiency (90.5%) as compared to pure $CuInS_2$ and Bi_2WO_6 under visible light irradiation[63].

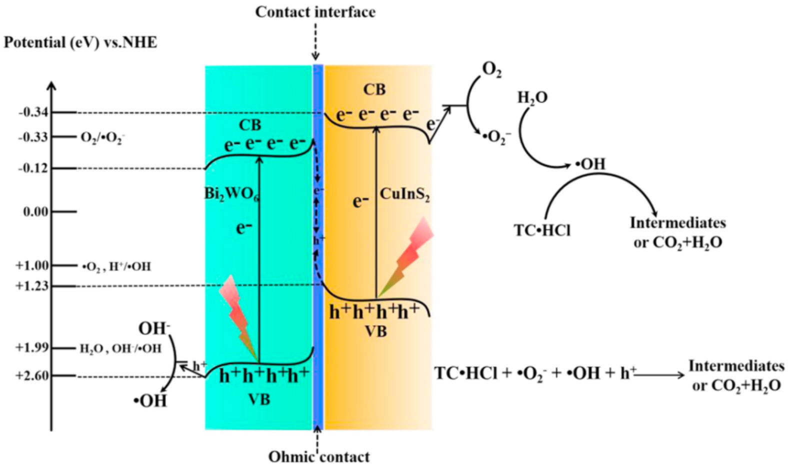

Figure 2.12. The interfacial electron transfer process and possible photocatalytic mechanism of Z-scheme $CuInS_2/Bi_2WO_6$ heterojunction[63].

Similarly, the redox mediator free direct Z-scheme marigold flower like $CaIn_2S_4/TiO_2$ composite was prepared via facile wet-impregnation method. The redox-mediator-free direct Z-scheme fabrication was significantly suppressed photo-induced charge recombination rate and also improved charge transfer thereby achieved higher photocatalytic efficiency on degradation of pharmaceutical compounds isoniazid and metronidazole. The developed direct Z-scheme $CaIn_2S_4$ marigold-flower-like/TiO_2 showed a higher photocatalytic degradation efficiency of isoniazid (71.9%) and metronidazole (86.5%) as compared to individual TiO_2 and $CaIn_2S_4$[64]. Further, a mediator-free Z-scheme γ-Fe_2O_3/g-C_3N_4 heterojunctions was developed over mesoporous γ-Fe_2O_3 nanospheres anchored on g-C_3N_4 nanosheet, the mesoporous property and enhanced specific surface area were offered large number of active sites to γ-Fe_2O_3/g-C_3N_4 heterojunctions system. Furthermore, Z-scheme heterostructure construction between γ-Fe_2O_3 and g-C_3N_4 were potentially extended and speeds up the photo-induced charge carrier separation and transfer, which is more beneficial for boosting the photocatalytic activity and degradation of tetracycline (73.8% in 120 min) under visible light[65].

2.5.3 Semiconductor-carbon composites

The semiconductor-carbon composite photocatalysts have been recently paid more attention due to their higher surface area, good conductivity, chemical stability and special electronic properties. The carbonaceous materials such as graphene, carbon quantum dots (CQDs) and carbon sphere are widely explored in photocatalysis (**Figure 2.13**).

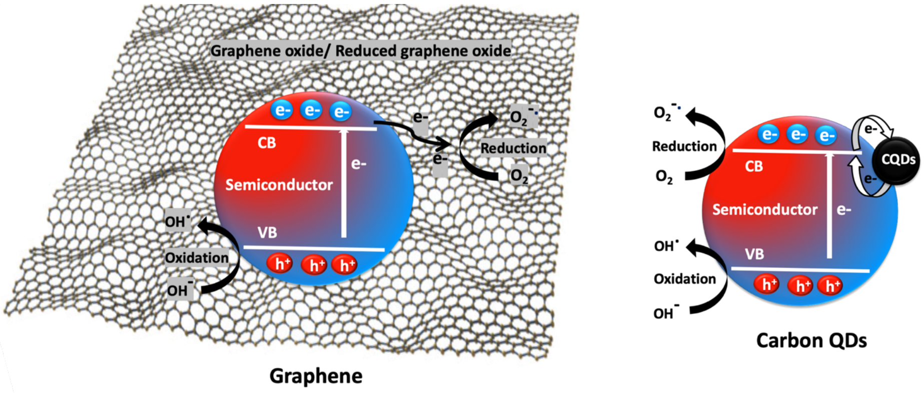

Figure 2.13. Schematic illustration of graphene-photocatalyst and carbon QDs-photocatalyst mechanism.

Also, there are numerous graphene, CQDs and carbon sphere-based nanocomposite photocatalysts were developed via different preparation routes and explored photocatalytic applications, the semiconductor-carbon established to be potential photo-induced charge separation and charge transfer thereby enhance the overall photocatalytic performances of the system. Moreover, semiconductor-carbon composite offers (i) efficient charge separation

(ii) higher charge mobility, (iii) extended photoabsorbance (iv) large specific surface area (v) good chemical and photostability[66-68].

i) Graphene photocatalysts

The graphene materials have received huge attraction in hybrid photocatalytic material designing because of their unique two-dimensional (2D) hybridized carbon structure, which specifically offers higher specific surface area, fast charge transfer and greater chemical stability[69, 70]. Also, their unique structural properties offer efficient photoinduced charge separation and transport properties thereby establishes the improved photocatalytic performances. Since it can be used as potential candidate for designing semiconductor-carbon composite photocatalyst for antibiotic degradation. For example, a two-dimensional graphene (GO) and reduced-graphene oxide (RGO) sheets have attracted much attention in photocatalysis because of their unique structure properties. For example, a distinctive ZnTe nanoparticles were well-spread onto a two-dimensional wrinkled graphene sheet surface, the RGO functioned as a solid support as well as a nucleation center of ZnTe nanocrystal. RGO-ZnTe composite exhibited around 2.6 times higher photocatalytic efficiency than ZnTe toward the degradation of tetracycline antibiotic under visible light. The enhanced catalytic performance was attributed to better interaction and synergy between RGO and ZnTe nanoparticles[71]. Similarly, the reduced graphene oxide offered good conductivity with outstanding electron transporting properties, which inhibited the photo-excited electron-hole pairs recombination in Fe_3O_4@g-C_3N_4/RGO ternary photocatalyst. Furthermore, graphene oxide is found to increase the photostability to Fe_3O_4@g-C_3N_4/RGO and showed enhanced photocatalytic performance on tetracycline degradation[72]. Further, the sandwich-like TiO_2-rGO composite was fabricated via Pickering emulsion approach, where the TiO_2 nanoparticles were closely and densely packed on rGO sheets (**Figure 2.14**). This unique structure significantly enhanced the light absorption, accelerated the charge separation and improved the adsorption capacity of antibiotic, thereby increased the photocatalytic removal of tetracycline under visible light around, which was around 94% in 40 min[73].

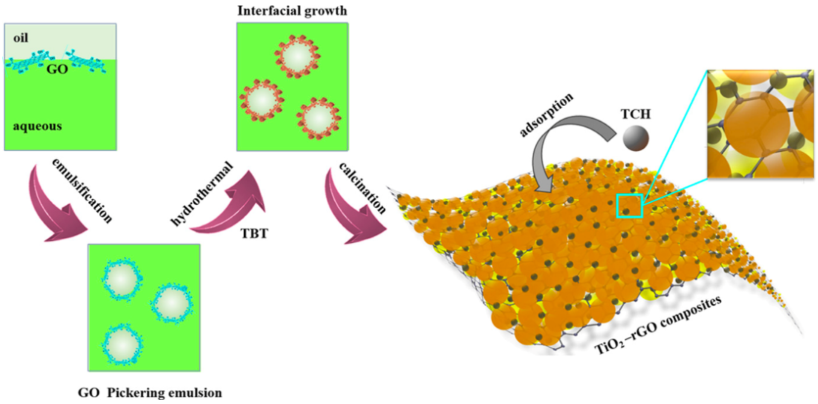

Figure 2.14. Fabrication of the TiO_2-GO composite by Pickering emulsion method[73].

A highly efficient and stable Ag_2MoO_4/Ag/AgBr/GO heterostructure photocatalyst was demonstrated an excellent charge separation and photocatalytic performance. Consequently, the antibiotic tetracycline hydrochloride was completely degraded within 75 min by Ag_2MoO_4/Ag/AgBr/GO heterostructure, which is 1.36 times higher photocatalytic efficiency than that of without GO based Ag_2MoO_4/Ag/AgBr heterostructure composite. Because of the graphene oxide that acted as an efficient electron acceptor, where it also prevented the metallic silver exchange into silver ions thereby improving the stability of the heterostructure photocatalyst[74].

ii) Carbon quantum dots photocatalysts

In recent years, the semiconductor-carbon quantum dot composites have also been received more interest in photocatalysis due to their distinct electronic properties. In this direction, the carbon quantum dots (CQDs) possess many unique properties such as (i) excellent charge transport properties, which can enhance photogenerated electron-hole separation and reduce recombination process (ii) the extension of the excitation wavelength into visible light region, acting as photosensitizers (iii) possible to act as either electron acceptor or electron donor. Therefore, fabrication of semiconductor-CQDs composites would provide enhanced photocatalytic activity[75, 76]. For example, carbon quantum dots-loaded mesoporous g-C_3N_4 (mpg-C_3N_4/CQDs) was found to show synergistic absorption effect and higher visible photodegradation of fluoroquinolones antibiotic ofloxacin (90.1% degradation). The mpg-C_3N_4/CQDs composite introduced a larger number of adsorption sites, exclusive up-converted photoluminescence properties and efficient charge separation in order to improve the degradation of ofloxacin, a fluoroquinolone antibiotic[77]. The photocatalytic performance of CQD modified-Bi_2MoO_6 was explored on the degradation of ciprofloxacin and tetracycline hydrochloride under visible light. The well-distribution of CQDs (~7 nm) on Bi_2MoO_6 nanosheet surface enhanced the photocatalytic activity and found to have 5.7 times higher ciprofloxacin degradation efficiency than that of pure $BiMoO_6$. The CQDs were played a major role on the observed superior photocatalytic activity of CQD-$BiMoO_6$ composite. In this system, the CQDs essentially acted as a photocenter for light absorbance as well as the charge centers towards improving the charge separation and reducing the charge recombination and thereby enhanced the antibiotic degradation[78]. More interestingly, Ag^+-CDs-Bi_2WO_6 ternary composites with excellent solar-light-driven photocatalyst activity were studied on tetracycline degradation. The CDs (carbon dots) were uniformly spread on Bi_2WO_6 nanosheets surface, where it also potentially performed as the efficient electron acceptors. The coexistence of CDs and Ag^+ significantly improved the photogenerated electron-hole pairs separation and distinctly improved visible light absorbance (**Figure 2.15**). It facilitated a superior photocatalytic activity towards the tetracycline degradation with 91.33% removal efficiency in 10 min and complete degradation was achieved in 20 min[79].

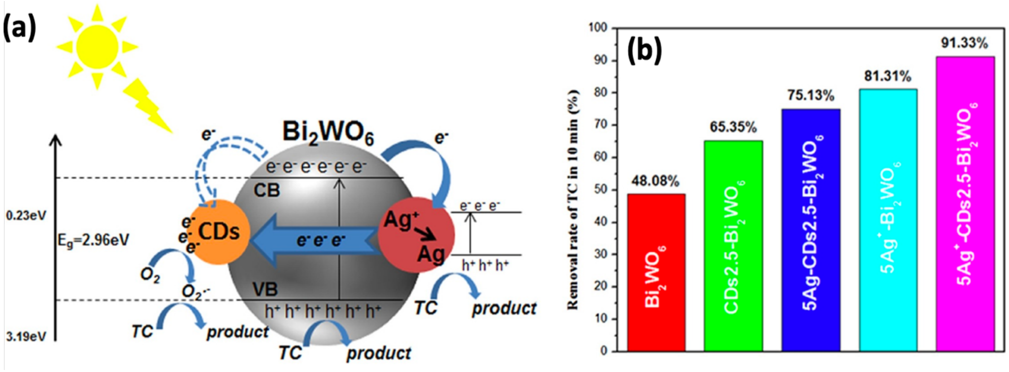

Figure 2.15. (a) Photocatalytic mechanism of Ag^+-CDs-Bi_2WO_6 and (b) photocatalytic removal efficiency of tetracycline with different catalyst in 10 min under solar light[79].

Further, 2-4 nm sized CQDs were well dispersed on dandelion-like ZnS surface and found to have higher photocatalytic activity on ciprofloxacin removal under simulated sun light. The optical and electrochemical results were proved that the enhancement of photocatalytic activities assigned to improved electron-hole charge separation efficiency by CQDs. Because of the smaller size, carbon quantum dots (CQDs) can be uniformly distributed and can establish well contact onto the semiconductor surface, which built bulk-to-small surface channels and excellent charge transport ability[80].

2.6 Bismuth materials

The development of new hybrid photocatalysts with proper counterparts and design is highly required for effective removal of antibiotics from water. The new photocatalyst can offer significant advantages over traditional photocatalytic materials such as interesting visible/solar absorption, narrow band gap, fast and efficient charge transfer, higher redox potential, and higher surface and catalytic properties. Recently bismuth-based materials such as metal bismuthate, bismuth vanadate and bismuth tungstate have received significant interest in photocatalysis due to its unique structure, electronic and physical properties, which offer interesting visible light absorption, better charge separation and high photostability[81-83]. Hence, the development of bismuth-based nanostructured and nanocomposite photocatalysts could possibly offer high photocatalytic performance towards antibiotic degradation.

2.6.1 Metal bismuthates

Metal bismuthates $MBiO_3$ (M = Ca, Cd, Mg and Zn) are theoretically proposed perovskite structured ferroelectric oxides, which can be operated under visible light irradiation. The $MBiO_3$ exhibits small band gap (~2.0 eV), strong visible-light absorption, small carrier effective masses and large electrical polarization. $MBiO_3$ materials are taking more advantage towards photocatalytic application due to their effective Bi^{3+}/Bi^{5+} charge disproportionation and small radii of M-site cations in the $MBiO_3$ compounds. Besides, the designing of small band gap ABO_3 ferroelectric oxides by combining of small A-site cations such as Mg^{2+}, Zn^{2+}, Cd^{2+} and Ca^{2+} with larger B-site cation of bismuth was favoring to higher the charge ordering and better light absorption, specifically disproportionation of Bi^{4+} into Bi^{3+}/Bi^{5+}. Also, $MBiO_3$ offers the ferroelectric compounds with smaller tolerance factor (τ) and the band edges formed by the 6s-like states derived from the Bi^{3+} and Bi^{5+} cations. The spatially extended 6s orbitals of Bi^{3+} and Bi^{5+} cations should guarantee a high photogenerated carrier mobility as observed in similar material. The band gap reduction in these-system is mainly due to the stereo-chemically active lone pair of Bi^{3+} 6s shifting the top of the valence band to higher energy, which does not affect the redox processes during photocatalytic process. Therefore, the development of new bivalent $MBiO_3$ ferroelectric perovskite materials are possibly potential candidate for photocatalytic oxidation of pharmaceutical pollutants[84]. Recently, we have developed for the first-time calcium bismuthate ($CaBiO_3$) perovskite material with distinct Bi^{3+} and Bi^{5+} multi-charge disproportion (**Figure 2.16**) via glycine-complexation and ion-exchange methods.

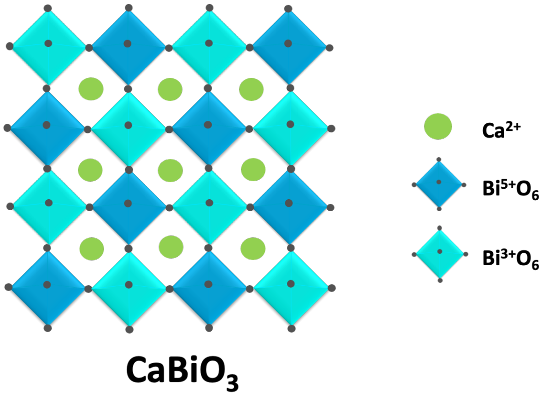

Figure 2.16. $CaBiO_3$ perovskite material with distinct Bi^{3+} and Bi^{5+} charge disproportion[13].

The as-developed $CaBiO_3$ found to have an efficient Bi^{3+}/Bi^{5+} charge disproportion and well-established BiO_6 octahedral crystal arrangement, where it also offered an efficient visible photo-absorbance and higher photo-generated charge carrier generation and separation. Moreover, the effective Ca^{2+} incorporation into bismuthate **(**BiO_6**)** crystal lattices potentially modified band structure and band potential of $CaBiO_3$, which offered more suitability for photocatalytic redox properties. Also, the developed nanostructured $CaBiO_3$ materials offering higher surface area resulting in enhanced surface properties for the improved catalytic reactions. Furthermore, the developed $CaBiO_3$ materials have also been potentially explored on the degradation of antibiotic contaminants under solar light[85].

2.6.2 Bismuth vanadate

Bismuth vanadate ($BiVO_4$) is a narrow band gap semiconductor, and its tunable structural and electronic properties provide excellent photocatalytic activity and photostability to the system. The photocatalytic activity is strongly depended on the crystal structure of the material. The $BiVO_4$ exists in three different crystal structure such as monoclinic scheelite, tetragonal scheelite and tetragonal zircon. Among them, the monoclinic $BiVO_4$ with a narrow band gap of 2.4 eV reveals superior photocatalytic performance than other crystalline phases[82]. The electronic structure of $BiVO_4$ exists with Bi 6s and O 2p in the valence band and V 3d states with minor contributions of Bi 6p and O 2p in conduction band. The $BiVO_4$ shows a greater visible photocatalytic performance due to Bi-O dodecahedral distortion and their distinct overlap of O 2p and Bi 6s orbitals in the valence band is a benefit for the higher mobility of photogenerated charge carriers and reducing band gap of $BiVO_4$[86, 87]. For example, quantum sized monoclinic $BiVO_4$ displayed size depended optical and photophysical properties. As-compared to nano-$BiVO_4$, the quantum-$BiVO_4$ exhibits increased band gap value due to the negative shift of conduction band edge by a quantum confinement effect of $BiVO_4$ as shown in **Figure 2.17**.

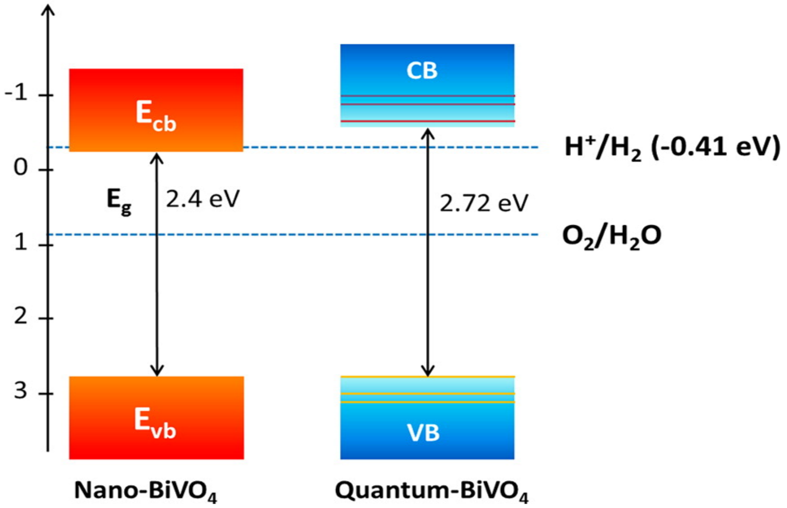

Figure 2.17. The band structures of nanoscale-$BiVO_4$ and quantum-$BiVO_4$[90].

This property offered excellent photocatalytic activity to quantum-$BiVO_4$ for the overall water oxidation without cocatalyst under solar light irradiation. Also, it proved that the photocatalytic performance was improved by tuning particle size of $BiVO_4$[88]. Further, the well-defined monoclinic $BiVO_4$ nanoplates was synthesized without using any template or organic surfactant by facile hydrothermal route. As-prepared m-$BiVO_4$ nanoplates displayed an efficient visible photocatalytic activity towards the degradation of organic contaminants and photocatalytic water oxidation. The nanostructure designing with suitable surface structures significantly enhanced visible photocatalytic activity of the material[89].

2.6.3 Bismuth tungstate

Bismuth tungstate (Bi_2WO_6) is a layer structured material which comprises of layered $[WO_4]^{2-}$ between bismuth oxide $[Bi_2O_2]^{2+}$ layers. Due to its unique layered structure and ideal band structure, it retains several advantages especially in photocatalytic applications. The perfect band structure offers suitable visible light absorption, and their layered structure leads to the efficient photogenerated electron-hole pairs separation, which can be ascribed to high photocatalytic activity and good stability. The conduction band of Bi_2WO_6 possess W 5d orbital and valence band comprises of hybridization of the O 2p and Bi 6s orbitals[90]. Upon photoexcitation, such band structure allows charge transfer from the O 2p and Bi 6s hybrid orbitals to the empty W 5d orbitals as indicated in **Figure 2.18**. The largely dispersed valence band resulted in narrow band gap (2.8 eV) of Bi_2WO_6 material, and it also favors higher photogenerated hole and electron mobility. Therefore, visible light driven Bi_2WO_6 photocatalysts have received extensive attention in photocatalytic applications.

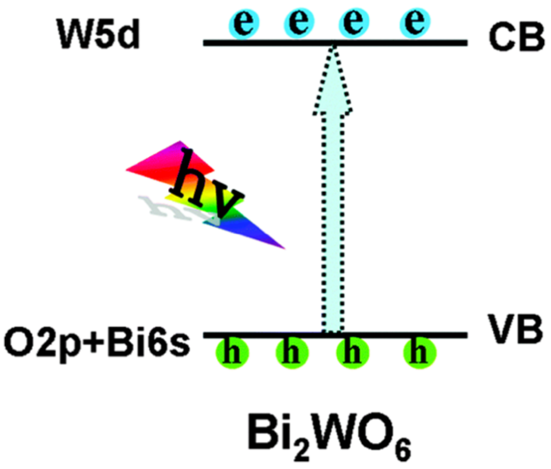

Figure 2.18. Band structure of the Bi_2WO_6 materials[93].

For example, the Bi_2WO_6 monolayer with $[BiO]^+$-$[WO4]^{2-}$-$[BiO]^+$ sandwich substructure was developed by CTAB-assisted self-assembly route. The sandwich structure established heterojunction interface with oxygen-depleted surface, and it offered an ultrafast photogenerated charge carrier separation and highly reactive surface. Hence, the monolayer catalyst surface generated a greater number of photogenerated holes which initiated an excellent organic pollutant degradation. Also, the monolayer Bi_2WO_6 formation showed an efficient visible light absorbance due to their narrow bandgap[83]. Similarly, the ultrathin Bi_2WO_6 photocatalyst presented an excellent catalytic performance in organic pollutant degradation and water splitting. Hence, the two-dimensional morphology with superior electronic properties introduced fast hole transport delivering stronger oxidation ability to ultrathin Bi_2WO_6. In addition, the ultrathin layered structural property of fast photogenerated charge carrier migration to the surface promisingly reduce the charge recombination rate and improve the photocatalytic activity[36]. The mesoporous single-crystal-like Bi_2WO_6 with integrated tetragonal architecture was developed by mixed molten salt method, the synergistic effect of metal precursors and electrostatic attraction of crystal structure played vital role in the construction of mesoporous Bi_2WO_6 architecture. The unique architecture efficiently altered their physical properties of mesoporous Bi_2WO_6 thus enhance the charge separation efficiency and lifetime of electron and hole pairs. Hence, the developed photocatalytic material found superior photocatalytic performance in organic pollutants degradation and oxygen evolution under visible light[91].

Chapter 3 : Characterization techniques

3.1 X-ray diffraction analysis

X-ray diffraction (XRD) technique is commonly used to analyze and describe the crystallographic structure and phases of materials. An X-ray source that produces X-rays by directing a high-voltage electron beam at a metal target anode within an evacuated X-ray tube (**Figure 3.1 a**). The detector will count the number of X-ray photons of a specific energy for each 2θ angle, which is proportional to reflection of the peak intensity. The XRD pattern is made up of a series of intensity peaks that vary in intensity as a function of angle. The peak positions depend on the crystal structure of the material, which includes the shape and size of the unit cell. Furthermore, each peak in the spectrum is associated with a particular atomic d spacing. Typically, X-ray diffraction occurs as X-ray photons are elastically scattered by atoms in a periodic lattice. Constructive interference is generated by scattered monochromatic X-rays in phase. According to Bragg's law, the constructive interference arises only when the path length difference between two or more beams diffracted in the same direction is an integer multiple of the wavelength (**Figure 3.1 b**).

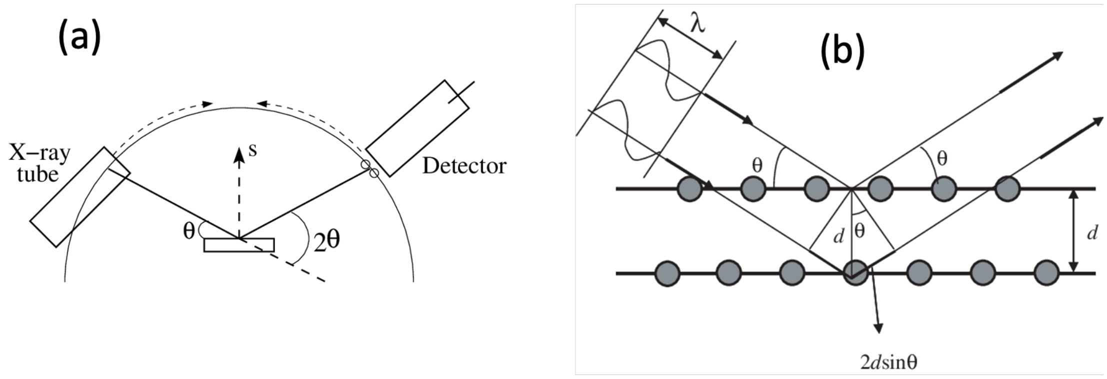

Figure 3.1. (a) X-ray diffraction instrument and (b) Schematic illustration of the Bragg's law.

The difference in path length is determined by the atomic lattice spacing and the sine function of the angle between the incident and scattering angles. Bragg's law of diffraction states that the relationship between the angles measured for each peak and the corresponding d spacing.

$$n\lambda = 2d \sin\theta$$

where n is an order of the interference, λ is the wavelength of the X-rays (nm), d is the distance between two lattice planes (nm), θ is the angle between the incoming X-rays and the normal to the reflecting lattice plane (degree).

3.2 Electron microscopy

Electron microscopy (EM) is an indispensable powerful technique to characterize micro and nanoscale materials, as it provides detailed information on the size and morphology of materials. In principle, electron microscopes investigate structures on a very fine scale using a beam of highly energetic electrons. The high energy beam interacts with the atoms in a material, incident electrons undergoes either elastic or inelastic scattering resulting in the electron emission and transmission (**Figure 3.2**).

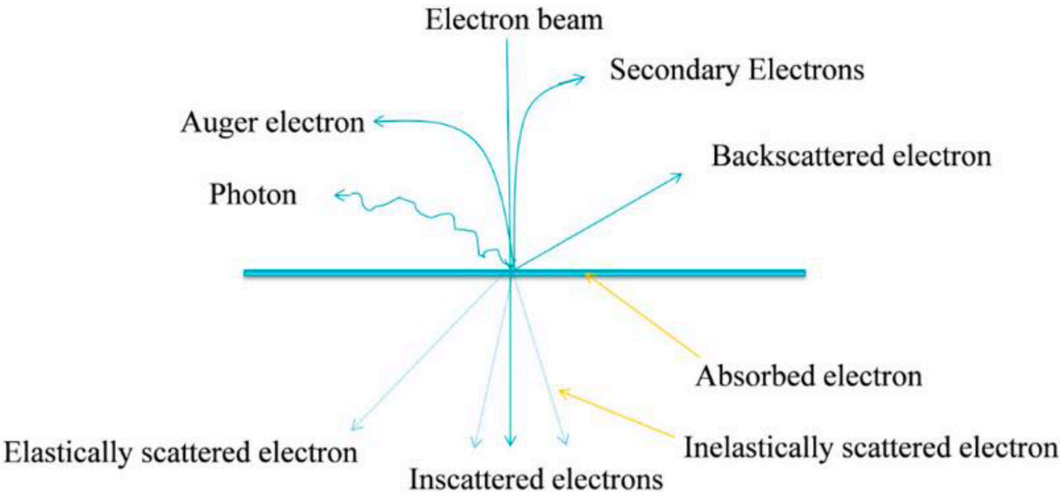

Figure 3.2. The working principle of electron microscope.

Generally, electron microscopes are classified into two types: scanning electron microscopy (SEM) and transmission electron microscopy (TEM), which are distinguished based on their imaging concepts and specimen shapes. The scanning electron microscopy works based on the electron emission process, while transmission electron microscopy operates on electron transmission. The SEM technique analyze morphology of microstructure and nanostructure material by scanning its surface by high resolution with great depth. In principle, highly accelerated electrons beam focused onto a small region sample specimen to hit out the secondary electrons or backscattered electrons. These generated backscattered electrons from material surface produces electronic signals, which are converted into images. The secondary electron signal intensity is greatly dependent on the shape and the chemical composition of the sample. The transmission electron microscopy is a distinctive technique providing high-resolution images of objects when an electron beam interacts and transmit through the specimen. In principle, the accelerated high energy electron beam passes through a thin-section specimen of sample, the electron beam undergoes to scattering and transmission. The transmitted and scattered electrons can be coupled to create interfering high-resolution images. The irradiated specimen must be small enough to enable electron transmission and the electron beam must have a high energy to transmit electrons.

In high-resolution transmission electron microscopy (HR-TEM) both transmitted and the scattered electrons can be combined to generate interfering images that is as small as a unit cell of the crystal. This technique can provide images of the crystal structures and lattice imperfections on the atomic scale of the materials. The elemental and chemical composition of a selected part of the material is characterized by energy-dispersive X-ray analysis (EDX or EDS). In this process, when the high energy electron beam strikes on sample surface, the core electrons are ejected from the atoms and generate electron vacancy. Then the created electron vacancy in the lower shell is filled by an electron from a higher shell and the energy difference between the two shells is emitted in the form of X-ray. Also, the energy of the emitted X-ray depends on the atomic structure of the elements from which they were emitted allowing the elemental composition of the specimen to be measured.

3.3 X-ray photoelectron microscopy

X-ray photoelectron microscopy (XPS) is a powerful surface chemical analysis technique for determining the chemical composition and chemical state of the elements in the surface region. XPS functions based on the photoelectric effect, while X-Ray beam is directed to the sample surface, the high energy of the X-ray photon is adsorbed by the core electron of an atom and causing electron emission (**Figure 3.3**). The emitted electron is defined as the photoelectron, which break the nuclear attraction force at the core level and escaping from the surface into the surrounding.

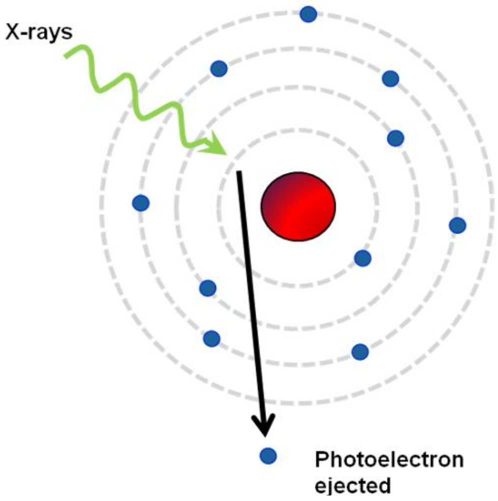

Figure 3.3. The mechanism of photoelectron emission in X-ray photoelectron spectroscopy.

The electron analyzer captures these ejected photoelectrons and measure their kinetic energy E_k (eV). The kinetic energies of ejected photoelectrons are not only characteristic of the atoms of the element, but it also reveals details about chemical states of the atom. The XPS spectrum plot the signals of the photoelectron versus binding energy. Further, the Einstein's relationship determines the binding energy of the core electron.

$$E_k = h\nu - E_b - \varphi$$

where E_k is the kinetic energy of the photoelectron; h is Planck's constant, ν is the frequency of the exciting radiation, E_b is the binding energy of the photoelectron with respect to the particular Fermi level and φ is the surface work function.

3.4 Nitrogen physisorption

The nitrogen physisorption equilibrium isotherms are used to measure the specific surface area, pore size, pore size distribution and porosity of solid materials. This measurement technique allows the physical adsorption of nitrogen or helium gases onto the catalyst surface at low constant temperature (atmospheric boiling point of nitrogen or helium) to estimate their surface area. It measures gas adsorption by increasing partial pressure and desorption by decreasing partial pressures on the materials. The adsorption-desorption isotherms resulting corresponds the relationship between volume of nitrogen adsorbed and desorbed vs relative pressure at constant temperature. The isotherm is the plot of adsorbed volume at the standard pressure against the corresponding equilibrium pressure (P/P_o) at a constant temperature. The specific surface area is calculated by adsorption isotherms that relate the volume adsorbed to the relative pressure. The Brunauer-Emmett-Teller (BET) theory is the widely used to estimate the surface area of the porous material. Further, the nature of the isotherms mainly depends on the porous structure of the materials. As per international union of pure and applied chemistry (IUPAC) estimation the isotherms are classified to six types (**Figure 3.4**).

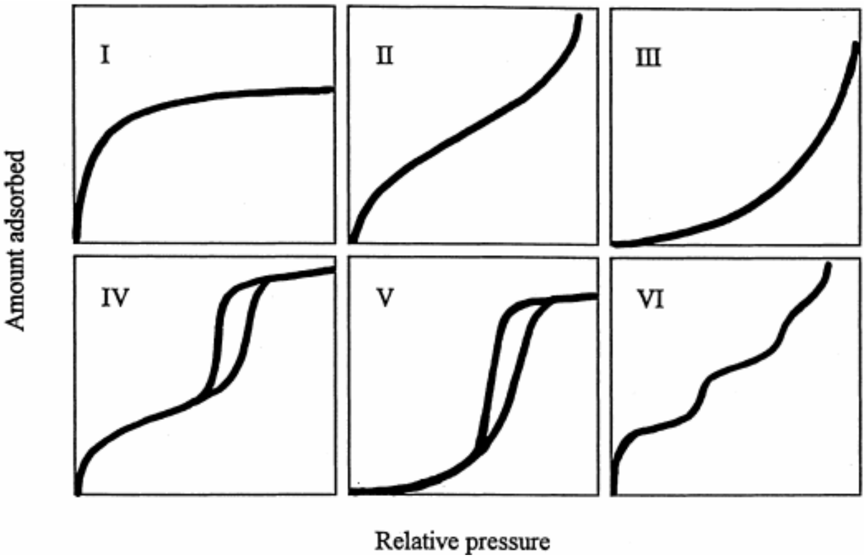

Figure 3.4. Types of physisorption isotherms.

The type I isotherms are found in microporous materials, while type II and III isotherms distinguish nonporous or macroporous materials in which adsorption occurred by multilayer formation. Type IV and V isotherms characteristic mesoporous materials with multilayer adsorption consisting of capillary condensation. Type VI isotherms represents uniform nonporous surface, which allows stepwise multilayer adsorption.

3.5 Fourier transform infrared spectroscopy

Fourier transform infrared spectroscopy (FTIR) is a well-known spectroscopy tool to identify chemical functional groups of materials. The infrared spectroscopy studies the changes in vibrational and rotational motions of molecules resulting in functional group identification

(**Figure 3.5**). It is used to prove the presence or absence of functional groups in the materials. The infrared radiation induces vibrational and rotational excitation in the molecular bonds of material under infrared radiation with frequency range of 400 to 4000 cm^{-1}. The specific chemical groups correspond to specific wavelength of infrared light and generate distinct vibration frequencies. Also, each chemical bond with multiple vibrational modes, such as stretching and bending modes can absorb multiple infrared frequencies with varying intensities. Stretching absorptions produce stronger peaks than bending absorptions, but the weaker bending absorptions help distinguish between similar types of bonds. The plot of percentage transmittance against frequency (wavenumber) creates the infrared spectrum of the sample or compounds.

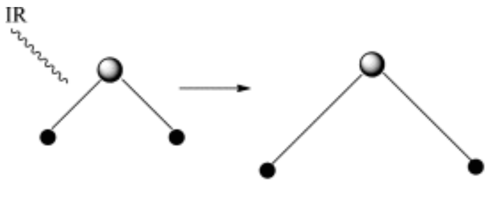

Symmetric stretching vibration

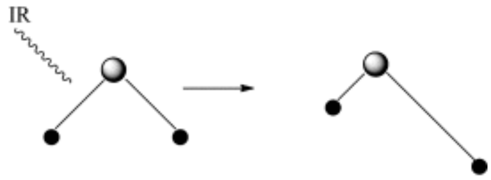

Asymmetric stretching vibration

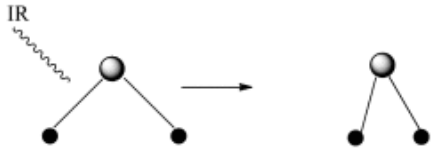

Bending vibration

Figure 3.5. The types of vibration in infrared spectroscopy.

3.6 UV-visible spectroscopy

UV-visible spectroscopy (UV-Vis) is a very useful characterization technique to measure optical properties such as absorption, transmission and reflectance of materials. In principle, the material interacts with photons and undergoes wavelength dependent electronic transitions (**Figure 3.6**). The material undergoes photo absorption and electronic transitions thereby electrons move from their ground states to higher energy excited states in the wavelength range of 200 to 800 nm. The intensity of absorbed or transmitted or reflected photons is analyzed as a function of wavelength. This technique offers a quantitative measurement of the wavelength dependent optical properties from light-matter interactions.

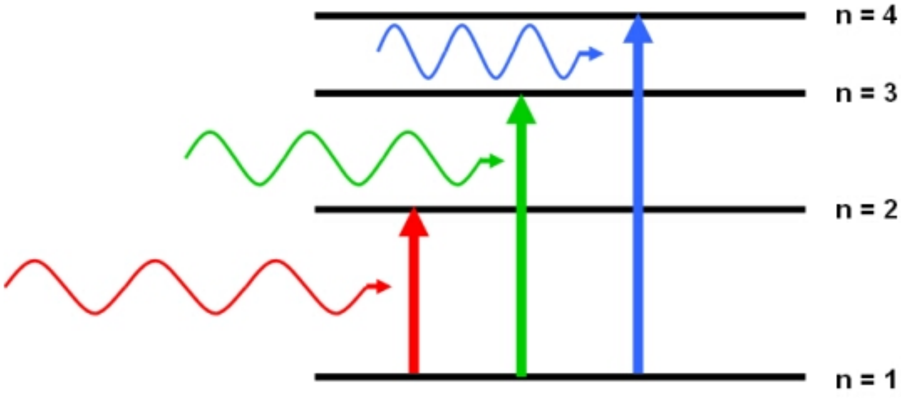

Figure 3.6. The wavelength dependent electronic transitions of materials.

UV-vis spectroscopy widely used to investigate diffuse reflectance and absorbance properties of the materials. The UV-vis diffuse reflectance spectroscopy is used to characterize solid state material, functioning based on amount of light reflection by the material. The absorbance of solid material estimated by the function of reflectance versus wavelength. UV-vis absorbance technique is mainly utilized to analyze liquid sample, it's evaluates based on the difference between the incident and transmitted light efficiency of the solution. The material concentration is estimated by linear relation between the absorbance versus wavelength. Moreover, the information derived from the UV-vis spectrum can be used to estimate the material's band gap.

3.7 Photoluminescence

Photoluminescence (PL) spectroscopy is a valuable technique for getting information about material electronic structure and optical properties, as well as study photochemical properties of charge carrier capture, migration and transfer efficiency. **Figure 3.7** explains the basic concept of photoluminescence, the emission of radiation late the photon absorption is known as photoluminescence.

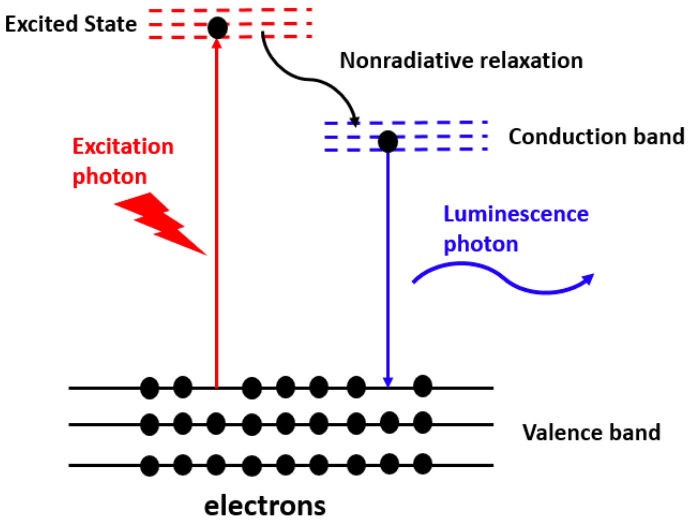

Figure 3.7. The basic mechanism of photoluminescence spectroscopy.

It can be represented quantum mechanically as an excitation to a higher energy state followed by a return to a lower energy state with the emission of a photon. The material absorbs a photon with a higher energy than its bandgap, followed by the electron-hole pair generation. Due to their unstable properties, the excited electrons from bottom of the higher energy level quickly return to the top of the lower energy level to recombine with the existing holes. The recombination of photoinduced charge carriers could emit energy as irradiation resulting in luminescence emission, this phenomenon is known as photoluminescence. The time between absorption and emission is very short, lesser than ten nanoseconds. The luminescence intensity reveals rate of photogenerated charge carrier recombination efficiency, and also emitted photon energy is equivalent to the bandgap energy of the material.

3.8 Photoelectrochemical study

The photoelectrochemical (PEC) technique is a potential characterization technique to study the electronic properties of semiconductor based photocatalytic materials. The charge carrier's separation and transfer ability are evaluated by transient photocurrent and electrochemical impedance study. Also, this technique can be used to estimate band position of semiconductor materials from Mott-Schottky plots. A typical photoelectrochemical cell consists of a three-electrode system which includes working electrode, counter electrode and reference electrode as shown in **Figure 3.8**.

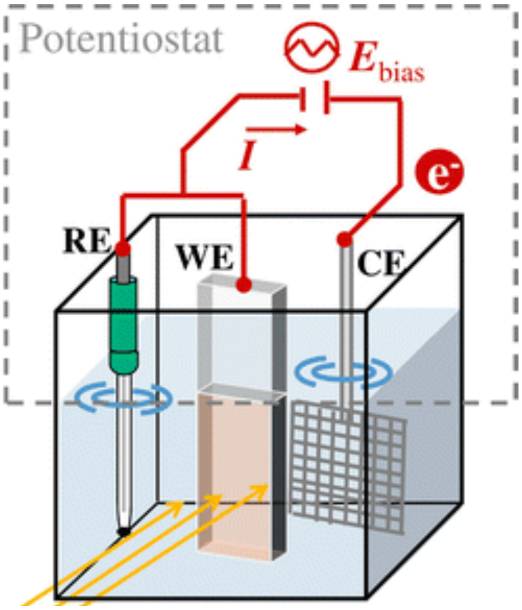

Figure 3.8. The basic setup of photoelectrochemical system.

Typically, the photoinduced electron-hole pairs are generated at working electrode in the presence of an electric field. Afterward the photogenerated electrons are transferred to the metal-based counter electrode, while the photogenerated holes move to the semiconductor/electrolyte interface. Generated transient photocurrent and their intensity can be used to characterise photoinduced charge carrier generation and separation of materials. Further, the electrochemical impedance provides the charge transfer efficiency of semiconducting materials, which can be obtained by measuring materials charge resistance via Nyquist plot.

Chapter 4 : Calcium bismuthate ($CaBiO_3$): a prospective sunlight driven perovskite photocatalyst for the degradation of emerging pharmaceutical contaminants

K. Rokesh, M. Sakar, Trong-On Do*

Department of Chemical Engineering, Laval University, Québec (Québec), G1V 0A6, Canada

*E-mail: trong-on.do@gch.ulaval.ca

This chapter is published in ChemPhotoChem 2020, 4, 373-380

Résumé

Cette étude est la première qui a montré l'efficacité photocatalytique de $CaBiO_3$ (CBO) vis-à-vis la dégradation des contaminants émergents (CEC) tels que la ciprofloxacine et la tétracycline sous l'irradiation de la lumière solaire. $CaBiO_3$ a été synthétisé en utilisant des méthodes de complexation de la glycine (GC) et d'échange d'ions (IE). La différence structurelle de ces différentes méthodes a été mise en évidence par des résultats XRD et XPS, vu le double état d'oxydation de Bi ($Bi^{3+/5+}$) dans $CaBiO_3$. Le CBO synthétisé par la méthode GC (CBO-GC) a montré une large gamme d'absorption UV-visible de 200 à 550 nm et une énergie de bande interdite de 2,30 eV, alors qu'elles ont été trouvées de 200 à 450 nm et de 2,65 eV pour le CBO synthétisé par la méthode IE (CBO-IE). Le potentiel VB de CBO-IE a été décalé vers une valeur plus positive (+2,45 eV) par rapport au CBO-GC (+1,90 eV) et ainsi le potentiel CB calculé de CBO-GC et CBO-IE a été trouvé respectivement -0,40 et-0,20 eV. Une telle position de niveau d'énergie de VB et CB a favorisé la génération de radicaux hautement réactifs pour une dégradation efficace des polluants. Ce positionnement relatif des bandes d'énergie pourrait être établi par les défauts surfaciques créés par les lacunes d'oxygène dans le matériau en raison du double état d'oxydation du Bi. Les mesures de photocourant et d'impédance ont démontré une excellente séparation des charges et une faible résistance dans le CBO-GC par rapport au CBO-IE. Par conséquent, le CBO-GC a montré une dégradation photocatalytique favorisée, ainsi qu'une photo-stabilité et une réutilisabilité améliorée par rapport à celles de CBO-IE.

Abstract

This study is first to report the photocatalytic efficiencies of $CaBiO_3$ (CBO) towards the degradation of the contaminants of emerging concern (CEC) such as ciprofloxacin and tetracycline under the solar light irradiation. $CaBiO_3$ was synthesized using glycine-complexation (GC) and ion-exchange (IE) methods. The structural difference by these different methods was evidenced from XRD and XPS results, due to the induced-dual oxidation state of Bi ($Bi^{3+/5+}$) in $CaBiO_3$. The CBO synthesized by GC method (CBO-GC) showed a broad UV-visible absorption range from 200 to 550 nm and band gap energy of 2.30 eV, while it was found to be 200 to 450 nm and 2.65 eV for the CBO synthesized by IE method (CBO-IE). The VB potential of CBO-IE is shifted towards more positive (+2.45 eV) as compared to the CBO-GC (+1.90 eV) and thereby the calculated CB potential of CBO-GC and CBO-IE was found to be -0.40 and -0.20 eV respectively. Such positioning of the VB and CB favored the generation of highly reactive radicals towards the effective degradation of the pollutants. These relative alignments of the bands could be mediated by the oxygen vacancy-defects in the systems owing to the dual oxidation state of Bi. The photocurrent and impedance measurements demonstrated excellent charge separation and lower resistivity in CBO-GC as compared to the CBO-IE. Accordingly, the CBO-GC showed enhanced photocatalytic degradation efficiency, improved photostability and reusability as compared to that of the CBO-IE.

4.1 Introduction

The early detection and degradation of pharmaceuticals compounds in the water bodies has become important considering their toxicity and potential hazardous to the ecosystems and the lives on the planet[4, 5]. Among these pharmaceutical compounds, the antibiotic chemicals receive the most serious attention, as they can lead to the serious health issues through the production of antibiotic-resistant bacteria's and antibiotic resistant genes, etc., which essentially have the ability to reduce the immunity of humans and animals to diseases. More importantly, the antibiotic resistant bacteria-mediated infections are no longer sensitive to antibiotic treatment, which could pose a serious threat to human's health[7, 92]. Hence, the antibiotic residuals are considered as an emerging pharmaceutical contaminant and therefore, there is an urgent need to find a process to degrade them when they get released and disposed into the environment, especially in water bodies[9, 93, 94]. In this direction, photocatalysis has been widely studied for the degradation of organic and pharmaceutical pollutants present in the water bodies[15]. In the past few decades, a wide range of photocatalytic materials has been developed and explored for fast and efficient degradation of pharmaceutical pollutants, especially antibiotics[48, 51, 57, 95]. However, the development of potential photocatalytic materials for such application is always being a challenge considering the various scientific and technological parameters of the process. In such aspects, perovskites are the class of materials that essentially provide the required features such as tunable band structure, photo-stability, etc for the effective photocatalytic process[96-98]. As compared to binary oxides, several perovskite materials have demonstrated the sufficient cathodic conduction band energies for photocatalytic reduction process. In addition, one of the special features of perovskites, which is ferroelectricity or piezoelectricity, is greatly helpful in many different ways toward enhancing the photocatalytic process via increasing the charge separation, enhancing the surface adsorption of pollutants and charge transportations for the effective photocatalytic activities[99, 100]. Perovskite materials are feasibly active in UV and visible light region; however, the visible light active perovskite materials are gained importance for their cost-effective practical applications. There are variety of visible light driven perovskites such as titanates, tantalites, nibotates, ferrites are formerly developed and well-studied for the photocatalytic applications[101].

Recently, bismuth-based perovskite photocatalysts are widely explored in a greater extent because of their unique photophysical properties and they offer a potential visible light absorption and enhanced photo-induced charge separation. Notably, the bismuth-based perovskite compounds can be established and stabilized in pentavalent oxidation state (Bi^{5+}) in the following Bi-based perovskites $MBiO_3$ (M = Li, Na, K, Ag)[102-105], whereas the dual-oxidation state bismuth-based perovskites (Bi^{3+} and Bi^{5+}) tend to show the greater photocatalytic efficiencies as compared to the mono-oxidation bismuth[81, 84, 106, 107]. It should be noted that the bismuth ions (Bi 6s orbital) involve in the effective formation of band energy structures in $MBiO_3$ systems and it has become predominant when Bi ions possess dual oxidation states, where the Bi^{3+} 6s ions and Bi^{5+} 6s ions specifically involves in the formation of VB and CB respectively[84, 108], which essentially lead to the tunable properties in $MBiO_3$ structures. However, the increased dual-oxidation states of Bi can lead to the creation of more oxygen vacancy-defects in the system and it may affect the properties of $MBiO_3$[109, 110]. Therefore, the optimal concentration of dual oxidation states of Bi should be meticulously engineered in the system.

In this direction, the calcium bismuthate with chemical formula of $CaBiO_3$ is theoretically proposed as a single-phase ferroelectric perovskite oxide, which could be active under visible light irradiation. $CaBiO_3$ (CBO) shows small tolerance factor (τ) with the band edges made up by 6s states derived from the Bi^{3+} and Bi^{5+} cations[111]. In addition, the band gap of CBO is relatively narrow as compared to the other typical transition metal oxides with d^0 electronic configurations and hence the CBO shows the better solar light absorption properties. The spatially extended 6s orbitals of Bi^{3+} and Bi^{5+} cations are found to be the origin for the high mobility of photogenerated carriers as observed in the case of $BaBiO_3$[84, 111]. With this theoretical basis, herein, we have developed the multivalent charge disproportioned $CaBiO_3$ (Bi^{3+} and Bi^{5+}) using two different synthesis routes known as glycine-complexation (GC) and ion-exchange (IE) methods. Unlike the traditional ion-exchange method, the glycine complexation process can potentially develop the charge disproportioned-CBO and decrease the structural defects thereby it improves the optical, structural, crystalline and photoinduced charge carrier mobility properties of $CaBiO_3$. Further, the synthesized $CaBiO_3$ systems have also been investigated for their photocatalytic efficiencies under solar light towards the degradation of the pharmaceuticals antibiotic pollutants such as ciprofloxacin and tetracycline, which are classified as the contaminants of the emerging concern, where they could often be found in the water bodies.

4.2. Materials and methods

4.2.1 Chemicals

The precursor chemicals such as bismuth nitrate pentahydrate (98%), calcium nitrate tetrahydrate (99%), glycine (99%), polyvinylpyrrolidone (MW-10000), ammonium hydroxide (28%) and nitric acid (68-70%) were procured from the commercial sources and used without any further purifications.

4.2.2 Synthesis of $CaBiO_3$

The $CaBiO_3$ (CBO) was prepared by novel glycine-complexation[112] method and conventional ion-exchange method[109].

4.2.2.1 Glycine-complexation method

In this process (as shown in **Scheme 4.1**), 10 mL of 0.1 M $Ca(NO_3)_2{\cdot}4H_2O$ and $Bi(NO_3)_3{\cdot}5H_2O$ (dissolved in diluted nitric acid) solutions were mixed together with 20 mL of deionized water and stirred for 0.5 h, followed by the addition of 900 mg of glycine and 300 mg of PVP (MW-10000). The mixture was continued for stirring for 0.5 h to ensure that all the precursors were dissolved completely. To this, few mL of NH_4OH solution was added to adjust the pH of the mixture to be around ~8.0. Then, the solution was transferred into 150 mL Teflon coated autoclave and kept at 180 °C for 12 h in a hot air oven. After the reaction time, the obtained solid product was centrifuged and washed with deionized water for several times and dried at 60 °C for 12 h to obtained grayish brown powder. Finally, this as-synthesized powder was calcinated at 450 °C for 4 h to obtain the $CaBiO_3$ (CBO-GC), which appeared greenish yellow in color.

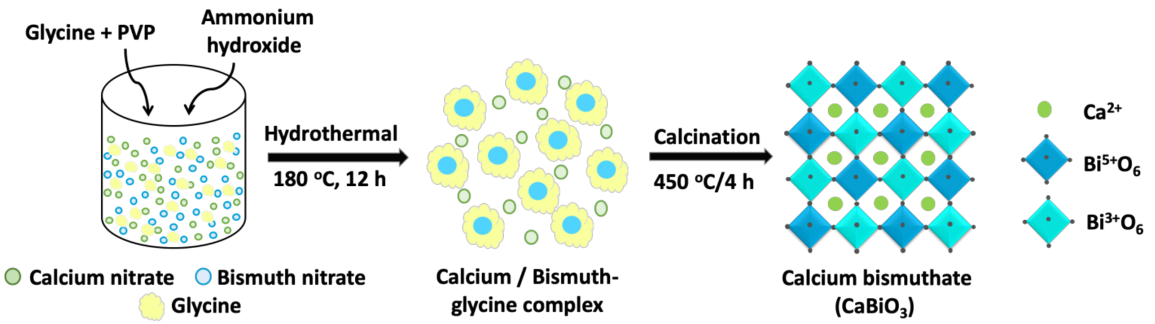

Scheme 4.1. Synthesis of $CaBiO_3$ by the glycine-complexation method.

4.2.2.2 Ion-exchange method

In this typical process (as shown in **Scheme 4.2**), 5 mmol (1.4 g) of $NaBiO_3.2H_2O$ was well dispersed in 100 mL of deionized water by ultra-sonication. To this, 0.5 mL of HCl solution was added dropwise, where the hydrolysis reaction was taken place and led to the formation of yellow precipitate and then finally to the light brown precipitate. Afterward, 5 mmol (0.82 g) of $Ca(NO_3)_2$ was dissolved in 100 mL of deionized water and drop-wise added into the above bismuthate mixture and stirred for 2 h. After this process, the solution mixture was transferred into a 150 mL Teflon coated autoclave and maintained 180 °C for 48 h. Finally, the resulted product was separated by centrifuging and washed with deionized water and ethanol for several times. Then the obtained product was dried at 80 °C and calcinated at 450 °C for 4 h to obtain brownish yellow $CaBiO_3$ (CBO-IE) product.

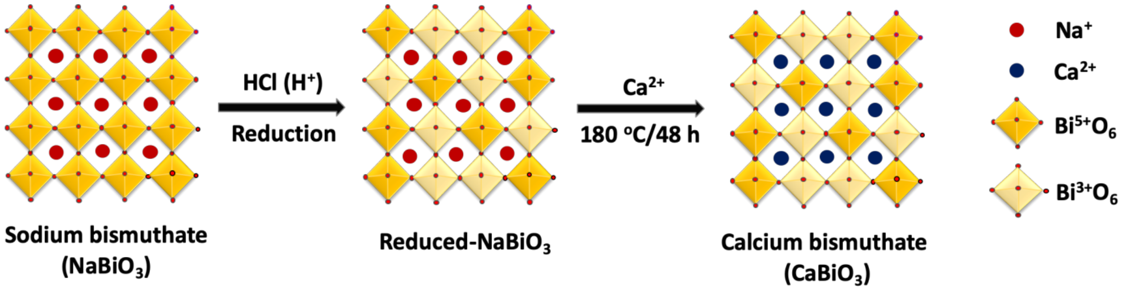

Scheme 4.2. Synthesis of $CaBiO_3$ by the ion-exchange method.

4.2.3 Characterizations

All the synthesized $CaBiO_3$ samples were characterized for their structural, optical, morphological, photo-physical and photocatalytic properties. The optical property was studied by UV-Visible spectroscopy (Cary 300 Bio UV-visible spectrophotometer). The crystal structure was analyzed using X-ray diffraction technique (Bruker SMART APEX II X-ray diffractometer equipped with a Cu Kα radiation source, λ = 1.5418 Å). The particle morphology and size of the samples were investigated using scanning electron microscope (JEOL 6360 instrument operated at 15 kV) and transmission electron microscope (JEOL JEM 1230 instrument operated at 120 kV). The nitrogen adsorption-desorption isotherms were studied using a Quantachrome Autosorb-1 MP analyzer. The surface chemical composition and chemical states of the catalysts were measured using X-ray photo-electron spectroscopy (Kratos Axis Ultra) equipped with a focused X-ray source (Al Kα, hν = 1486.6 eV). The photoelectrochemical properties were measured by a photo-electrochemical analyzer (Autolab PGSTAT204) using 100W Xenon arc lamp.

4.2.4 Photocatalytic experiment

Photocatalytic performance of the synthesized $CaBiO_3$ photocatalysts was examined on the degradation of antibiotic molecules such as ciprofloxacin and tetracycline under solar light illumination. In the typical experiment, 30 mg of photocatalyst was suspended in 100 mL of ciprofloxacin (10 ppm) and tetracycline (30 ppm) antibiotic solutions. Prior to the light irradiation, the photocatalyst-pollutant solution mixture was stirred at dark condition for about 15 min to attain the adsorption-desorption equilibrium. Then, the mixture was exposed under a 100W ABET Sunlite solar simulator, Xenon arc lamp with wavelength ranging from 250-1800 nm light irradiation and kept under a continuous stirring for the thorough mixing of the photocatalyst and pollutant. For every 15 min, a small amount of solution mixture was collected and investigated for its optical properties using a UV-Vis spectrometer to estimate the degradation kinetics.

4.3. Results and discussion

4.3.1 Optical properties

The UV-Vis absorption spectra of both CBO-GC and CBO-IE clearly revealed (as shown in **Figure 4.1(a)**) the visible light absorption characteristics of the $CaBiO_3$ system. This observed broad visible light absorption range of CBO-GC and CBO-IE systems could be attributed to the strong inter-site electron transition between Bi^{3+} 6s and Bi^{5+} 6s states in the

$CaBiO_3$ system[84, 111]. It should be noted that the CBO-GC is showing an extended visible light absorption range up to 550 nm as compared to that of the CBO-IE that shows absorption up to 450 nm, which could be due to their enhanced Bi^{3+}/Bi^{5+} charge disproportion in the CBO-GC system. These results indicate that the CBO shows the synthesis methods dependent optical properties. The glycine-bismuth complexation leads to the formation of Bi^{3+}/Bi^{5+} charge disproportion rich CBO, which could be due to the glycine molecules that stabilize the CBO system with oxygen vacancies through Bi^{3+}-O^{2-}-Bi^{5+} complexes. Therefore, the CBO-GC with rich Bi^{3+}/Bi^{5+} charge disproportion exhibited a strong and extended visible absorbance as there is a manifestation of electrons hopping or shuttling in the CBO-GC system[84, 111].

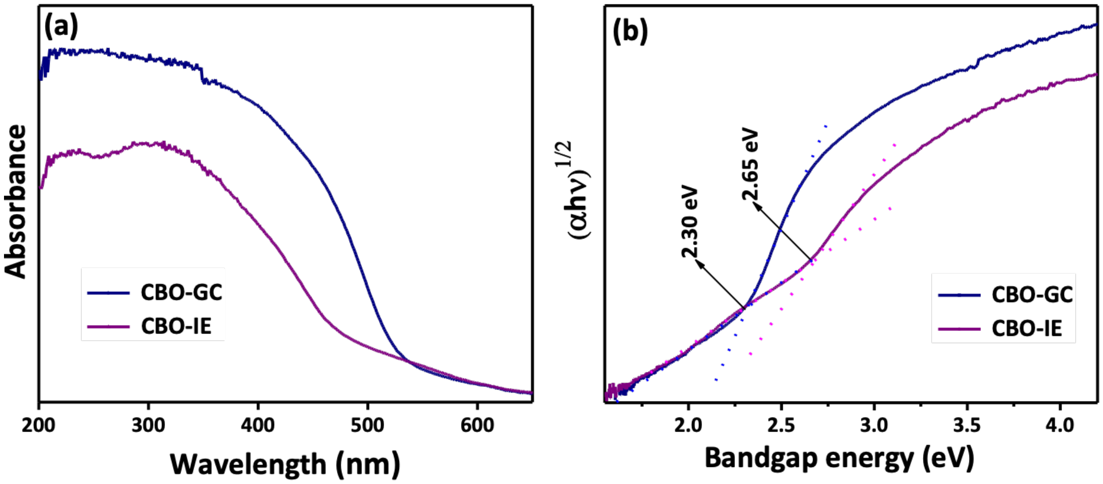

Figure 4.1. (a) UV-Vis spectra and (b) Tauc plot band gap energy of $CaBiO_3$ (CBO-GC and CBO-IE).

The band gap energy of the synthesized $CaBiO_3$ samples (CBO-GC and CBO-IE) is estimated from their optical absorption spectra through the Tauc plot as shown in **Figure 4.1(b)**. Generally, the typical narrow and indirect band gap energy of CBO is mainly attributed to the incorporation of small radii calcium cations (Ca^{2+}) into bismuthate (BiO_6) crystal structure in the $CaBiO_3$ system[111]. From the plot, the CBO-GC is showed the decreased band gap energy of 2.30 eV as compared to the CBO-IE, which is 2.65 eV. This could be because of the glycine-bismuth complexation that offers a well-organized calcium ion's incorporation into bismuthate lattices that shifted the valence band edge of bismuth

(Bi^{3+} 6s) into lower energy, therefore it led to the formation of reduced band gap energy in CBO-GC[84, 113]. On other hand, the ion exchange technique may offer the inadequate Ca^{2+} incorporation into BiO_6 crystal structures, which has insignificant impact on the valence band edge shifting in the CBO-IE system. Accordingly, the obtained band gap energy value of CBO-GC (2.30 eV) was found to be nearly equal to the theoretically predicted band gap energy of $CaBiO_3$ (2.09 eV)[111].

4.3.2 Crystalline and chemical composition analysis

The crystalline properties of $CaBiO_3$ (CBO-GC and CBO-IE) are investigated using X-ray diffraction (XRD) technique and the obtained results are shown in **Figure 4.2(a)**. Both the synthesized CBO-GC and CBO-IE systems are found to be crystalline in nature, but their XRD patterns are found to be slightly different from each other. This could be due to two possible reasons; (i) difference in the crystal structure and (ii) formation of impurities[84, 111].

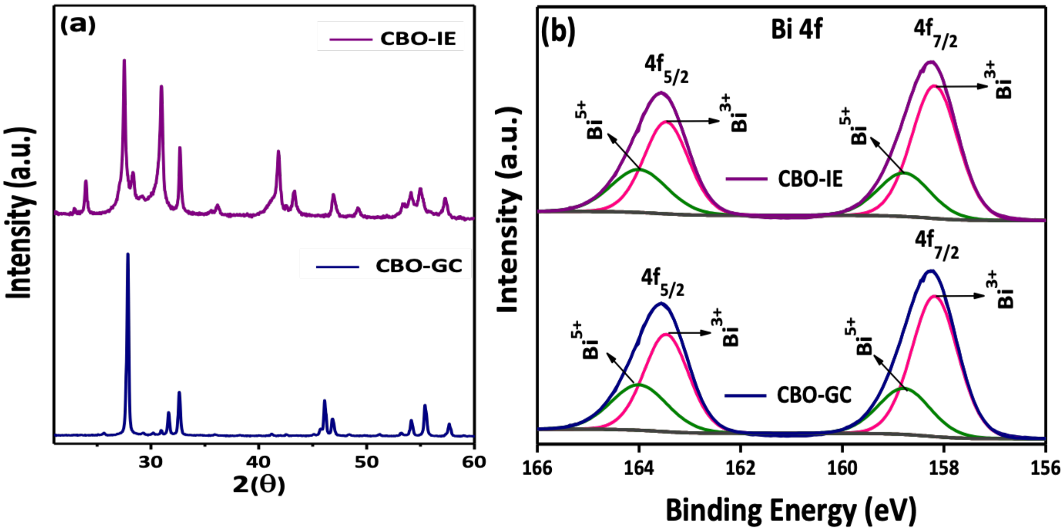

Figure 4.2. (a) X-ray diffraction spectra of $CaBiO_3$ (CBO-GC and CBO-IE) and (b) X-ray photoelectron narrow scan spectra of Bi4f (CBO-GC and CBO-IE).

It is realized that the $CaBiO_3$ phase could possibly take either the perovskite structure and crystallize in the monoclinic $P2_1/c$ space group or ilmenite structure and crystallize in the trigonal R-3 space group[111]. Accordingly, the differences in the obtained XRD patterns (mismatching of the peaks) of CBO-GC and CBO-IE may be due to their structural difference. However, we predict that CBO synthesized via GC method might have crystallized into perovskite structure, as it contains relatively low oxygen vacancy defects with relatively minimized Bi3+/5+ charge fluctuations as compare to the CBO synthesized via IE method[110]. Otherwise, it is also possible that the extra peaks appeared in the XRD patterns could be due to the formation of some impurities such as bismuth oxide (Bi_2O_3) and other possible impurity phases such as bismuth oxychloride (BiOCl), sodium bismuthate ($NaBiO_3$)[110, 114, 115]. However, the XPS spectra (as discussed in the following section) showed no peaks corresponding to Na or Cl or any other peaks corresponding to any other elements. In addition, to the best of our knowledge, there is no JCPDS data available for the $CaBiO_3$. Therefore, the observed difference in the XRD patterns could be ascribed to their structural difference rather than the formation of impurities.

The structural characteristics of CBO-GC could be attributed to its synthesis process, which facilitated the formation of a perfect BiO_6 octahedral arrangement along with a strong Bi-O hybridization and appropriate placement of Ca^{2+} ions in the $CaBiO_3$ system[84, 106]. On the other hand, in the ion-exchange process, the acid hydrolysis partially reduces the $Bi^{5+}O_6$ into $Bi^{3+}O_6$ and encourages the non-selective bismuth reduction. This non-selective reduction leads to the structural destruction in BiO_6 octahedral and poor Ca^{2+} incorporation into BiO_6 octahedral lattices, which eventually leads to the formation of different crystal structure and/or secondary impurities phases as mentioned above[109, 114].

The X-ray photoelectron spectra (XPS) of bismuth (Bi), as displayed in **Figure 4.2(b)**, show the existence of mixed oxidation sate of Bi (Bi^{3+}/Bi^{5+}) in the synthesized $CaBiO_3$ materials. The deconvoluted peaks of Bi can be assigned to Bi $4f_{5/2}$ and Bi $4f_{7/2}$ orbitals, where it has been found that the strong peaks of CBO-GC and CBO-IE at 163.4 and 158.1 eV can be assigned to +3 oxidation state of bismuth, whereas the weak peaks of CBO-GC and CBO-IE at 164.0 and 158.7 eV can be assigned to +5 oxidation state of bismuth[109, 110, 116]. Accordingly, the charge distributions of Bi^{3+} and Bi^{5+} oxidation states of Bi in CBO-GC and CBO-IE samples were estimated from their respective Bi XPS spectra. The estimation showed that in the sample CBO-GC, the percentage of Bi^{3+} and Bi^{5+} is 68.67 and 31.33% respectively. Similarly, in the sample CBO-IE, the percentage of Bi^{3+} and Bi^{5+} is 80.79 and 19.21% respectively. It should be noted that the $CaBiO_3$ system typically has two types of distorted BiO_6 octahedral on its unit cell, which are $Bi^{3+}O_6$ and $Bi^{5+}O_6$. The octahedral BiO_6 are connected to each other and the Ca^{2+} ions are located between octahedral BiO_6. Therefore, the developed CBO material contains two kinds of octahedral distorted and ordered cations in their perovskite structure[84, 111]. These two different octahedral distorted units $Bi^{3+}O_6$ and $Bi^{5+}O_6$ establish the dipole-induced internal electrical field, where the electron hopping between Bi^{3+} and Bi^{5+} can offer the enhanced ferroelectric properties to $CaBiO_3$ system[99].

The XPS survey spectra of $CaBiO_3$ (CBO-GC and CBO-IE) are given in **Figure S4.1(a)** (supporting information), where it clearly indicates that all the synthesized materials contain the respective elements such as Ca, Bi and O with its native oxidation states and without any impurities. The narrow scan XPS spectra of Ca, O and C elements are given in **Figure S4.1(b-d)** (supporting information). The XPS spectra of calcium (Ca) (in **Figure S4.1(b)** supporting information) show the peaks at 350.0 and 346.4 eV corresponding to Ca $2p_{1/2}$ and Ca $2p_{3/2}$ orbital of Ca^{2+} ions. The O1s XPS spectra of $CaBiO_3$ (CBO-GC and CBO-IE) could be deconvoluted into three peaks, as shown in **Figure S4.1(c)**, such as lattice oxygen (Bi-O), oxygen vacancy ($O_{vacancy}$) and adsorbed oxygen (O-H). The O 1s spectrum of CBO-GC clearly demonstrated that the CBO-GC contains only the lattice oxygen (Bi-O) and oxygen vacancies ($O_{vacancy}$), while the CBO-IE contains the adsorbed oxygen (O-H) in addition to the lattice oxygen (Bi-O) and oxygen vacancies ($O_{vacancy}$)[110]. Furthermore, the pronounced asymmetric peak of O 1s spectrum of CBO-IE indicates that the system relatively contains more oxygen vacancy defects (77.6%) as compared to CBO-GC (38.8%). Accordingly, there has been a shift towards higher binding energy observed in the Bi XPS spectrum of CBO-IE as compared to CBO-GC, which might have occurred due to the inadequate Bi-O interactions. This can be corroborated with the estimated concentrations of Bi-O, where it was found to be 61.2 and 15.9% in CBO-GC and CBO-IE respectively. The oxygen vacancy defects essentially affect the bismuthate (BiO_6) lattice structures in $CaBiO_3$ systems and thereby it leads to the formation of highly distorted structure in CBO-IE[109, 110]. This could be the reason for the observed structural discrepancy in the CBO-GC and CBO-IE, which can be corroborated through the observed differences in their XRD patterns. Despite the rich-oxygen vacancies in CBO-IE system, the presence of adsorbed oxygen (O-H ~6.8%) species (**Figure S4.1(c)**) in the sample likely stabilize the system by screening the influence of vacancy defects and enhance the surface-adsorption and reactivity of the sample towards its photocatalytic reactions. **Figure S4.1(d)** displays the deconvoluted C 1s XPS spectra of CBO-IE and CBO-GC, where it demonstrates the characteristic existence of C=C, C-C, C-O and C=O species in the samples. We would like to highlight that the CBO synthesized by sol-gel method did not show the existence of dual oxidation states of Bi, rather it possesses its stable mono-oxidation state, which is +3 as confirmed through its XPS spectrum as shown in **Figure S4.2**.

4.3.3 Morphological and surface area analysis

The morphological analysis of the synthesized $CaBiO_3$ samples (CBO-GC and CBO-IE) were performed using scanning electron microscopy (SEM) and transmission electron microscopy (TEM) techniques and the obtained images are displayed in **Figure 4.3(a-d)**. The morphology of CBO-GC is found to be nano-flakes that aggregated into flower like structure with the average length of flakes around 450 nm as shown in **Figure 4.3(a-b)**. Similarly, the morphology of CBO-IE is found to be nanosheets-like structure that aggregated into micro-structured particle with an average length of the nanosheets around 600 nm as shown **Figure 4.3(c-d)**. It is observed from these results that the ion-exchange method leads to the formation of aggregated nanosheets, while the glycine-bismuth complex favors the formation of dispersed nano-flakes morphology with thin layered structure of $CaBiO_3$. This could be because of the glycine that acts as chelating agent as well as shape controlling agent towards the formation of thin layered nano-flakes structures of $CaBiO_3$[112].

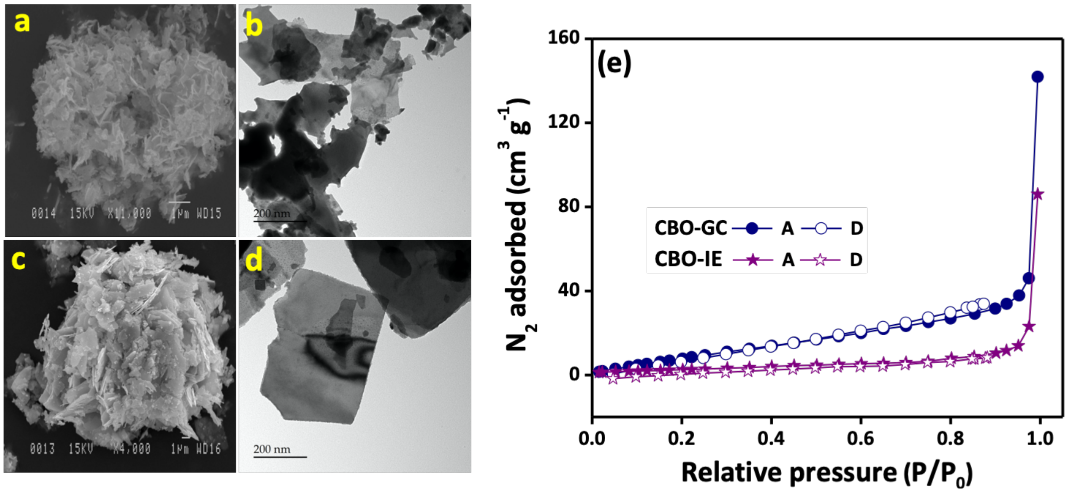

Figure 4.3. SEM and TEM images of $CaBiO_3$ (a)-(b) CBO-GC; (c)-(d) CBO-IE and (e) Nitrogen adsorption-desorption isotherm of CBO-GC and CBO-IE.

The nitrogen (N_2) adsorption-desorption isotherm of CBO-GC and CBO-IE is shown in **Figure 4.3(e)**. The obtained results revealed that the CBO-GC demonstrates an enhanced surface adsorption-desorption efficiency as compared to CBO-IE. In addition to the less aggregation, the nano-flakes of CBO-GC also contain nanosized porous structure on the surface, which led to the enhanced N_2 adsorption[112], while no such pores are found on the surface of CBO-IE nanosheets. Accordingly, the surface area of CBO-GC is found to be around 46.6 m^2/g, while it is only 14.2 m^2/g for CBO-IE. Therefore, the high surface area of CBO-GC could offer more active sites on its surface and provide better active sites along with an improved charge transfer pathway in CBO-GC towards the enhanced photocatalytic reactions[99].

4.3.4 Photoelectrochemical and photocatalytic study

The photoelectrochemical (PEC) studies revealed the characteristic photo-induced charge generation, separation and transfer processes in the CBO-GC and CBO-IE systems. The PEC measurements such as chronoamperometry and impedance characteristics have been investigated using sodium sulfate as electrolyte under the solar light irradiation and the obtained results are shown in **Figure 4.4(a-b)**. The chrono-amperometry study of the samples demonstrated the characteristics of the photoinduced charge generation and separation in the synthesized $CaBiO_3$ systems as shown in **Figure 4.4(a)**. The photocurrent density of the samples can be ascribed to the generation of photo-induced charge carriers and their effective separation, where the higher and lower photocurrent densities during the ON-OFF cycles is associated with the electron-hole charge separation process in the system under light and dark conditions[117]. It should be noted that the photoconductivity in $CaBiO_3$ is fundamentally originated due to the spatially extended 6s orbital of Bi^{3+} and Bi^{5+}cations[84, 111, 118]. Accordingly, it can be noted in **Figure 4.4(a)** that the CBO-GC shows relatively a higher photocurrent density, which implies the manifestation of higher electron-hole generation and charge separation in the system as compared to the CBO-IE system. The obtained graph showed that the photocurrent density of CBO-GC is reached up to 162.8 $\mu A\ cm^{-2}$ at 0.6 V. This could be due to the optimal band edge position, band gap energy, optimal Bi 6s charge disproportion and perfect BiO_6 octahedral hybridization in CBO-GC, which facilitated an enhanced charge generation and separation of photo-induced electrons-holes in the system[84, 111, 118] as compared to the CBO-IE. The charge disproportion in the system is correlated with their oxygen vacancy defects, where the increased oxygen vacancies act as recombination centers for the excited electrons, while the optimal oxygen defect act as trap for the excited electrons that increase the life of the separated charge carriers by preventing their recombination.

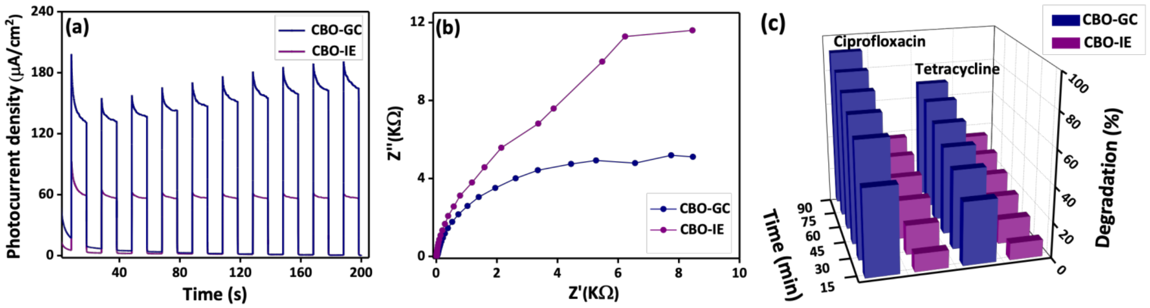

Figure 4.4. (a) Chronoamperometric, (b) Impedance response-Nyquist plots and (c) Photocatalytic degradation of antibiotic ciprofloxacin and tetracycline by the CBO-GC and CBO-IE under solar light irradiation.

The impedance characteristics as revealed by the Nyquist plot demonstrate the recombination resistance in the synthesized CBO-GC and CBO-IE samples as shown in **Figure 4.4(b)**. The Nyquist plot essentially reflects the charge transfer rate on the electrode surface, which can be determined by arc radius of the curve[117]. Accordingly, the obtained smaller arc radius of CBO-GC represents the effective electron-hole pair separation and lower resistivity in the system. As described, the glycine-bismuth complexation leads to the formation of ideal BiO_6 octahedral structures along with an effective Ca^{2+} incorporation into the lattices of BiO_6 framework. This eventually tends to the shifting of the valence band of CBO-GC towards an optimal energy level along with the localization of Bi 6s bands near to its Fermi level and thereby it demonstrated an enhanced charge transfer and greatly reduced electron-hole recombination possibilities. Then, the CBO-IE showed a higher arc radius that revealed higher resistivity and greater charge recombination, which can be attributed to their synthesis (ion-exchange) process mediated structural distortion in the BiO_6 octahedral structure and the inefficient Ca^{2+} incorporation into BiO_6 frameworks that led to the shifting of the valence band edge potential to more positive and limited the charge transfer kinetics in the system in CBO-IE. Therefore, the optimal charge disproportion and ideal structural arrangements in CBO-GC offered a better light-harvesting ability and thereby the improved charge transfer and reduced electron-hole recombination in $CaBiO_3$ system[84, 111, 118].

The photocatalytic performance of the synthesized CBO-GC and CBO-IE samples were examined on the degradation of antibiotics such as ciprofloxacin (CIP) and tetracycline (TEC) under solar light irradiation[119, 120] and the obtained results are given in **Figure 4.4(c)**. The time dependent absorbance spectra of ciprofloxacin and tetracycline degradation over CBO-GC and CBO-IE samples are given in **Figure S4.3(a-d)** in the supporting information. As showed in **Figure 4.4(c)**, the CBO-GC showed a degradation efficiency of 90.5 and 68.6% on CIP and TEC respectively at the end of 90 min, while it was found to be 36.5 and 33.3% respectively for CBO-IE. It is known that the photocatalytic efficiency of a material is governed by the factors such as the appropriate band edge position, band gap energy, surface reactivity, enhanced charge separation and recombination resistance, etc. Especially, considering the valence band (VB) and conduction band (CB) positions, the more negative potential of CB facilitates the reduction reactions and favors the production of super oxide anionic radicals ($O_2^{\bullet-}$), while the more positive potential favors the oxidation reaction through the generation of $OH^{\bullet}$ radicals[121-123]. The XPS valence band spectra (**Figure 4.5(a-b)**) showed that the VB potential of CBO-IE has been shifted towards more positive (+2.45 eV) as compared to the CBO-GC (+1.90 eV) and thereby the calculated CB potential of CBO-GC and CBO-IE was found to be -0.40 and -0.20 eV respectively as shown in **Figure 4.5(c)**. Such positioning of the VB and CB essentially favored the generation of highly reactive radicals towards the effective degradation of the pollutants[121]. Accordingly, as illustrated in **Figure 4.5(c)**, the VB potential of CBO-GC is +1.90 eV of may not be enough to generate hydroxyl radical ($OH^{\bullet}/OH^{-}$ = 1.99 eV), but on the other hand, the CB potential of CBO-GC is -0.4 eV, which could be enough to generate super oxide radical ($O_2/O_2^{\bullet-}$ = -0.33 eV). Therefore, it is possible that the holes and superoxide radical's active species can be effectively generated over CBO-GC as compared to CBO-IE[38]. Thereby, it can be proposed that the observed enhanced photocatalytic efficiency of CBO-GC could be possibly due to the enhanced formation of super oxide anionic radicals and direct holes (h^+) oxidation of the pollutant molecules[124, 125]. The holes at the less positive VB potential of CBO-GC possess the required energy to oxidize the pollutant molecules. In the case of CBO-IE, the photocatalytic reaction might have occurred predominantly by the OH$^{\bullet}$ radicals rather than super oxide anion radical's and holes[126]. Because of the VB potential of CBO-IE is 2.40 eV, which may be enough to generate hydroxyl radical (OH$^{\bullet}$/OH^{-} = 1.99 eV) and CB potential of CBO-IE is -0.20 eV may not be enough to produce super oxide radical ($O_2/O_2^{\bullet -}$ = -0.33 eV). Therefore, the less positive potential of VB and more negative potential of CB of CBO-GC together led to the enhanced photocatalytic efficiencies as compared to the CBO-IE.

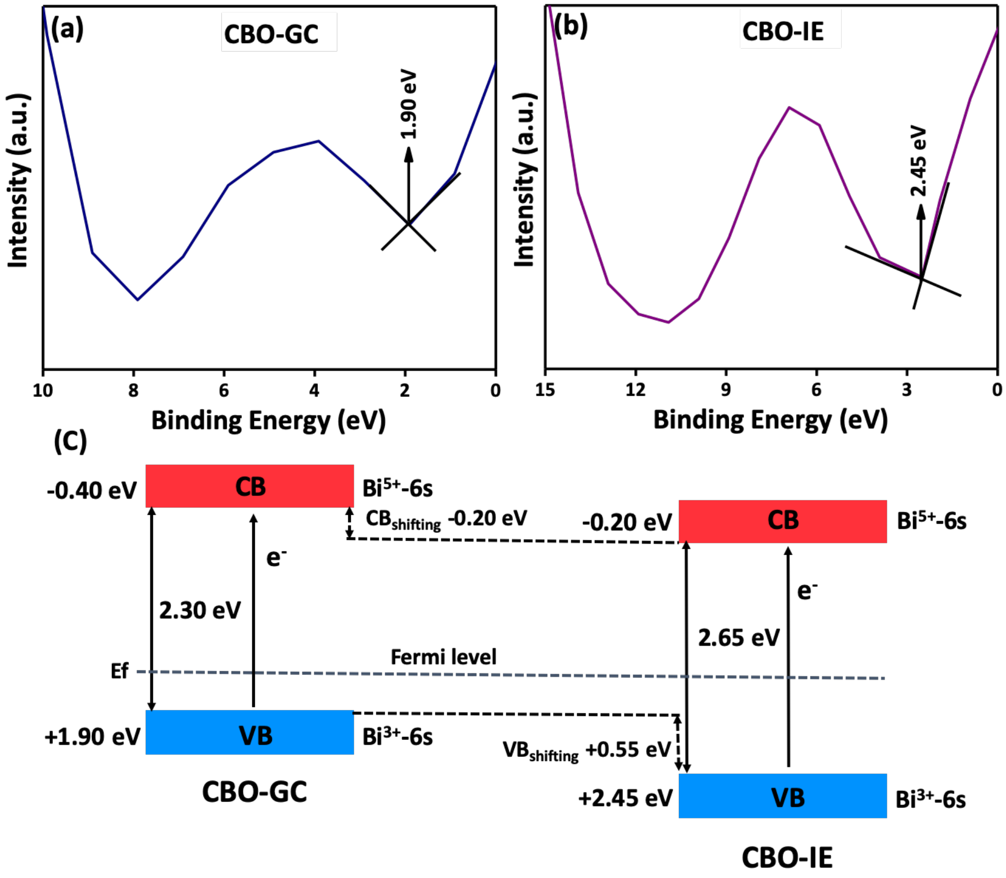

Figure 4.5. XPS valence band spectrum of (a) CBO-GC, (b) CBO-IE and (c) Schematic illustration of the relative alignment of band edge positions in CBO-GC and CBO-IE systems.

Towards estimating any surface "adsorption" nature of CBO-GC and CBO-IE samples, the degradation experiments were also conducted without solar light by following the same experimental conditions and the obtained results are given in **Figure S4.4(a-f)** in the supporting information. The obtained results showed that both the CBO-GC and CBO-IE systems possess relatively less adsorption characteristics, where it was found to be around 26.6 and 20.6% of CIP and TEC respectively on CBO-GC sample and 10.7 and 6.4% of CIP and TEC respectively on CBO-IE sample (both at the end of 90 min).The observed adsorption properties of the samples could be attributed to their surface characteristics such as enhanced porous nature and surface adsorbed hydroxyl ions over the CBO-GC and CBO-IE samples respectively[28, 127].

Similarly, to examine the photolysis characteristics of CIP and TEC molecules, the degradation experiment was conducted under solar light irradiation without adding the photocatalysts and data are given in **Figure S4.5(a-b)** in the supporting information. The obtained results showed that there is only a negligible amount photolysis of CIP and TEC molecules occurred under the solar light irradiation. Further, towards examining the photo-stability and reusability of the synthesized photocatalysts, the photocatalytic degradation experiments were repeated for 5 runs using the used photocatalysts, the result given in **Figure S4.6(a-b)**. Both the systems CBO-GC and CBO-IE demonstrated good stability, however, CBO-GC showed relatively enhanced stability as compared to CBO-IE, which could be mainly attributed to their stabilized structural and compositional properties[57, 128]. Furthermore, as compared to other typical $MBiO_3$ based photocatalysts, this present $CaBiO_3$ photocatalyst relatively shows enhanced photocatalytic activity and stability. A comparative analysis between the developed $CaBiO_3$ and other $MBiO_3$ based photocatalysts towards their photocatalytic efficiency is given in **Table S4.1** in the supporting information.

4.4. Conclusion

In summary, we have developed new ferroelectric perovskite material calcium bismuthate ($CaBiO_3$) with distinct Bi^{3+} and Bi^{5+} multi-charge disproportion via glycine-complexation and ion-exchange methods. The founded efficient Bi^{3+}/Bi^{5+} charge disproportion and well-organized BiO_6 octahedral crystal arrangement offered an efficient visible photo-absorbance and higher photo-generated charge carrier generation and separation to CBO system. Then, the effective Ca^{2+} incorporation into bismuthate **(**BiO_6**)** crystal lattices was potentially altered CBO band gap and band structure. The established band structure and band energy potentials are more suitable for photocatalytic redox reactions. Subsequently, the developed CBO materials are presented nanostructure with higher surface area which provide enhanced surface properties to catalytic reaction. Furthermore, the developed $CaBiO_3$ materials is potentially explored on degradation of antibiotic contaminants under solar light. To best of our knowledge this is the first reports on development of $CaBiO_3$ and its potential application photocatalytic degradation of antibiotics.

Acknowledgements

This work was supported by the Natural Science and Engineering Research Council of Canada (NSERC) through the Strategic Project (SP), and Discovery Grants. The authors would like to thank Exp Inc. and SiliCycle Inc. for their support.

4.5. Supporting information

4.5.1 X-ray photoelectron spectra (XPS)

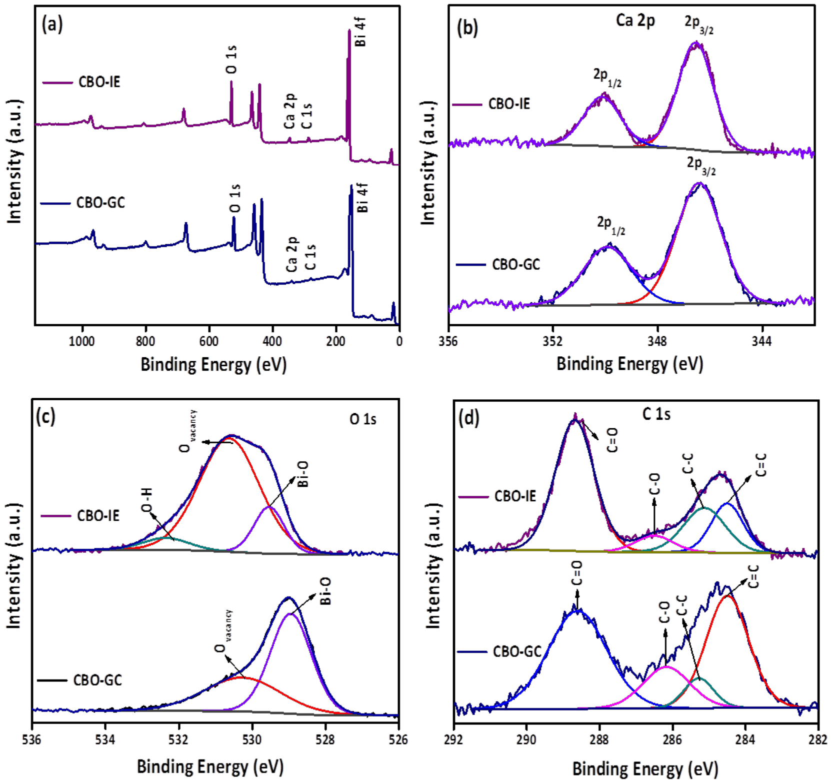

Figure S4.1. XPS of (a) survey spectra (b) Ca 2p (c) O 1s and (d) C 1s spectra of CBO-GC and CBO-IE.

4.5.2. Synthesis and chemical oxidation state of CBO-SG

Calcium bismuthate (CBO-SG) was also prepared via the conventional sol-gel method. In this typical process, 0.1 M of $Ca(NO_3)_2 \cdot 4H_2O$ and 0.1 M of $Bi(NO_3)_3 \cdot 5H_2O$ solution were mixed together and stirred for 1 h. After that 0.1 M of tartaric acid solution was added dropwise and allowed stirring for 1 h. Then, this aged sol was heated at 80 °C overnight until all the water content was evaporated completely and obtained a white powder. Then this white powder was calcined at 650 °C for 3 h to obtain the crystalline $CaBiO_3$ phase (CBO-SG), which appeared pale yellow in color.

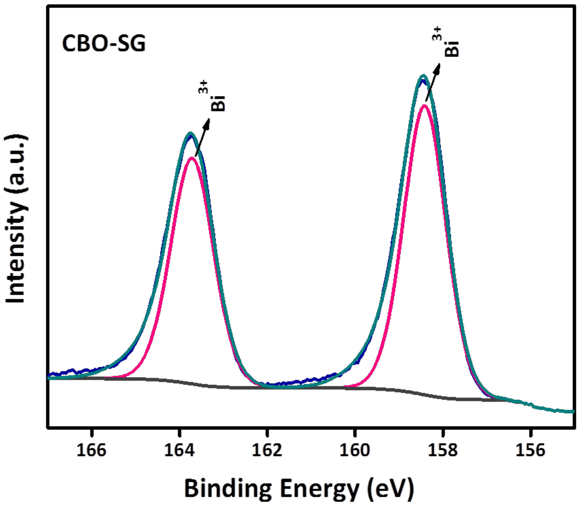

Figure S4.2. Bi 4f narrow scan X-ray photoelectron spectrum of CBO-SG.

4.5.3. Photocatalytic degradation of ciprofloxacin and tetracycline

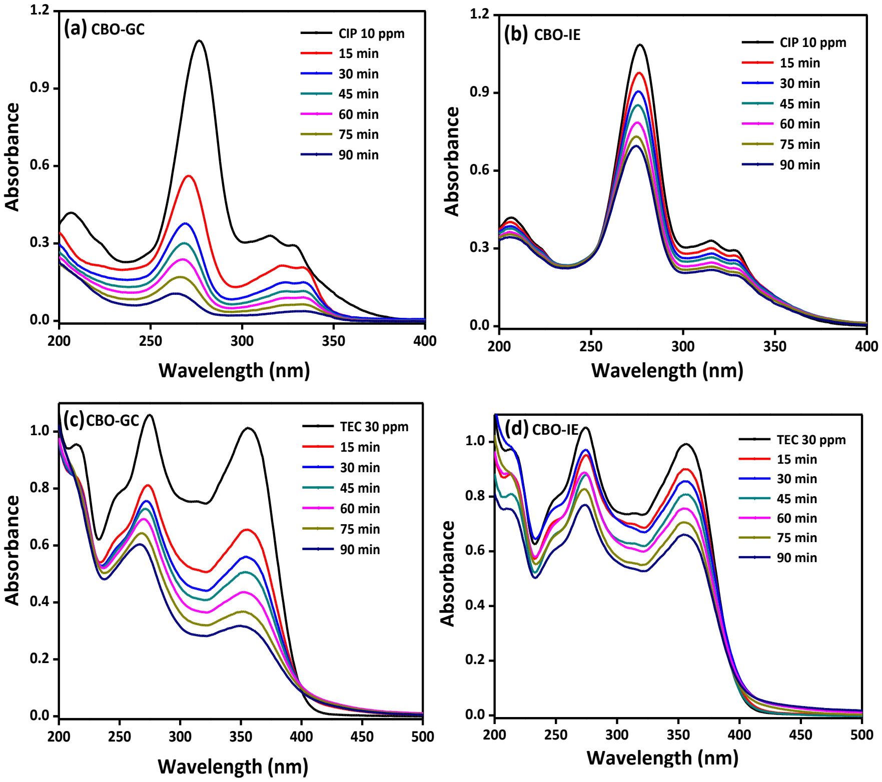

Figure S4.3. UV-vis absorbance spectra of degradation of (a)-(b) ciprofloxacin and (c)-(d) tetracycline using CBO-GC and CBO-IE under solar light, respectively.

4.5.4. Adsorption of ciprofloxacin and tetracycline

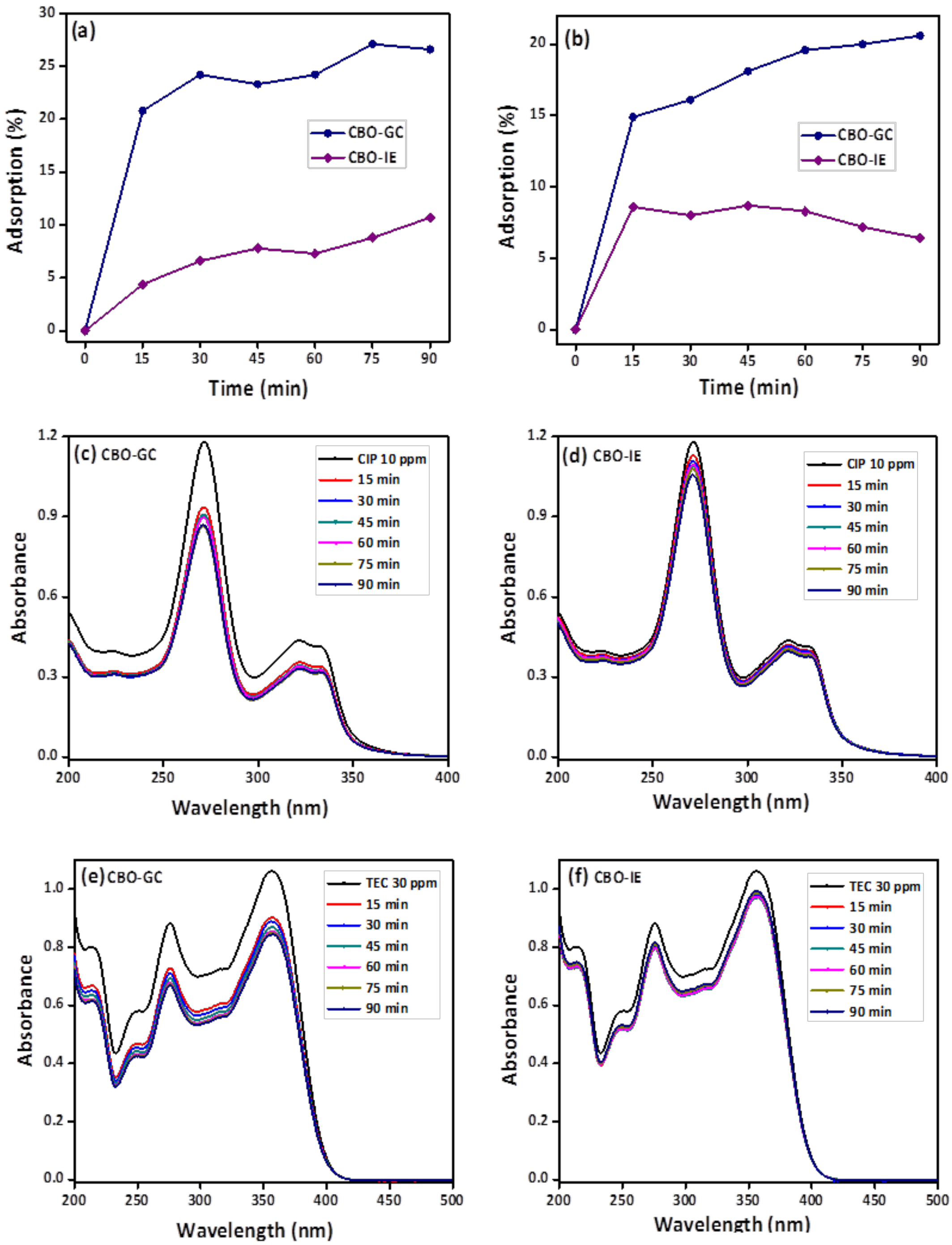

Figure S4.4. Surface adsorption of (a) ciprofloxacin, (b) tetracycline onto the CBO-GC and CBO-IE photocatalysts under dark condition; UV-vis absorbance spectra towards understanding the adsorption of (c-d) ciprofloxacin and (e-f) tetracycline using CBO-GC and CBO- IE under dark condition, respectively.

4.5.5. Photolysis of ciprofloxacin and tetracycline

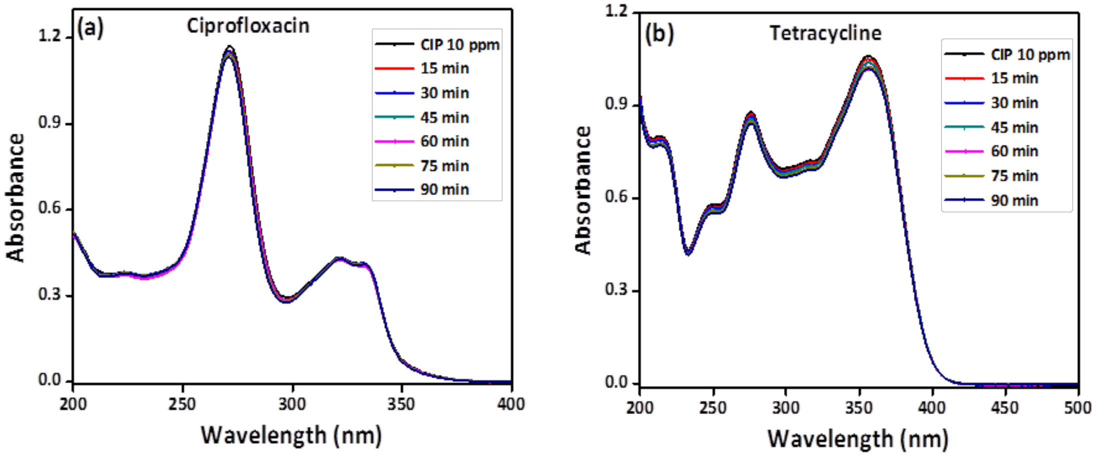

Figure S4.5. Photolysis of (a) ciprofloxacin and (b) tetracycline under solar light without photocatalyst.

4.5.6. Reusability of photocatalyst

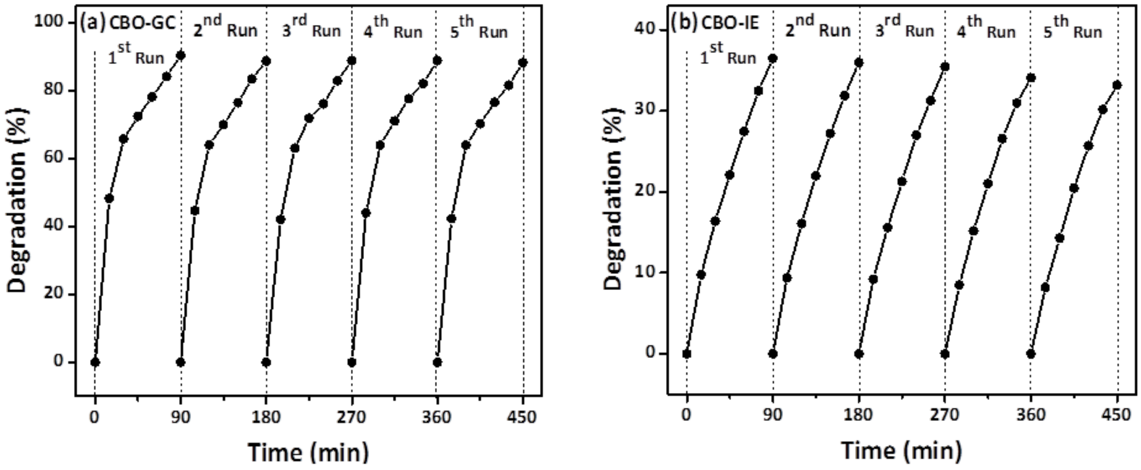

Figure S4.6. Photocatalytic reusability test of (a) CBO-GC and (b) CBO-IE on the degradation of ciprofloxacin under solar light irradiation.

4.5.7. Photocatalytic performance of $CaBiO_3$ compared with related materials

Photocatalyst	Oxidation states	Light source	Pollutants	Degradation efficiency (%)	Time (min)	References
$CaBiO_{33}$	Bi^{3+} & Bi^{5+}	Solar light	Ciprofloxacin Tetracycline	90.5 68.6	90	Present work
$BaBiO_3$	Bi^{3+} & Bi^{5+}	Visible light	Acetaldehyde Methylene blue	~100 100	195 120	[84]
$BaBiO_3$	Bi^{3+} & Bi^{5+}	Visible light	Rhodamine B	83	240	[129]
Bi^{3+} self-doped $NaBiO_3$	Bi^{3+} & Bi^{5+}	Visible light	Rhodamine B Bisphenol A	~100 100	40	[110]
Bi^{3+} self-doped $NaBiO_3$	Bi^{3+} & Bi^{5+}	Visible light	Carbamazepine	99.8	60	[107]
$NaBiO_3$	Bi^{5+}	Visible light	Rhodamine B	~100	30	[130]
$KBiO_3$	Bi^{5+}	Visible light	Rhodamine B Crystal violet	~100 85	50 90	[104]
$LiBiO_3$	Bi^{5+}	Solar light	Methylene blue Rhodamine B	~95 ~30	120	[131]

Table S4.1. Comparative table showing the photocatalytic efficiency of $CaBiO_3$ and other $MBiO_3$ structures reported in the literature.

Chapter 5 : Integration of aminosilicate functionalized - fullerene (C_{60}) QDs on bismuth vanadate ($BiVO_4$) nanolayers for the photocatalytic degradation of pharmaceutical pollutant

K. Rokesh, M. Sakar, Trong-On Do*

Department of Chemical Engineering, Laval University, Québec (Québec), G1V 0A6, Canada

*E-mail: trong-on.do@gch.ulaval.ca

This chapter is submitted in Catalysis Today 2021, 10.1016/j.cattod.2021.10.006

Résumé

Un nanomatériau composite constitué des points quantiques de fullerène (C_{60} QDs), fonctionnalisés par aminosilicate (APS), et de vanadate de bismuth ($BiVO_4$-APS-C_{60}) a été développé via un processus hydrothermal facile en une seule étape. L'analyse structurelle par XRD a révélé que les QDs intégrés n'ont pas affecté la structure cristalline de $BiVO_4$, tandis que l'analyse par XPS a montré que ces QDs ont été intégrés en tant que Bi-V-O-Si-C. Les études optiques ont indiqué que les C_{60} et APS-C_{60} QDs ont légèrement affecté les propriétés d'absorption optique du composite. D'autre part, la dispersion des QDs fonctionnalisés par aminosilicate a considérablement réduit l'agrégation dans les couches et a donné des couches de $BiVO_4$ de quelques nanomètres d'épaisseur en raison de leur occupation intercouche comme il a été illustré par les images TEM à haute résolution. Les études de photoluminescence, de photocourant et d'impédance électrochimique ont montré que l'intégration des APS-C_{60} QDs a considérablement amélioré les propriétés photocatalytiques du composite en améliorant efficacement la résistance aux recombinaisons des charges, la séparation des charges et le processus de transfert entre les constituants du nanocomposite. Par conséquent, le composite $BiVO_4$-APS-C_{60} a montré une efficacité photocatalytique améliorée vis-à-vis la dégradation des molécules de ciprofloxacine (CIP) sous irradiation solaire par rapport à celle de $BiVO_4$ et $BiVO_4$-C_{60}.

Abstract

A composite system consisting of aminosilicate (APS) functionalized-fullerene quantum dots (C_{60} QDs) and bismuth vanadate ($BiVO_4$-APS-C_{60}) has been developed via a facile one-step hydrothermal process. The structural analysis by XRD revealed that the integrated QDs have not affected the crystal structure of the host $BiVO_4$, while the XPS studies showed that these QDs have been integrated via the Bi-V-O-Si-C network. The optical studies indicated that both the C_{60} and APS-C_{60} QDs have hardly influenced the optical absorption properties of the composite system. On the other hand, the dispersion of aminosilicate functionalized-QDs considerably reduced the aggregation in the layers and yielded a few nanometer thick $BiVO_4$ layers due to their inter-layer occupancy as seen from their high-resolution TEM images. The photoluminescence, photocurrent and electrochemical impedance studies showed that the integration of APS-C_{60} QDs greatly improved the photoactive properties of the composite by effectively enhancing the charge recombination resistance, charge separation and transfer process between the integrated materials and surroundings. As a result, $BiVO_4$-APS-C_{60} composites showed the enhanced photocatalytic efficiency towards degradation of ciprofloxacin (CIP) molecules under solar light irradiation as compared to that of bare-$BiVO_4$ and $BiVO_4$-C_{60}.

5.1. Introduction

In recent years, the detection of antibiotics in the aquatic ecosystem has received much attention due to their specific environmental risks and potential impacts on the aquatic animals as well as human health[4, 5]. The improper disposal and overuse of antibiotic drugs lead to serious issues worldwide. Antibiotics and their metabolites are often found in global aquatic environments in different concentrations; however, it does not show any direct effects and toxicity to humans[2, 3]. However, the antibiotic residues facilitate the emergence of antibiotic-resistance microorganisms, which ultimately reduce the potential healing towards humans, animals and other ecosystems from the induced toxic effects[7]. These antibiotic-resistant bacteria no longer respond to the antibiotic treatment, which poses a serious threat and it causes serious public concerns as well[132]. Therefore, it is an urgent need to develop a potential technique for the effective removal of antibiotic residues from the water-bodies[9, 10]. Accordingly, many techniques such as adsorption, filtration, biological, electrocatalytic and photocatalytic treatments have been developed for such applications[51, 133-136]. While most of the conventional treatments are relatively less effective for the removal of antibiotic contaminants, the semiconductor-based photocatalytic technique is considered as an efficient technique for the removal of antibiotics from effluent water[12, 15, 137]. Semiconductor photocatalysis is considered as a green and sustainable technology thanks to its potential utilization of solar energy and high efficiency towards a wide range of pollutant removal from water environments[11, 138, 139]. Over the past few years, bismuth-based semiconductors have attracted significant interest in photocatalysis due to their complex structure and unique physical properties, which offer interesting visible light absorption with narrow band gap energy of around 2.4 eV and high stability[140]. Among the Bi-based materials, $BiVO_4$ has been explored for photocatalytic removal of organic contaminants, water splitting, carbon dioxide reduction and organic conversion[88, 89, 141, 142]. However, studies showed that the photocatalytic efficiency of the bare $BiVO_4$ can be further improved by reducing its electron-hole charge recombination and by enhancing its surface properties[143, 144]. Hence, great efforts have been made to overcome such limitations, where the ultrathin $BiVO_4$ showed superior photocatalytic performance as its ultrathin nanostructures offer a large number of surface-active sites for the effective photocatalytic process[82, 141]. Nevertheless, this ultrathin $BiVO_4$ photocatalyst still had an issue of slow charge transfer and fast charge recombination[145]. On the other hand, carbon nanostructures (C_{60}) have been widely used as supporting materials for the fabrication of semiconductor-based composite photocatalytic system due to their excellent electron receiving and transporting properties[146-148]. Therefore, combining $BiVO_4$ and C_{60} could make an ideal system, which could increase the photocatalytic efficiency via the synergetic effects between C_{60} and $BiVO_4$ nanostructures. Further, it is found that the silicate functionalization of C_{60} QDs can improve the overall photoconductivity and stability of the system through intact integration of C_{60} and $BiVO_4$[149, 150]. In this context, herein we have developed the aminosilicate (APS)-functionalized fullerene (C_{60}) integrated bismuth vanadate ($BiVO_4$-APS-C_{60}) nanocomposite via one-step hydrothermal technique. The incorporation of fullerenes can effectively improve the transfer of photo-generated electrons and slow down the charge recombining rates and thereby it can enhance the overall photoredox property of the system and accordingly the as-developed $BiVO_4$-APS-C_{60} composite was found to show excellent photocatalytic activity towards degradation of ciprofloxacin molecules under solar light.

5.2. Materials and characterizations

5.2.1 Chemicals

The precursors such as bismuth chloride ($BiCl_3$), sodium orthovanadate (Na_3VO_4), cetrimonium bromide (CTAB, $C_{19}H_{42}BrN$), Fullerene (C_{60}), 3-aminopropyltriethoxysilane (APTES/APS, $C_9H_{23}NO_3Si$), ethylene glycol ($C_2H_6O_2$) and toluene (C_7H_8) were procured from Sigma Aldrich and used without any further purification.

5.2.2 Materials preparation

5.2.2.1 Preparation of $BiVO_4$ nanolayers: In a typical procedure, 2.21 g of $BiCl_3$ and 1.05 g of CTAB were added to 60 mL of ethylene glycol. After vigorous stirring for 40 min, 2.80 g of Na_3VO_4 was added into the reaction mixture and then transferred into a 140 mL Teflon-lined autoclave, sealed and heated at 160 °C for 3 h. Then, the autoclave was allowed to cool down naturally to room temperature, and the final product was collected by centrifuging. The obtained mixture was washed several times with ethanol and water and then dried at 80 °C overnight (**Scheme 5.1**).

5.2.2.2 Preparation of $BiVO_4$-C_{60} composite: Similar to the above procedure, 2.21 g of $BiCl_3$ and 1.05 g of CTAB were added to 60 mL of ethylene glycol. After vigorous stirring for 40 min, 2.80 g of Na_3VO_4 was added into the reaction mixture. At the same time, 1.0 mg of C_{60} was dissolved in a toluene solution (1.0 g/L) under ultrasonication for 30 min with the formation of a pink colour solution. The clear C_{60} solution was then added into the above reaction mixture and subsequently transferred into a 140 mL Teflon-lined autoclave, sealed and heated at 160 °C for 3 h. Then the autoclave was allowed to cool down naturally to room temperature, and the final product was collected by centrifuging. This obtained mixture was washed several times with ethanol and water and then dried at 80 °C overnight (**Scheme 5.1**).

5.2.2.3 Preparation of $BiVO_4$-APS-C_{60} composite: In this procedure, 2.21 g of $BiCl_3$ and 1.05 g of CTAB were added to 60 mL of ethylene glycol. After vigorous stirring for 40 min, 2.80 g of Na_3VO_4 was added into the reaction mixture. Meanwhile, 1 mg of C_{60} was added into 1 mL toluene solution with the addition of 0.1 mL of 3-aminopropyltriethoxysilane (APTES/APS) under ultrasonication process for 30 min. Then, the clear aminosilicate-functionalized C_{60} (APS-C_{60}) solution was added dropwise into the above reaction mixture, followed by, the mixture was transferred into a 140 mL Teflon-lined autoclave, sealed and heated at 160 °C for 3 h. Then the autoclave was allowed to cool down naturally to room temperature and the final product was collected by centrifuging. This obtained mixture was washed several times with ethanol and then dried at 80 °C overnight (**Scheme 5.1**).

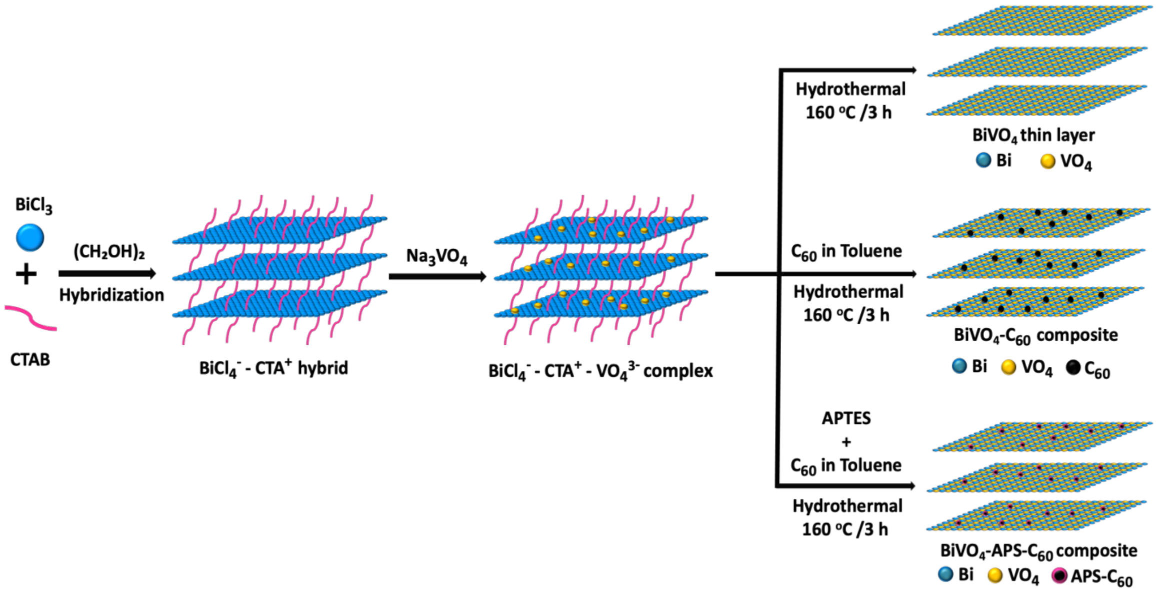

Scheme 5.1. Synthesis and formation mechanism of $BiVO_4$, $BiVO_4$-C_{60} and $BiVO_4$-APS-C_{60} composite via one-pot hydrothermal technique.

5.2.3 Material characterizations

The optical absorbance was measured using UV-visible diffuse reflectance spectroscopy (UV-DRS, Cary 300 Bio UV-visible spectrophotometer) and emission spectra were measured using photoluminescence spectrometer (PL, HORIBA PTI Quanta Master 500 spectrofluorometer). The crystal structures of the materials were determined using X-ray diffraction technique (XRD, Bruker SMART APEX II X-ray diffractometer equipped with a Cu Kα radiation source, $\lambda = 1.5418$ Å). Morphology and elemental compositions were analyzed by transmission electron microscopy (TEM, JEOL JEM 1230 instrument operated at 120 kV) and high-resolution transmission electron microscopy equipped with energy dispersive X-ray spectrometer (FEG-TEM, JEOL JEM 2100F instrument operated at 200 kV and EDS, Oxford company model Xplore TEM). The chemical states and compositions were analyzed using X-ray photoelectron spectroscopy (XPS, Kratos Axis Ultra equipped with a focused X-ray source Al Kα, hν = 1486.6 eV). Chemical functional groups were identified by Fourier transform infrared spectroscopy (FTIR, FTS 45 infrared spectrophotometer) with the KBr pellet technique. N_2 adsorption-desorption isotherms were obtained using Brunauer-Emmett-Teller instrument (BET, Quantachrome Autosorb-1 MP analyzer). The photocurrent and impedance studies were carried out using the photo-electrochemical analyzer (Autolab PGSTAT204) equipped with 150 W Xenon arc lamp.

5.2.4 Photocatalytic activity

The photocatalytic activity of the synthesized samples was evaluated on the degradation of ciprofloxacin (CIP) molecules (10 mg/L, 100 mL of CIP and 50 mg of photocatalyst) under solar light irradiation. A 100 W Xenon arc lamp with a wavelength range of 250-1800 nm was used as a light source (ABET Sunlite solar simulator). Before the light irradiation, the reaction suspensions were stirred for 15 min in the dark to establish adsorption-desorption equilibrium between the pollutant and photocatalyst. During the process, for every 30 min, a small amount of mixture was collected and centrifuged then subjected to the optical absorbance analysis, where the degradation of CIP was measured using UV-Vis absorption spectrometer (UV-Vis, Cary 300 Bio UV-visible spectrophotometer).

5.3. Result and discussion

5.3.1 Optical property analysis

The UV-visible diffuse reflectance (UV-Vis) spectra of the as-prepared $BiVO_4$, $BiVO_4$-C_{60} and $BiVO_4$-APS-C_{60} materials are displayed in **Figure 5.1(a)**. The absorption band edge of the bare-$BiVO_4$ is located around 440 nm, whereas the $BiVO_4$-C_{60} and $BiVO_4$-APS-C_{60} composites showed a slight red-shift in their absorption edges. However, it is clear that the integration of C_{60} and APS-C_{60} has hardly impacted the overall absorption properties of the composites. This indicates that these QDs do not modify the band structure of host $BiVO_4$ via modifying their valence and conduction band as typically observed in the case of doped semiconductor photocatalysts[29,30]. Accordingly, the band gap energy of $BiVO_4$, $BiVO_4$-C_{60} and $BiVO_4$-APS-C_{60} composite, estimated using Tauc plot[34,35], is also found to be hardly varied such as 2.58, 2.50 and 2.46 eV, respectively as shown in **Figure 5.1(b)**.

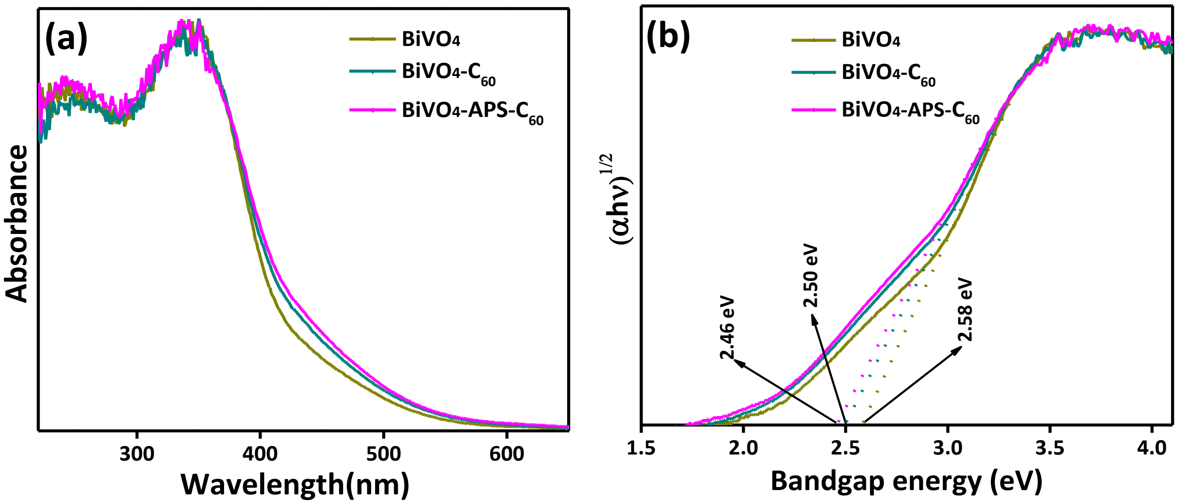

Figure 5.1. (a) UV-Vis absorption spectra and (b) Tauc plot band gap energy estimation of $BiVO_4$, $BiVO_4$-C_{60} and $BiVO_4$-APS-C_{60}.

5.3.2 Crystalline and chemical composition analysis

The X-ray diffraction (XRD) patterns of the as-prepared $BiVO_4$ and $BiVO_4$-APS-C_{60} materials are displayed in **Figure 5.2(a)**. The results showed that the as-developed materials exhibit good crystallinity and are found to be monoclinic structure with $BiVO_4$ phase (JCPDS Card 75-2480)[88, 141]. The XRD pattern of $BiVO_4$-APS-C_{60} composite is found to be similar to that of bare-$BiVO_4$ and no peaks corresponding to C_{60} were identified in its XRD pattern, which could be due to the low concentration and fine dispersion of C_{60} QDs. Further, the XRD pattern also suggested that the integration of C_{60} with $BiVO_4$ has not altered the crystal structure of $BiVO_4$ as there were no visible shift in the peaks or appearance any new peaks observed in the XRD patterns[151, 152].

The X-ray photoelectron spectroscopy (XPS) analysis provided the insights into the chemical composition and oxidation state of the elements in the $BiVO_4$-APS-C_{60} composite. The XPS survey spectrum indicated the presence of Bi, V, O, C, N and Si elements in the $BiVO_4$-APS-C_{60} composite as shown in **Figure S5.1**(supporting information). The narrow scan spectrum of $BiVO_4$-APS-C_{60} showed peaks at 162.58 and 157.28 eV corresponding to Bi $4f_{5/2}$ and Bi $4f_{7/2}$ orbital of bismuth (Bi^{3+}) as shown in **Figure 5.2(b)**. The spectrum also showed peaks at 522.51 and 514.90 eV corresponding to V $2p_{1/2}$ and V $2p_{3/2}$ orbital, and the peak appeared at 528.06 eV can be assigned to the O 1s spectrum (**Figure 5.2(c)**), which confirmed the formation of vanadate (VO_4^{3-}) frameworks[153, 154]. Then, the carbon C 1s spectrum showed three distinct peaks at 283.47, 284.8 and 286.1 eV as shown in **Figure 5.2(d)**, wherethe peak located at 283.47 and 284.8 eV could be assigned to C=C and C-C bond of C_{60}, respectively[151, 152, 155], which confirmed the presence of C_{60} in the composite. Similarly, the existence of C_{60} species in the composite was also confirmed by the Fourier transform infrared spectroscopy (FTIR) analysis as shown in **Figure 5.2(e)**. The obtained FTIR spectra showed a peak at 470 and 754 cm^{-1} corresponding to the VO_4^{3-} and V-O stretching vibration mode of $BiVO_4$, whereas, for the $BiVO_4$-C_{60} and $BiVO_4$-APS-C_{60}, these vibration peaks are found to be slightly shifted, which could be due to the interaction of C_{60} with $BiVO_4$ layers[156]. Further, the $BiVO_4$-C_{60} and $BiVO_4$-APS-C_{60} composites showed the typical IR peaks at 1410 cm^{-1} corresponding to C-C internal modes of the C_{60}, which confirmed the presence of C_{60} molecules in the composites[147, 157]. Especially, in the case of $BiVO_4$-APS-C_{60} composite, the above typical IR peaks are prominent, which indicated the strong interaction between C_{60} and $BiVO_4$ nanolayers through Bi-V-O-Si-C networks established by APS. The peak appeared at 2350 and 3647 cm^{-1} could be assigned to the stretching vibration of carbon dioxide molecule and O-H groups on the surface of the composites[158, 159]. However, no peaks corresponding to APS (i.e. Si-O) are found in the FTIR spectra due to the smaller concentration of APS in the $BiVO_4$-APS-C_{60} composite.

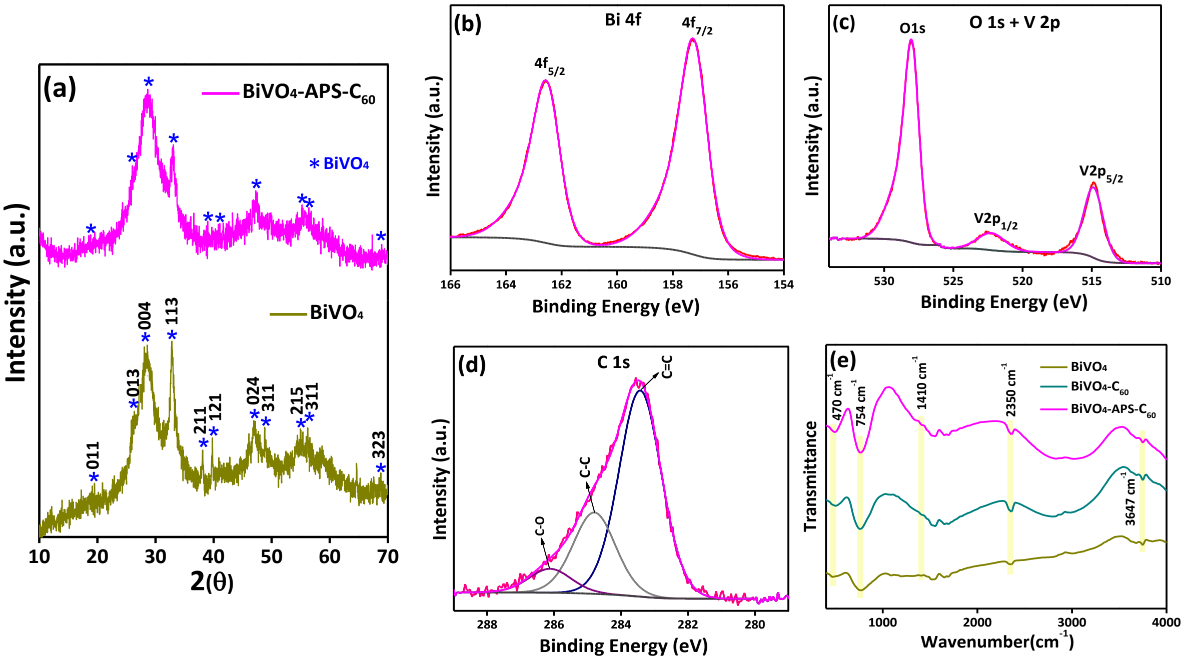

Figure 5.2. (a) X-ray diffraction spectra of $BiVO_4$ and $BiVO_4$-APS-C_{60} and X-ray photoelectron spectra of $BiVO_4$-APS-C_{60} (b) Bi 4f, (c) O 1s + V 2p, (d) C 1s, and (e) FTIR spectra of $BiVO_4$, $BiVO_4$-C_{60} and $BiVO_4$-APS-C_{60}.

5.3.3 Morphology and surface area analysis

The morphology of the synthesized $BiVO_4$, $BiVO_4$-C_{60} and $BiVO_4$-APS-C_{60} materials was investigated by transmission electron microscopy (TEM) and high-resolution transmission electron microscopy (HR-TEM) and the obtained images are displayed in **Figure 5.3(a-c)** and **Figure 5.3(d-e)**, respectively. The TEM images revealed that the $BiVO_4$ are formed like a layered structure with a length in the range of around 500 nm to 1.5 μm and found to be curved-like indistinguishable ultrathin layer structures[141, 160]. Similarly, the morphology of $BiVO_4$-C_{60} and $BiVO_4$-APS-C_{60} composites was also found to be ultrathin layer-like structures. However, as compared to the bare $BiVO_4$, the layers of $BiVO_4$-C_{60} and $BiVO_4$-APS-C_{60} are relatively less aggregated, which could be due to the effect of fine dispersion of CQDs between the layers that assembled the layers without aggregation. However, the presence of CQDs is not clear in the TEM images due to their smaller size and low concentration. Therefore, the HR-TEM images of the samples were obtained and given in **Figure 5.3(d-e)**, which clearly showed that the C_{60} QDs are highly dispersed on the surface as well in the inter-layer regions of $BiVO_4$. The size of C_{60} QDs was estimated to be around 5 nm in the $BiVO_4$-APS-C_{60} composite. Further, the elemental mapping using energy dispersive X-ray spectroscopy (EDS) was performed and it confirmed the presence and distribution of C_{60} QDs and APS in the $BiVO_4$-APS-C_{60} composite as displayed in **Figure 5.3(f-l)**. The mapping results showed the presence of elements such as Bi, V, O, C, Si and N in the $BiVO_4$-APS-C_{60} composite as corroborated from the XPS survey spectrum of the sample.

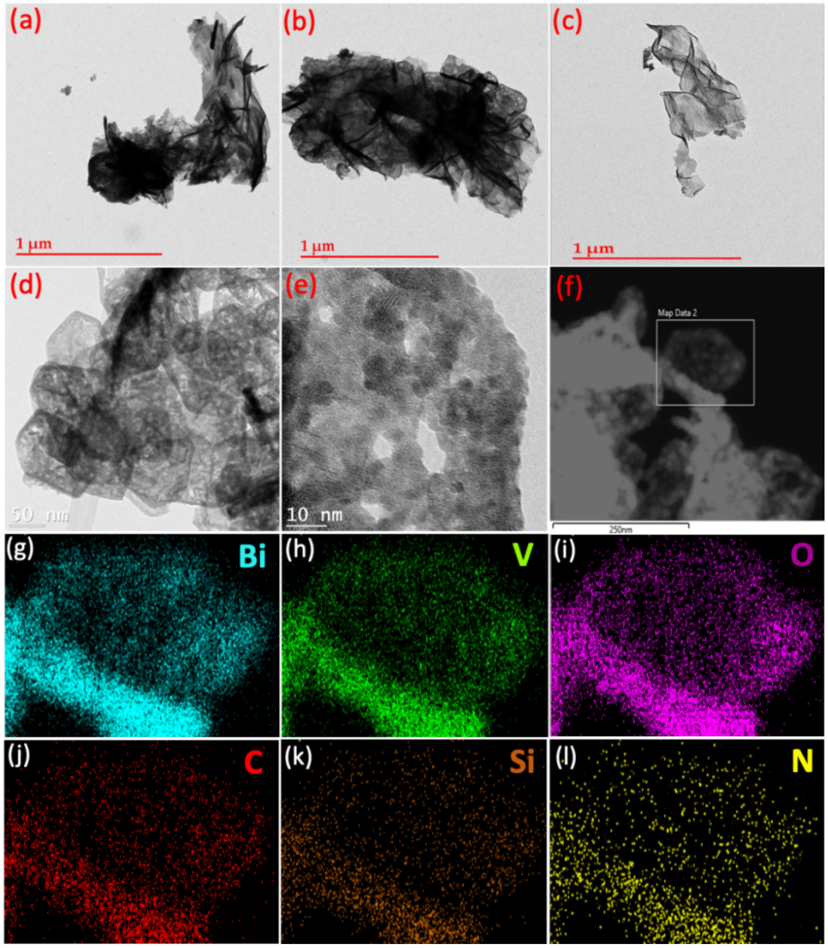

Figure 5.3. TEM image of (a) $BiVO_4$, (b) $BiVO_4$-C_{60}, (c) $BiVO_4$-APS-C_{60}, (d-e) HR-TEM images of $BiVO_4$-APS-C_{60} and (f-l) EDS elemental mapping of $BiVO_4$-APS-C_{60} composite.

The Brunauer-Emmett-Teller (BET) specific surface area of the as-prepared materials was investigated using nitrogen (N_2) adsorption-desorption measurements and the obtained results are shown in **Figure S5.2** (supporting information). It has been widely recognized that materials with more active sites, porous in nature and have layer structures can have larger specific surface area, which eventually allow for an enhanced adsorption of pollutants and leading to the effective photocatalytic activity[13, 161]. Accordingly, the surface area of $BiVO_4$ and $BiVO_4$-C_{60} and $BiVO_4$-APS-C_{60} was estimated to be around 95.22, 97.86 and 99.74 m^2/g, respectively. This slight increment in the surface area of the composites could be attributed to their decreased inter-layer distances and assembly of $BiVO_4$ layers due to the presence of CQDs.

5.3.4 Charge separation and transfer studies

The photoluminescence (PL) analysis was performed to determine the separation and migration characteristics of the charge carriers in the as-developed $BiVO_4$, $BiVO_4$-C_{60} and $BiVO_4$-APS-C_{60} materials and the obtained results are given in **Figure 5.4(a)**. As compared to the pure $BiVO_4$, the composites $BiVO_4$-C_{60} and $BiVO_4$-APS-C_{60} showed a significantly decreased PL intensity, which revealed that there could be a greater separation of the photo-generated electron-hole pairs and increased recombination resistance in the system[143]. Such enhancement could be attributed to the delocalized carbon structure of C_{60} QDs and their intimate interfacial contact with $BiVO_4$ layers, which offers a fast charge transfer and prolonged lifetime for the excited carriers[151, 162]. This observed result also confirmed that the recombination of the photo-generated electron-hole is greatly inhibited by the addition of C_{60}. Also, as the aminosilicate functional groups increase the dispersion ability of C_{60} onto the $BiVO_4$-layers, they facilitate the faster charge transfer at the interfaces and improve the overall charge separation efficiency in the $BiVO_4$-APS-C_{60} composite[163]. In addition, the charge separation and transfer efficiencies of the systems were also corroborated with the photoelectrochemical (PEC) investigations. The photocurrent densities of the as-prepared $BiVO_4$, $BiVO_4$-C_{60} and $BiVO_4$-APS-C_{60} materials were measured by chronoamperometry technique with the light on-off process under solar light irradiation and the obtained results are shown in **Figure 5.4(b)**. The composite system showed highly reproducible photocurrent, and the intensity goes down to zero when the light was turned off and it resumed back to the higher density when the light was turned on[152, 164]. Among these systems, the as-prepared $BiVO_4$-C_{60} and $BiVO_4$-APS-C_{60} composites displayed much higher photocurrent density of around 2.87 and 3.36 $\mu A/cm^2$, respectively as compared to the bare-$BiVO_4$ (1.09 $\mu A/cm^2$).

The mechanism of such enhancement could be attributed to the factors that the C_{60} QDs act as an electron trapper and their delocalized π-π conjugated structure delivers the adequate potential for the effective charge transfer in the system[147, 151]. Therefore, it is realized that both the bare-C_{60} and APS functionalized-C_{60} can potentially reduce the charge recombination process in $BiVO_4$ and thus improve the photocurrent efficiency in the composites[163]. The Nyquist plots of the as-prepared materials were obtained using the electrochemical impedance technique and the obtained plots are displayed in **Figure 5.4(c)**.

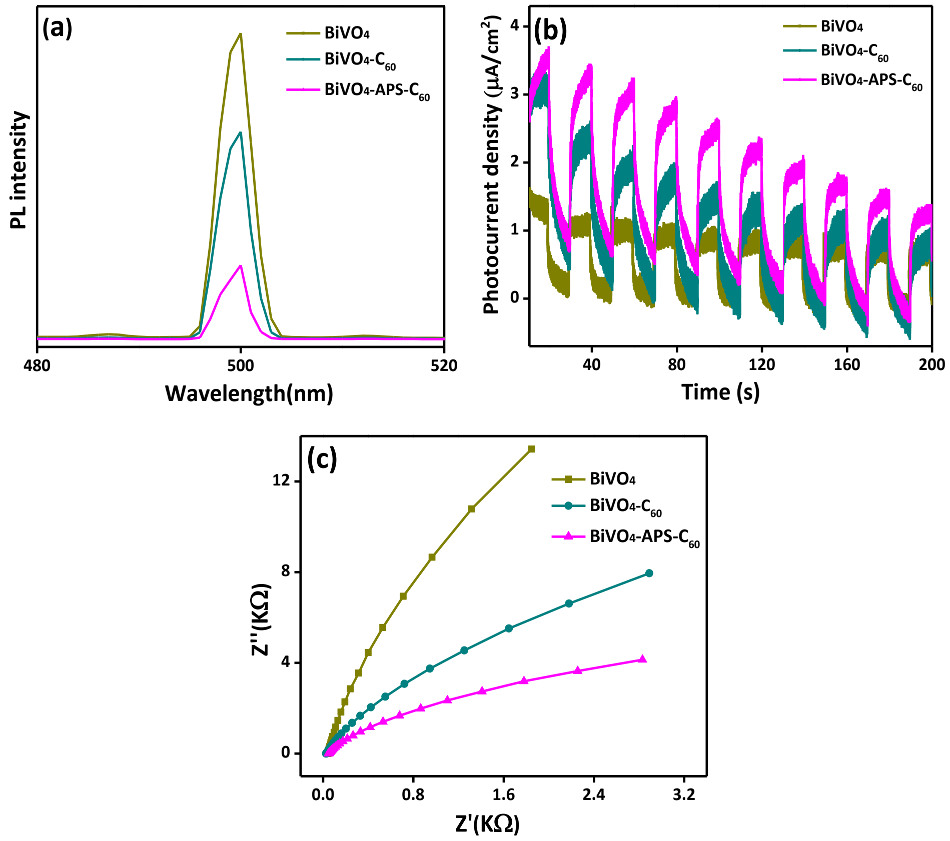

Figure 5.4. (a) Photoluminescence, (b) Chronoamperometric and (c) Nyquist plots of $BiVO_4$, $BiVO_4$-C_{60} and $BiVO_4$-APS-C_{60}.

The results showed that there could be a reduced charge transfer resistance in the $BiVO_4$-C_{60} and $BiVO_4$-APS-C_{60} composites as compared to that of the bare $BiVO_4$. This observed reduced resistance could be due to the enhanced delocalization of the electrons excited in $BiVO_4$ and C_{60}, which facilitated the rapid transfer of photoinduced electrons in the composites with lesser resistivity at the interfaces[151, 165]. All these obtained results demonstrate that the $BiVO_4$-APS-C_{60} composite could possess effective electron-hole charge separation and lower charge recombination, which could be due to the strong interconnection between the $BiVO_4$ ultrathin layers and APS-C_{60} through the network of Bi-V-O-Si-C in the system.

5.3.5 Photocatalytic degradation studies

The photocatalytic performances of the as-prepared $BiVO_4$, $BiVO_4$-C_{60} and $BiVO_4$-APS-C_{60} materials were studied on the degradation of antibiotic ciprofloxacin (CIP) molecules under solar light irradiation and the obtained degradation results are shown in **Figure 5(a)** and the time depended degradation spectra are shown in **Figure S5.3(a-c)** (supporting information)[119, 166]. The $BiVO_4$, $BiVO_4$-C_{60} and $BiVO_4$-APS-C_{60} composite showed the highest degradation efficiency of 41.8, 65.4 and 85.42%, respectively at the end 180 min. As compared to bare-$BiVO_4$, the composites $BiVO_4$-C_{60} and $BiVO_4$-APS-C_{60} are found to have around 0.6 and ~1.1 folds higher degradation efficiency, where this efficiency can be primarily attributed to the presence of C_{60}. In the composite system, the C_{60} QDs show multifunctional activity via enhanced adsorption of CIP molecules, enhanced charge separation and transfer to improve the photocatalytic properties of the composite. Also, the incorporation of C_{60} paved the ways to manifest the additional pathways for the effective charge transfer during the photocatalytic process in the system. Such collective processes offer a better charge exciton diffusion length, increased photocurrent conductivity and photocatalytic efficiency for the $BiVO_4$-APS-C_{60} composite[146, 147, 167]. In addition, the higher specific surface area and the increased number of reactive sites in the composite also favoured for the higher photocatalytic activity in the system.

Similarly, the energy band structure is a crucial factor in enhancing the photocatalytic properties of the materials. As observed, the $BiVO_4$-APS-C_{60} material showed narrow band gap energy as compared to $BiVO_4$-C_{60} and bare-$BiVO_4$, which facilitated an extended photo-absorbance in the system. Meanwhile, the optimum conduction band potential (-0.90 eV) and valence band potential (+1.56 eV) of $BiVO_4$-APS-C_{60} composite (as calculated from the XPS valence band spectrum as shown in **Figure S5.4**) facilitated the formation of more number of active species through a rapid photo-redox reaction with higher charge separation efficiencies in the system. Accordingly, these remarkable synergetic effects between $BiVO_4$

and aminosilicate functionalized-C_{60} significantly improved the overall photocatalytic performance of the $BiVO_4$-APS-C_{60} composites[168]. A schematic illustration demonstrating the observed enhanced photocatalytic activity in $BiVO_4$-APS-C_{60} composite is displayed in **Figure 5.5(b)**. In this process, the aminosilicate functionalized fullerene (APS-C_{60}) QDs rapidly accept the photogenerated electrons from $BiVO_4$ and transfer them to the surface-adsorbed oxygen to produce the superoxide radicals; meanwhile, the holes generate hydroxyl radicals during the reaction[152, 169]. Moreover, the incorporation of fullerenes can effectively slow down the recombination rate of electrons-holes and improve the lifetime of the photogenerated electrons thereby it collectively improved the degradation efficiency of the composite[167].

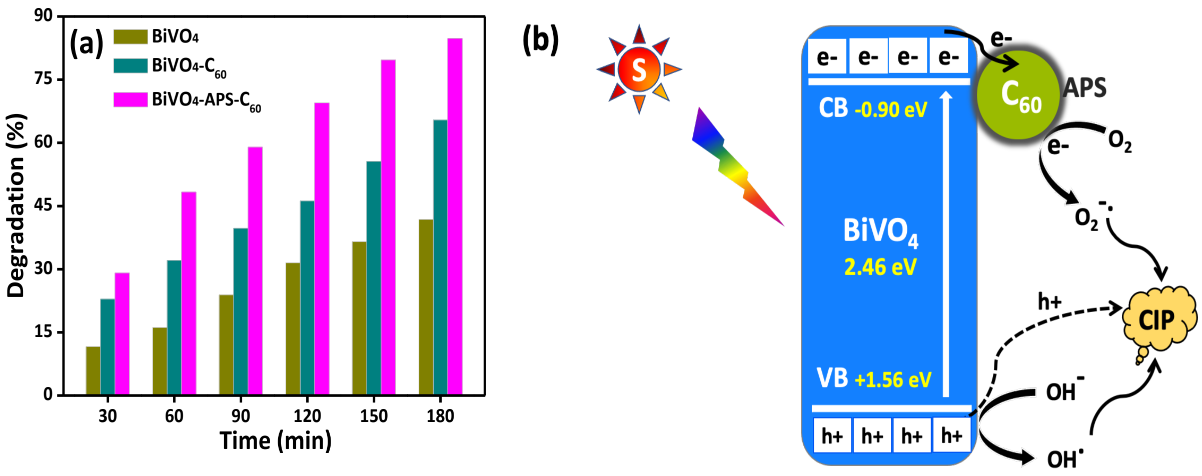

Figure 5.5. (a) Photocatalytic degradation of antibiotic ciprofloxacin by $BiVO_4$ and $BiVO_4$-C_{60} and $BiVO_4$-APS-C_{60} under solar light irradiation and (b) Proposed photocatalytic degradation mechanism of $BiVO_4$-APS-C_{60}.

For further insights into in the photocatalytic mechanism, the degradation of ciprofloxacin was studied by introducing various scavengers such as triethanolamine (h^+), isopropyl alcohol ($OH^\bullet$) and p-benzoquinone ($O_2^{\bullet -}$). The influence of the scavengers towards the degradation of ciprofloxacin over $BiVO_4$-APS-C_{60} composite is displayed in **Figure 5S.5** (supporting information). It was observed that the degradation efficiency was dropped to 50.6, 79.5 and 65.8% in presence of triethanolamine (h^+), isopropyl alcohol ($OH^\bullet$) and p-benzoquinone ($O_2^{\bullet -}$), respectively, while it was 85.42% without adding any scavengers in the reaction system[50, 170]. From these results, it is realized that the active species for the degradation of ciprofloxacin could be h^+ followed by $O_2^{\bullet-}$ radicals. Further, the recycle test revealed the stability of $BiVO_4$-APS-C_{60} composite, where itshowed that the degradation efficiency of this composite did not get decreased up to five recycles. However, the degradation efficiency of $BiVO_4$-C_{60} composite is comparably decreased (**Figure S5. 6(a-b)**), which may be ascribed to the factor that they were not APS functionalized. This suggested that the presence of APS has potentially improved the binding of C_{60} onto the surface of $BiVO_4$ ultrathin layers and efficiently prevented the leaching of C_{60} from the $BiVO_4$ surface thereby the stability of the composite is preserved for repeatable uses[171, 172]. Also, a comparative study of a various photocatalyst systems and their photocatalytic efficiency towards the degradation ciprofloxacin is displayed in **Table S5.1** (supporting information).

5.4. Conclusion

In this work, an efficient $BiVO_4$-APS-C_{60} composite was developed by integrating the aminosilicate-functionalized-C_{60} QDs on the surface of ultrathin $BiVO_4$ nanolayers. It was found that the as-developed $BiVO_4$-APS-C_{60} displayed much higher photocatalytic activity towards ciprofloxacin degradation under solar light irradiation. The observed boosted photocatalytic performance was mainly attributed to a couple of factors. First, the integration of C_{60} on $BiVO_4$ improved the photo-redox properties of the composite via the optimal valence and conduction band potential, effective generation and separation of the photoinduced charge carriers. Second, the functional group of aminosilicate established a strong interfacial interaction between C_{60} and $BiVO_4$, which provided a remarkable charge transfer efficiency and stability for the $BiVO_4$-APS-C_{60} composite. Further, the scavenger studies demonstrated that the h^+ and $O_2^{\bullet-}$ radical species were the main reactive species involved in the ciprofloxacin degradation over the developed $BiVO_4$-APS-C_{60} composite system.

Acknowledgements

This work was supported by the Natural Science and Engineering Research Council of Canada (NSERC) through the Strategic Project (SP), and Discovery Grants. The authors would like to thank Exp Inc. and SiliCycle Inc. for their support.

5.5. Supporting information

5.5.1. X-ray photoelectron spectra (XPS)

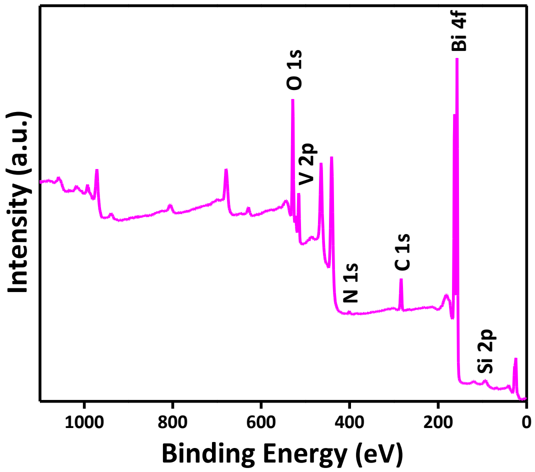

Figure S5.1. XPS survey spectrum of $BiVO_4$-APS-C_{60}.

5.5.2. Brunauer-Emmett-Teller (BET) analysis

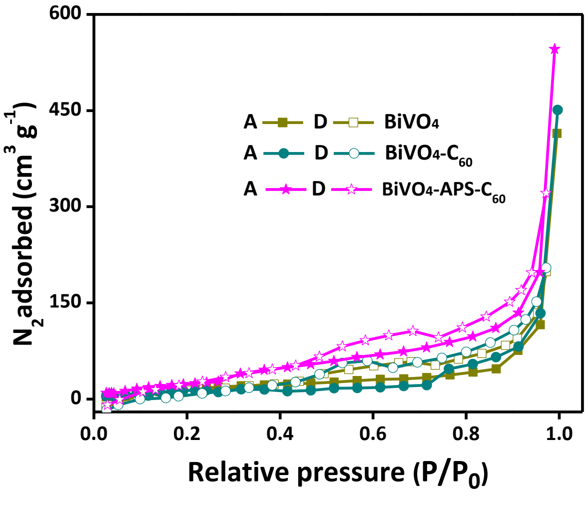

Figure S5.2. Nitrogen adsorption-desorption isotherm of $BiVO_4$, $BiVO_4$-C_{60} and $BiVO_4$-APS-C_{60}.

5.5.3. Photocatalytic degradation of ciprofloxacin

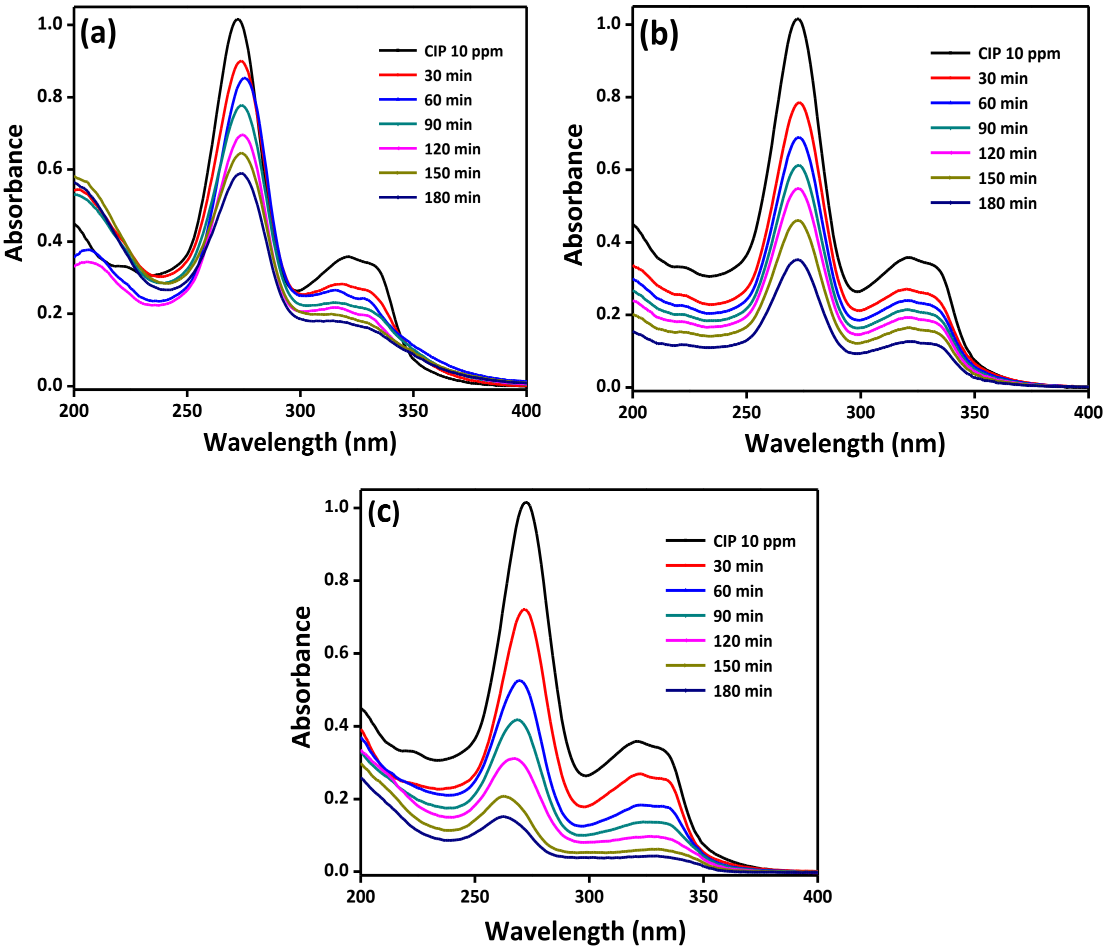

Figure S5.3. UV-vis absorbance spectra of degradation of ciprofloxacin in presence of (a) $BiVO_4$, (b) $BiVO_4$-C_{60} and (c) $BiVO_4$-APS-C_{60}.

5.5.4. Band energy calculation

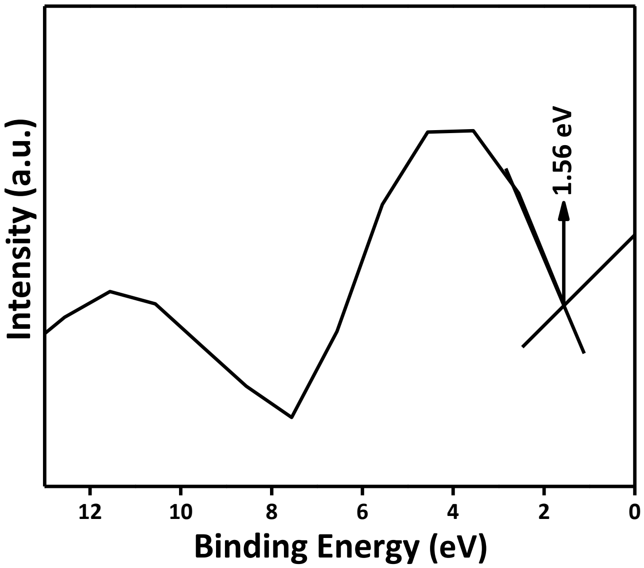

Figure S5.4. XPS spectrum of valence band value of $BiVO_4$-APS-C_{60}.

5.5.5. Scavenger test

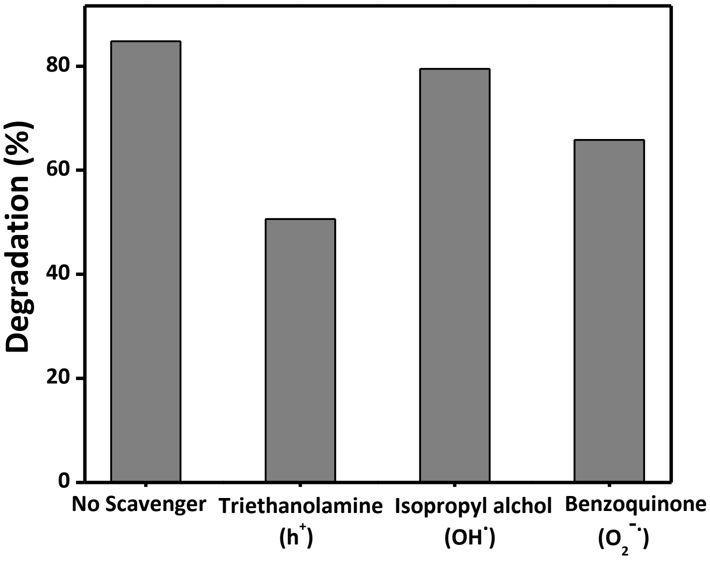

Figure S5.5. Radicals scavenger test over $BiVO_4$-APS-C_{60}.

5.5.6. Recyclability of photocatalyst

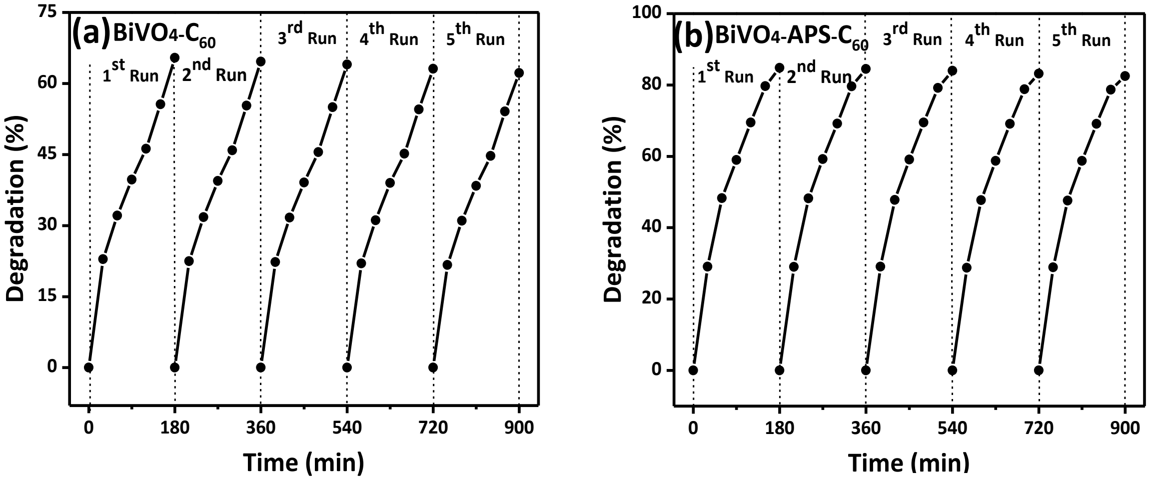

Figure S5.6. Recyclability study of (a) $BiVO_4$-C_{60} and (b) $BiVO_4$-APS-C_{60}.

5.5.7. Photocatalytic degradation of catalyst compared with related photocatalysts

Photocatalyst	**Light source**	**Pollutant**	**Degradation efficiency (%)**	**Time (min)**	**References**
NiS/MoS$_2$/g-C$_3$N$_4$ (1 mg/1 mL)	Visible light (250 W)	Ciprofloxacin (10 ppm)	71.3	120	[173]
Ag$_3$PO$_4$-NPs/Cu (0.2 mg/1 mL)	Visible light (500 W)	Ciprofloxacin (10 ppm)	85	180	[174]
BiVO$_4$-APS-C$_{60}$ (0.5 mg/1 mL)	Solar light (100 W)	Ciprofloxacin (10 ppm)	85.4	180	**This work**
Bi/Bi$_3$NbO$_7$ (0.5 mg/1 mL)	Visible light (300 W)	Ciprofloxacin (10 ppm)	86	120	[175]
CuS/BiVO$_4$ (1 mg/1 mL)	Visible light (300 W)	Ciprofloxacin (10 ppm)	86.7	90	[176]
Bi$_3$TaO$_7$/g-C$_3$N$_4$ (0.5 mg/1 mL)	Visible light (86 W)	Ciprofloxacin (10 ppm)	91	120	[119]
Ag/AgCl/Ag$_2$O (1 mg/ 1 mL)	Visible light (250 W)	Ciprofloxacin (10 ppm)	91.2	100	[177]
g-C$_3$N$_4$/TiO$_2$/kaolinite (2 mg/1 mL)	Visible light (90 W)	Ciprofloxacin (10 ppm)	92	240	[178]

Table S5.1. Comparative table showing the photocatalysts reported in the literature for ciprofloxacin degradation.

Chapter 6 : Amine-functionalized metal-organic framework integrated bismuth tungstate (Bi_2WO_6/NH_2-UiO-66) composite for the enhanced solar-driven photocatalytic degradation of ciprofloxacin molecules

K. Rokesh, M. Sakar, Trong-On Do*

Department of Chemical Engineering, Laval University, Québec (Québec), G1V 0A6, Canada

*E-mail: trong-on.do@gch.ulaval.ca

This chapter is submitted in New Journal of Chemistry 2021,10.1039/D1NJ03977F

Résumé

Le nanocomposite de tungstate de bismuth intégré avec métal organic framework fonctionnalisé par une amine (Bi_2WO_6/NH_2-UiO-66) a été développé par croissance in situ de NH_2-UiO-66 sur Bi_2WO_6 ayant une forme micro/nanoflorale via une technique hydrothermale. Ce nanomatériau a été étudié pour son activité photocatalytique envers la dégradation de la ciprofloxacine sous rayonnement solaire. L'intégration de NH_2-UiO-66 avec micro/nanoflorale de Bi_2WO_6 a élargi le domaine d'absorption lumineuse ainsi que la surface spécifique de nanocomposite Bi_2WO_6/NH_2-UiO-66. Il a été noté que la liaison amine a établi un fort contact interfacial entre NH_2-UiO-66 et Bi_2WO_6 et a formé une hétérojonction de type Z-schème. Cette dernière permet d'améliorer la séparation des paires électrons-trous photo-induits ainsi que la cinétique de transfert de charge, et de fournir de forts sites d'oxydation et de réduction au nanocomposite. De plus, le trou h^+ et le radical $O_2^{\bullet-}$ ont été identifiés comme les principales espèces actives dans le processus photocatalytique de nanocomposite, et ainsi un mécanisme photocatalytique possible a été également proposé.

Abstract

Amine-functionalized metal organic framework integrated bismuth tungstate (Bi_2WO_6/NH_2-UiO-66) nanocomposite has been developed by *in-situ* growth of NH_2-UiO-66 on Bi_2WO_6 micro/nanoflower via hydrothermal technique and studied their photocatalytic performance towards ciprofloxacin degradation under solar light irradiation. The integration of NH_2-UiO-66 with Bi_2WO_6 micro/nanoflower extended the photo-absorption and specific surface area of the Bi_2WO_6/NH_2-UiO-66 composite. It is observed that the amine linkage established a strong interfacial contact between the NH_2-UiO-66 and Bi_2WO_6 micro/nanoflower and formed the Z-scheme heterojunction in the composite. The Z-scheme heterojunction is found leading to the effective photo-induced electron-hole pair separation, charge transfer kinetics and provide strong oxidation and reduction sites in the composites. Besides, the h^+ and $O_2^{\bullet-}$ radicals have been identified as major reactive species responsible for the photocatalytic process in the composite, and thereby a possible photocatalytic mechanism has also been proposed.

6.1. Introduction

The rising occurrence of pharmaceuticals compounds in global water sources has received emerging concerns because of the specific environmental risks and potential impact on ecosystems and human health[2, 3]. Among them, the antibiotics have become a growing concern due to their possible threat of generation of antibiotic-resistance in microorganism and genotoxic effects. The antibiotic residues generate stable organic by-products which lead to secondary pollutant generation, and it could produce serious toxicity and long-term chronic effects into humans and aquatic species and hence, they are considered as an emerging pharmaceutical contaminant[4, 7, 132]. As a result, there is an urgent need to find an efficient technique for the careful removal of emerging antibiotic pollutants from water system. There are numerous techniques available to remove antibiotic residues from water, which include adsorption, microbial degradation, photocatalysis, ozonolytic, electrocatalysis and membrane filtration[9, 93, 94, 179]. Among these techniques, the semiconductor-based solar photocatalytic technique has found to be of a great interest because of their strong redox property offering a high degradation efficiency and non-toxic by-product generation[12, 180]. Especially, the hybrid nanocomposite photocatalytic materials have been found to show higher antibiotics degradation efficiency. These hybrid photocatalysts are found as the systems with suitable characteristic properties such as superior structural, interface, surface properties, and thereby, enhanced photo-absorbance, charge-separation, -transfer, redox ability and photostability of the systems[11, 137, 181]. Recently, a wide range of bismuth-based materials has been developed and studied for photocatalytic antibiotics degradation[123, 182-185]. Of these materials, the layer-structured bismuth tungstate (Bi_2WO_6) materials have been found to be of great interest in the field of photocatalysis due to their visible light driven bandgap energy (2.7 eV), structural tunability, chemical stability, and non-toxicity. However, their practical application towards photocatalytic process is limited by their low specific surface area, high electron-hole recombination, slow charge transfer and weak hydrophilicity[186-189]. To overcome these limitations, coupling Bi_2WO_6 with other semiconductors to construct as a hybrid composite could be the efficient way to achieve the desired high photocatalytic performance. This hybrid structure essentially offers a favorable band structure-alignment and efficient interfacial contact in the system. Therefore, considerable efforts have been made to improve the charge carrier separation efficiency by constructing the Bi_2WO_6 nanostructure-based heterojunctions with other semiconductors[190, 191]. In this direction, it is emerging that the incorporation of metal-organic frameworks (MOFs) with Bi_2WO_6 nanosheet could be an efficient way to overcome the above limitation of high charge recombination and to offer efficient charge separation and fast transfer rates in the system[192, 193]. MOFs are porous crystalline materials linked by organic ligands with transition metals and possess unique properties such as tunable porous structure, high designability, high surface area and strong adsorption ability[194]. Among them, the UiO-66 is one of the widely studied zirconium-based MOFs for photocatalytic applications owing to their large surface area, visible light absorbance and relatively high structural stability in aqueous system. However, the photocatalytic efficiency of UiO-66 is still limited due to their low charge separation, conductivity and photo-activity. It is found that while introducing the amino functional groups into UiO-66 towards extending the photo-absorption ranges in the visible region, it possibly provides strong connection between the interface of composite counterparts, and thereby it becomes efficient to improve the charge separation and migration of photogenerated charge carriers and to increase the stability of composites[195, 196]. Therefore, the incorporation of amine-functionalized UiO-66 (NH_2-UiO-66) with Bi_2WO_6 materials can provide efficient pathways for the charge migration and lead to the efficient photo-induced charge carrier separation in the system. In addition, the combination of these materials may lead to the establishment of a Z-scheme charge transfer mechanism and thus it will enhance overall redox potential in the composite system, which will eventually be beneficial towards achieving high photocatalytic efficiency. In this context, herein, we have developed a hybrid system based on NH_2-UiO-66 integrated Bi_2WO_6 via a two-step hydrothermal technique. The incorporation of NH_2-UiO-66 with Bi_2WO_6 micro/nanoflower is found to potentially enhance the overall visible light absorbance of the composite and improve the charge separation and transfer efficiency in the system. Hence, the Bi_2WO_6/NH_2-UiO-66 composite exhibited a significantly higher photocatalytic activity towards antibiotic degradation under solar light irradiation.

6.2. Materials and methods

6.2.1 Chemicals

The chemicals such as bismuth nitrate pentahydrate ($Bi(NO_3)_3•5H_2O$), sodium tungstate dihydrate ($Na_2WO_4•2H_2O$), cetrimonium bromide (CTAB, $C_{19}H_{42}BrN$), zirconium tetrachloride ($ZrCl_4$), terephthalic acid ($C_8H_6O_4$), 2-aminoterephthalic acid ($C_8H_7NO_4$), N, N-dimethylformamide (DMF, C_3H_7NO) were obtained from Sigma Aldrich and used without any further purification.

6.2.2 Materials preparations

i) Preparation of Bi_2WO_6 micro/nanoflower: In a typical procedure, 2 mmol (0.97 g) of $Bi(NO_3)_3•5H_2O$, 1 mmol (0.33 g) of $Na_2WO_4•2H_2O$ and 0.05 g of CTAB were added to 80 mL of deionized water. After 30 min of stirring, the reaction mixture was transferred into a 140 mL Teflon-lined autoclave, sealed and heated at 120 °C for 24 h. The autoclave was naturally cooled to room temperature and the obtained final product was washed with deionized water and ethanol followed by drying at 80 °C for 10 h (**Scheme 6.1**).

ii) Preparation of Bi_2WO_6/UiO-66 and Bi_2WO_6/NH_2-UiO-66 composites: In this procedure, 0.25 g of the synthesized Bi_2WO_6 micro/nanoflower were dispersed into 20 mL of DMF solution and sonicated for 30 min. Then, 0.025 g of $ZrCl_4$ in 20 mL of DMF solution was added to the above solution and stirred for 30 min. Later, 0.05 g of terephthalic acid or 2-aminoterephthalic acid was dissolved in 20 mL of DMF solution and added into the above mixture and stirred for 30 min. Afterwards, the reaction mixture was transferred into a 140 mL of Teflon-lined autoclave, sealed and heated at 120 °C for 24 h. The final obtained products were washed with ethanol for several times, and then heated in an oven at 80 °C for overnight (**Scheme 6.1**).

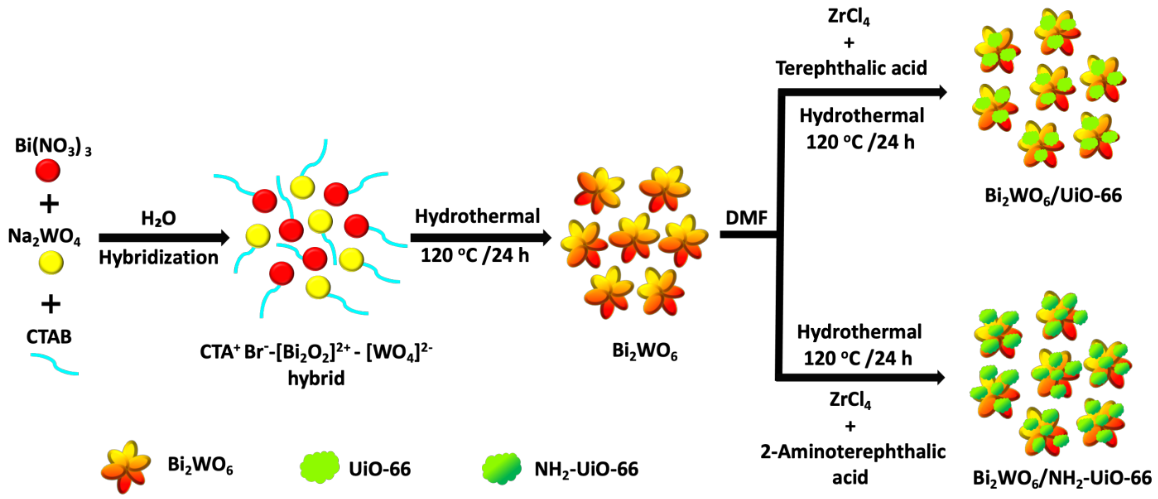

Scheme 6.1. Synthesis process of bare-Bi_2WO_6, Bi_2WO_6/UiO-66 and Bi_2WO_6/NH_2-UiO-66 composites via two-step hydrothermal technique.

6.2.3 Characterizations

The optical property was studied using UV-Visible spectroscopy (Cary 300 Bio UV-visible spectrophotometer). Crystalline nature of the materials was studied using X-ray diffraction technique (Bruker SMART APEX II X-ray diffractometer equipped with a Cu Kα radiation source, $\lambda = 1.5418$ Å). Chemical functional groups were identified using Fourier transform infrared spectroscopy (FTS 45 infrared spectrophotometer) with the KBr pellet technique. Morphology and structure of the materials were analyzed by scanning electron microscopy (FEI Inspect F50) and transmission electron microscopy (JEOL JEM 1230 instrument operated at 120 kV). The elemental compositions were identified by energy dispersive X-ray spectroscopy (Edax Ametek Octane Super-A). Surface area was measured by nitrogen adsorption-desorption isotherms technique using Brunauer-Emmett-Teller instrument (Quantachrome Autosorb-1 MP analyzer). Emission spectra were obtained using photoluminescence spectrometer (HORIBA PTI Quanta Master 500 spectrofluorometer). The photoelectrochemical properties were studied using a photo-electrochemical analyzer (Autolab PGSTAT 204) using 100 W Xenon arc lamp.

6.2.4 Photocatalytic experiment

Photocatalytic performance of the synthesized materials was examined for the degradation of antibiotic ciprofloxacin under solar irradiation. In the typical experiment, 25 mg of photocatalyst was suspended in 100 mL of ciprofloxacin (10 ppm) solution. 100 W Xenon arc lamp with a wavelength range of 250-1800 nm was used as a light source (ABET Sunlite solar simulator). Prior to the reaction, the photocatalyst-pollutant solution mixture was stirred in the dark for 15 min to establish adsorption-desorption equilibrium, and later the suspension was kept under continuous light exposure for the degradation. For every 10 min, a small amount of reaction-solution was collected and centrifuged and monitored for their optical absorbance intensity using UV-Vis absorption spectrometer (UV-Vis, Cary 300 Bio UV-visible spectrophotometer), which can be directly correlated to amount of antibiotics degraded.

6.3. Result and discussion

6.3.1 Optical properties

The UV-Visible diffuse reflectance (UV-Vis) spectra of the synthesized bare-Bi_2WO_6, Bi_2WO_6/UiO-66 and Bi_2WO_6/NH_2-UiO-66 composites are presented in **Figure 6.1(a)**. In comparison with bare-Bi_2WO_6, the absorption band edges of Bi_2WO_6/UiO-66 and Bi_2WO_6/NH_2-UiO-66 composite were blue and red shifted, respectively. Since the UiO-66 is typically a UV-light active, whereas the amine functionalized UiO-66 exhibits visible light absorbance, therefore, the incorporation of UiO-66 reduced the overall photoabsorbance of Bi_2WO_6/UiO-66 composites towards UV region and NH_2-UiO-66 extended the photoabsorbance of Bi_2WO_6/NH_2-UiO-66 towards the visible light region[197-199]. Hence, the existence of amine group in NH_2-UiO-66 and their effective interface interaction with Bi_2WO_6 could form a complemented strong heterostructure with broad spectral response ranges in the visible light region[196]. Further, the band gap energy of bare-Bi_2WO_6, Bi_2WO_6/UiO-66 and Bi_2WO_6/NH_2-UiO-66 composites were estimated using Tauc's plot and found to be 2.71, 2.79 and 2.58 eV, respectively as shown in **Figure 6.1(b)**[186, 200, 201]. The band gap energy is found to be increased due to the incorporation of UiO-66 and it is decreased upon the incorporation of NH_2-UiO-66, due to which, the Bi_2WO_6/NH_2-UiO-66 composite exhibited relatively a narrow band gap and extended visible light absorbance.

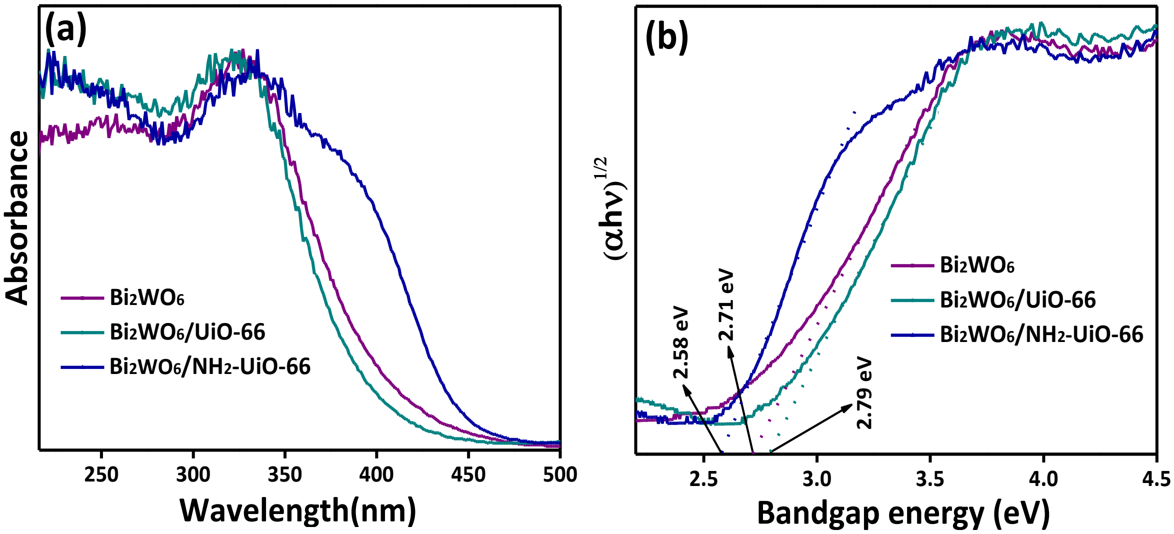

Figure 6.1. (a) UV-Vis absorption spectra and (b) Tauc plot band gap energy estimation of bare-Bi_2WO_6, Bi_2WO_6/UiO-66 and Bi_2WO_6/NH_2-UiO-66 composites.

6.3.2 Structural and chemical composition

The X-ray diffraction (XRD) patterns of the synthesized bare-Bi_2WO_6, Bi_2WO_6/UiO-66 and Bi_2WO_6/NH_2-UiO-66 composites are given in **Figure 6.2(a)**. The prepared materials have shown excellent crystalline properties with sharp diffraction peaks. The obtained patterns confirmed the orthorhombic structure of Bi_2WO_6 (JCPDS No. 73-2020)[36, 202]. The Bi_2WO_6/UiO-66 and Bi_2WO_6/NH_2-UiO-66 composites showed similar XRD patterns to those of Bi_2WO_6, and the peaks corresponding to UiO-66 and NH_2-UiO-66 were also identified in the XRD pattern of the respective composites. The peaks corresponding to Bi_2WO_6 were not shifted even after the incorporation of UiO-66 and NH_2-UiO-66, which revealed that the integration of these MOFs did not influence the crystal structure of Bi_2WO_6. For the composites, the peaks at 7.25°, 23.31° and 25.74° are corresponding to the UiO-66 and NH_2-UiO-66, but their peak intensities are relatively low due to their lower concentrations in the composites[197, 203]. As compared to Bi_2WO_6/UiO-66, the Bi_2WO_6/NH_2-UiO-66 showed a major intensity peak at 7.25°, which can be attributed to the strong binding properties between the -NH_2 groups in UiO-66 and Bi_2WO_6 [199]. Furthermore, the obtained sharp diffraction peaks and absence of any other unknown peaks indicated the crystallinity and purity of the synthesized materials. The existence of various chemical functional groups in the materials were confirmed by Fourier transform infrared spectroscopy (FTIR) analysis as shown in **Figure 6.2(b)**. The characteristic peak obtained at 730 cm^{-1} corresponds to W-O stretching vibration of the Bi_2WO_6 material, while the vibration peaks of Bi_2WO_6/NH_2-UiO-66 was slightly shifted towards higher wavenumber as compared to Bi_2WO_6/UiO-66 composite, which could be due to the strong interaction of NH_2-UiO-66 with Bi_2WO_6[204]. The composites Bi_2WO_6/UiO-66 and Bi_2WO_6/NH_2-UiO-66 displayed peaks at 1380 and 1562 cm^{-1} related to the symmetric and asymmetric carboxylate (O-C=O) group, respectively of the UiO-66 and NH_2-UiO-66. The weak vibration at 1506 cm^{-1} is ascribed to the C=C of benzene ring in the UiO-66 and NH_2-UiO-66[198, 205, 206]. Besides, the Bi_2WO_6/NH_2-UiO-66 composite displayed a peak at 1249 cm^{-1}, which could be assigned to the C-N stretching vibration of aromatic amines and the peak at 1628 cm^{-1} represents the N-H bending vibration of NH_2-UiO-66. These results confirmed the presence of -NH_2 linker in the composite and found to be prominent Bi_2WO_6/NH_2-UiO-66 composite due to their strong interaction at their interfaces[196, 207]. The IR spectra also showed a peak at 3400 cm^{-1} corresponding to the stretching vibration of -OH group in the materials, whereas, in Bi_2WO_6/NH_2-UiO-66 composites, these vibration peaks are relatively broad, which could be attributed to the N-H stretching in the composite[196].

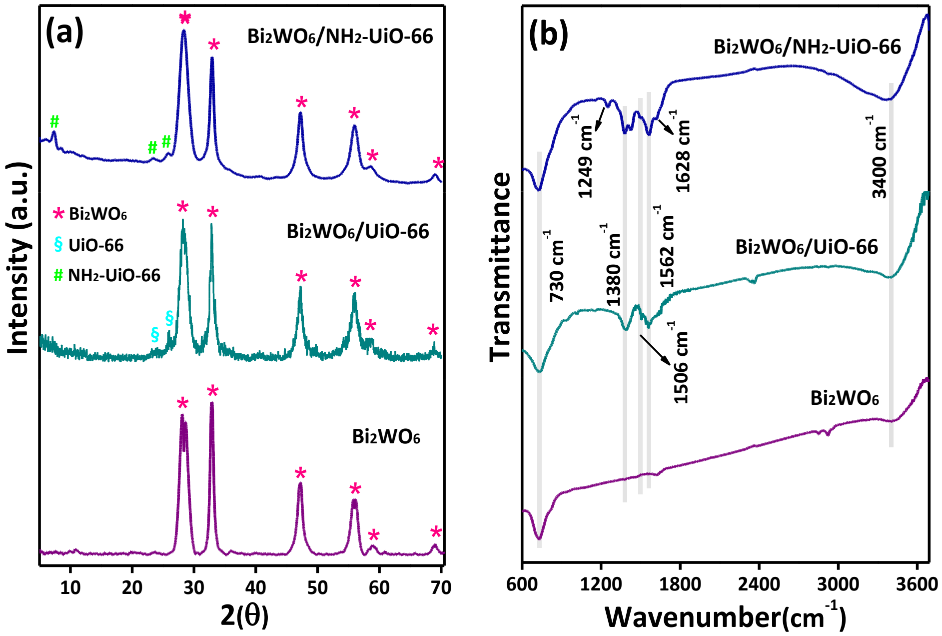

Figure 6.2. (a) X-ray diffraction and (b) FTIR spectra of spectra of bare-Bi_2WO_6, Bi_2WO_6/UiO-66 and Bi_2WO_6/NH_2-UiO-66 composites.

6.3.3 Morphology and surface analysis

The morphology and structure of bare-Bi_2WO_6, Bi_2WO_6/UiO-66 and Bi_2WO_6/NH_2-UiO-66 composites were analysed using scanning electron microscopy (SEM) and transmission electron microscopy (TEM) as shown in **Figure 6.3(a-i)**. The developed bare-Bi_2WO_6 exhibited flower like morphology, which could be due to assembly of small nanoflakes into micro/nanoflower with a diameter of around 4 to 5 μm (**Figure 6.3(a-c)**)[191, 208]. The morphology of Bi_2WO_6/UiO-66 and Bi_2WO_6/NH_2-UiO-66 composites were significantly altered over the integration of UiO-66 and NH_2-UiO-66 onto the Bi_2WO_6 surface, which considerably influenced the nano/micro flower surface as shown in **Figure 6.3(e)&(h)**. Further, SEM results revealed that the UiO-66 and NH_2-UiO-66 particles are aggregated with Bi_2WO_6 micro/nanoflower. However, as compared to UiO-66, the NH_2-UiO-66 significantly altered the morphology of the composite. This could be attributed to the -NH_2 functional group, which possibly established a potential binding of NH_2-UiO-66 on Bi_2WO_6 micro/nanoflower surface. Therefore, the increased amount of NH_2-UiO-66 on Bi_2WO_6 surface strongly covered the microflower surface and transformed microflower as microparticle[196, 201, 209]. Both the SEM and TEM images confirmed that the NH_2-UiO-66 and Bi_2WO_6 are closely connected, which can be corroborated with the XRD and FTIR analysis as well. Further, the elemental composition of the materials was confirmed by energy dispersive X-ray spectroscopy (EDS) as shown in **Figure S6.1**(supporting information). The elements such as Zr, C and N were detected in EDS spectrum of Bi_2WO_6/NH_2-UiO-66, which confirmed the presence of NH_2-UiO-66 in the composite[210]. The specific surface area of the bare-Bi_2WO_6, Bi_2WO_6/UiO-66 and Bi_2WO_6/NH_2-UiO-66 composites was measured using Brunauer-Emmett-Teller (BET) analysis using nitrogen (N_2) adsorption-desorption measurement is displayed in **Figure 6.3(j)**. The estimated surface area of Bi_2WO_6, Bi_2WO_6/UiO-66 and Bi_2WO_6/NH_2-UiO-66 was around 47.9, 83.7 and 113.6 m^2/g, respectively. It is clear that the incorporation of UiO-66 and NH_2-UiO-66 has significantly improved the overall specific surface area of the Bi_2WO_6/UiO-66 and Bi_2WO_6/NH_2-UiO-66 composites and the observed increased surface area of Bi_2WO_6/NH_2-UiO-66 could be attributed to the -NH_2 groups which established a stronger and stable integration of NH_2-UiO-66 onto the surface of Bi_2WO_6, which also increased the quantity of NH_2-UiO-66 onto the micro/nanoflower surface as well. Moreover, the absence of amine linker in UiO-66 could possibly establish only the electrostatic interaction between UiO-66 and Bi_2WO_6 and thereby the overall surface area is reduced for Bi_2WO_6/UiO-66 composite as compared to the other composite. Notably, the improved specific surface area can favor the generation of more active species and offer enhanced adsorption of more antibiotic molecules, and thereby it can contribute to the higher photocatalytic performance[201, 211].

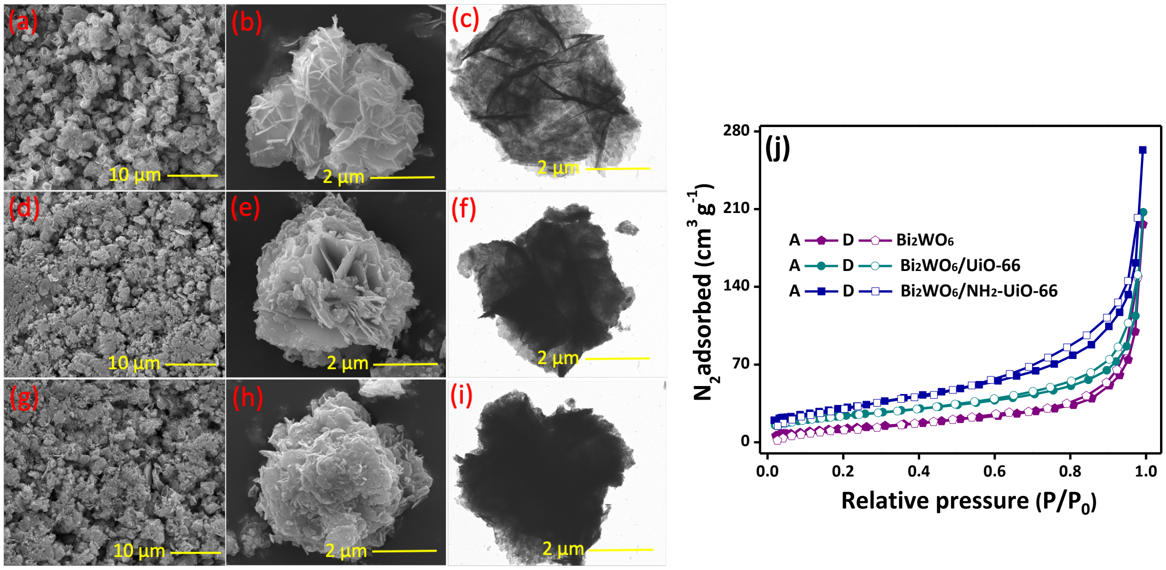

Figure 6.3. SEM and TEM image of (a-c) bare-Bi_2WO_6, (d-f) Bi_2WO_6/UiO-66, (g-i) Bi_2WO_6/NH_2-UiO-66 composites, and (j) Nitrogen adsorption-desorption isotherm of bare-Bi_2WO_6, Bi_2WO_6/UiO-66 and Bi_2WO_6/NH_2-UiO-66 composites.

6.3.4 Photoinduced charge separation and transfer characteristics

The photogenerated charge separation efficiency of the bare-Bi_2WO_6, Bi_2WO_6/UiO-66 and Bi_2WO_6/NH_2-UiO-66 composites studied using the photoluminescence (PL) analysis and the corresponding results are displayed in **Figure 6.4(a)**. As compared to the bare-Bi_2WO_6, the composites Bi_2WO_6/UiO-66 and Bi_2WO_6/NH_2-UiO-66 showed reduced PL emission intensity, which indicated that the composites possess lower recombination resistance and higher photoinduced electron-hole separation in the system. This could be attributed to the formation of heterojunction between the Bi_2WO_6 and UiO-66/NH_2-UiO-66 resulting the favorable band structure for the improved the separation and transfer of photo-generated charge carriers within the composites as well as to the reactant molecules. Further, as revealed by the SEM and TEM images, the UiO-66/NH_2-UiO-66 has been strongly incorporated onto the Bi_2WO_6 micro/nanoflower and greatly facilitates for the stronger interfacial contact between Bi_2WO_6 and NH_2-UiO-66 and thus the composite possesses an improved photo-generated charge carrier transfer rate through the formation of heterojunctions. Moreover, the Bi_2WO_6/NH_2-UiO-66 composite showed relatively enhanced charge separation and migration, which could be attributed to the amine functional group establishing a strong interface contact between Bi_2WO_6 and NH_2-UiO-66 heterostructures[197, 209, 210]. Further, the photogenerated charge carrier separation and transfer efficiencies of the materials were measured by photoelectrochemical (PEC) technique. The photocurrent generation in the bare-Bi_2WO_6, Bi_2WO_6/UiO-66 and Bi_2WO_6/NH_2-UiO-66 composite was estimated by chronoamperometry technique with light "on-off" process under solar light irradiation (**Figure 6.4(b)**). The developed materials showed good photocurrent generation, and the intensity of photocurrent was increased during light irradiation and decreased to zero when light irradiation was turned off. On comparison, the Bi_2WO_6/NH_2-UiO-66 composite showed higher photocurrent generation efficiency and high photocurrent density of around 1.42 $\mu A/cm^2$. The enhanced photocurrent generation could be attributed to the amine linker resulting in an efficient photocurrent conduction via the formed heterojunction along with strong interface connection between Bi_2WO_6 and NH_2-UiO-66[210, 212]. In addition, the Nyquist plot was obtained to analyze charge transfer efficiency in the system using electrochemical impedance technique and the corresponding results are displayed in **Figure 6.4(c)**. The obtained results showed that the Bi_2WO_6/NH_2-UiO-66 composite exhibited smaller arc radius that indicated the smaller charge transfer resistance in the system as compared to that of the Bi_2WO_6/UiO-66 and bare-Bi_2WO_6 materials. The lower resistance of Bi_2WO_6/NH_2-UiO-66 could be attributed to the establishment of conducting channels to facilitate the migration of photo-generated electrons from Bi_2WO_6 and NH_2-UiO-66 via Bi-W-O-N-C-O-Zr network in the system. This eventually lowered the interface resistivity and increased the fast charge transfer efficiency, along with offering a better photo-stability to the composite[199, 211].

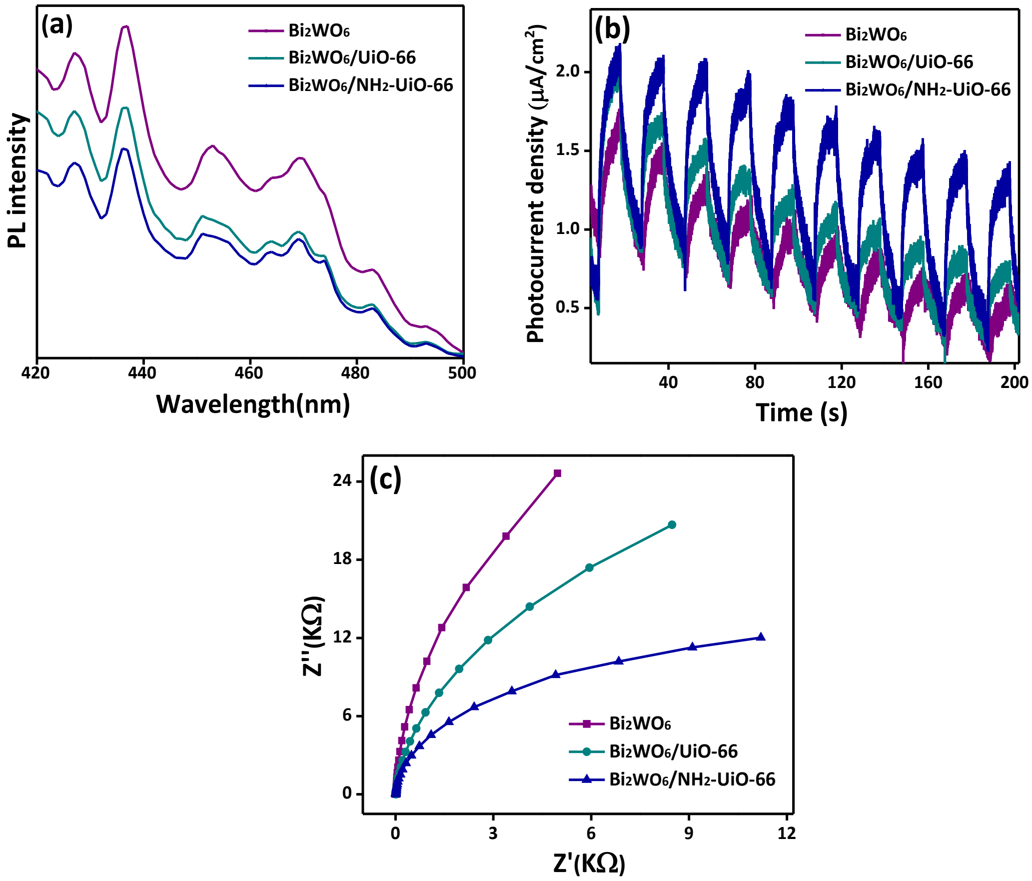

Figure 6.4. (a) Photoluminescence, (b) Chronoamperometric and (c) Nyquist plots of bare-Bi_2WO_6, Bi_2WO_6/UiO-66 and Bi_2WO_6/NH_2-UiO-66 composites.

6.3.5 Photocatalytic activity

The photocatalytic performances of the bare-Bi_2WO_6, Bi_2WO_6/UiO-66 and Bi_2WO_6/NH_2-UiO-66 composites were studied for the degradation of antibiotic ciprofloxacin (CIP) under solar light irradiation and the obtained degradation results are shown in **Figure 6.5(a)**. The time dependent optical degradation spectra of ciprofloxacin over Bi_2WO_6, Bi_2WO_6/UiO-66 and Bi_2WO_6/NH_2-UiO-66 are given in **Figure S6.2(a-c)** in the supporting information. The materials showed photocatalytic activity on ciprofloxacin degradation in the order of Bi_2WO_6/NH_2-UiO-66 > Bi_2WO_6/UiO-66 > Bi_2WO_6, with degradation percentage of 83.1, 57.7 and 34.6%, respectively at the end of 60 min. On comparison, the Bi_2WO_6/NH_2-UiO-66 composite revealed the higher photocatalytic activity, and it found be around 2.4 and 1.45 folds higher than Bi_2WO_6 and Bi_2WO_6/UiO-66, respectively. The superior photocatalytic performance of Bi_2WO_6/NH_2-UiO-66 can be readily attributed to the improved photoinduced rate of charge carrier separation and transfer due to the formation of heterojunction via amine linkage. In addition, the extended photo-absorbance offered higher solar light absorption and specific surface area provided a large number of reactive sites to the Bi_2WO_6/NH_2-UiO-66 composites, which contributed in improving the overall photocatalytic properties of the system. Further, in order to know the key radical species responsible for the photocatalytic activity in Bi_2WO_6/NH_2-UiO-66 composites, the scavenging experiment using different scavenging agents such as triethanolamine (TEOA), isopropyl alcohol (IPA) and p-benzoquinone (BQ) corresponding to h^+, $OH^{\bullet}$ and $O_2^{\bullet-}$ species was carried out and the obtained results are displayed in **Figure 6.5(b)**. The result showed that the degradation efficiency was dropped to 28.4, 72.5 and 43.5% in presence of TEOA, IPA and BQ, respectively, whereas without scavenger the ciprofloxacin degradation was 83.1%. Therefore, it is confirmed that the holes (h^+) and superoxide radical ($O_2^{\bullet-}$) are the main active species involved in the photocatalytic ciprofloxacin degradation process rather than the $OH^{\bullet}$ radicals[170, 213]. The band structure of the photocatalysts is a key factor in determining the photocatalytic redox potential as well as photocatalytic efficiency of the heterojunction composites. Therefore, the band positions of Bi_2WO_6 (+2.69 eV VB and -0.02 eV CB) and NH_2-UiO-66 (+2.30 eV VB and -0.35 eV CB) were estimated using the Mott-Schottky plot[214, 215] and Tauc plot[186, 215] analysis and the corresponding results are given in **Figure S6.3(a-b)** and **Figure S6.4(a-b)**, respectively in the supporting information. Further, the schematic illustration as shown in **Figure 6.5(c)** represents the photocatalytic charge mechanism in Bi_2WO_6/NH_2-UiO-66 composite towards the degradation of ciprofloxacin. It can be seen that the photo-generated electrons undergo migration from the CB of Bi_2WO_6 to the VB of UiO-66-NH_2 and then excited to the CB of UiO-66-NH_2 under solar light irradiation. Based on the band structure, the VB potential of Bi_2WO_6 (+2.69 eV) could be enough to generate hydroxyl radical ($OH^{\bullet}/OH^-$ = 1.99 eV), but CB of Bi_2WO_6 (-0.02 eV) may not be enough to generate super oxide radical ($O_2/ O_2^{\bullet-}$ = -0.33 eV). Similarly, the VB (+2.30 eV) and CB (-0.35 eV) potential of NH_2-UiO-66 both are suitable to generate hydroxyl radical ($OH^{\bullet}/OH^-$ = 1.99 eV) and super oxide radical ($O_2/ O_2^{\bullet-}$ = -0.33 eV). However, the Bi_2WO_6/NH_2-UiO-66 heterojunction composite led to the Z-scheme charge transfer mechanism with strong redox property, and it can establish the strong oxidation ability at the valence band (VB) of Bi_2WO_6 and high reduction ability at the conduction band (CB) of NH_2-UiO-66. Therefore, the generated holes at the VB of Bi_2WO_6 spontaneously undergo a direct oxidation of ciprofloxacin, and/or oxidize the water molecules, and thereby the generated hydroxyl radicals involved in the oxidation mediated degradation of ciprofloxacin. On other hand, the electrons at CB of NH_2-UiO-66 reduce the oxygen molecule and produce super oxide radicals and thereby it involves in ciprofloxacin degradation. Hence, the integration of NH_2-UiO-66 with Bi_2WO_6 established Z-scheme heterojunction with efficient charge separation and high redox properties, which potentially led to the efficient degradation of ciprofloxacin molecules[216-218].

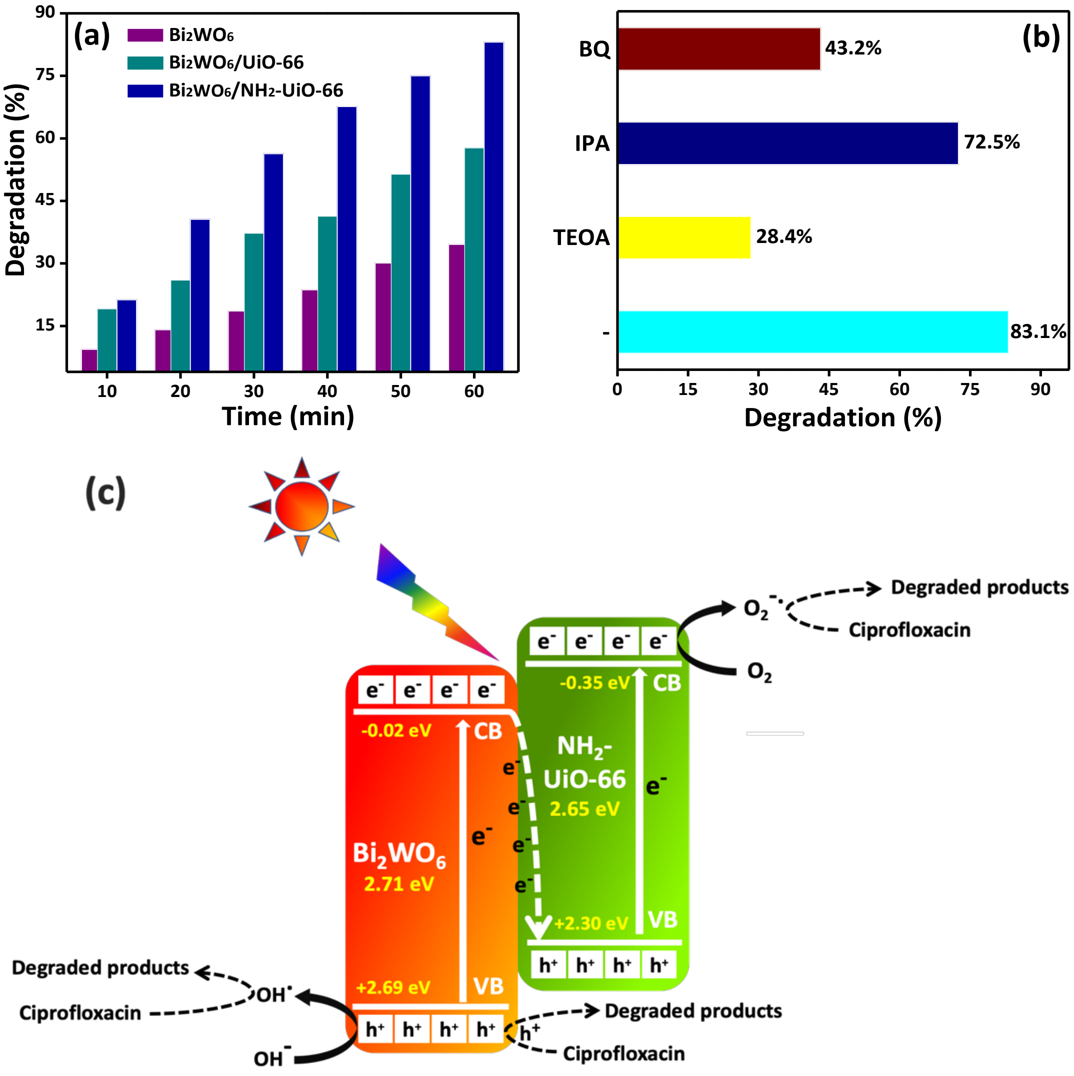

Figure 6.5. (a) Photocatalytic degradation of antibiotic ciprofloxacin by bare-Bi_2WO_6, Bi_2WO_6/UiO-66 and Bi_2WO_6/NH_2-UiO-66 composites under solar light irradiation (b) Radicals scavenger test over Bi_2WO_6/NH_2-UiO-66 and (c) Proposed photocatalytic degradation mechanism of Bi_2WO_6/NH_2-UiO-66.

Further, the stability of the photocatalyst was studied by conducing the reusability study for up to five cycles using the Bi_2WO_6/UiO-66 and Bi_2WO_6/NH_2-UiO-66 photocatalysts under the same experiment condition, and the obtained results are given in **Figure S6.5(a-b)**. The obtained results revealed both the composites showed better stability and consistency towards the photocatalytic degradation of CIP molecules. However, the Bi_2WO_6/NH_2-UiO-66 showed relatively higher recyclability even five cycles as compared to that of the Bi_2WO_6/UiO-66, and it could be mainly attributed to their strong interface contact and stabilized structural properties established by the amine functionalized UiO-66 MOFs[196, 215].

6.4. Conclusion

In this study, the development of Bi_2WO_6/NH_2-UiO-66 nanocomposite by anchoring NH_2-UiO-66 on Bi_2WO_6 micro/nanoflower surface and their enhanced photocatalytic activity towards degradation of antibiotic-ciprofloxacin molecules under solar light irradiation has been demonstrated. The improved photocatalytic activity of Bi_2WO_6/NH_2-UiO-66 composite was attributed to the formation of heterojunction with strong interface contact between Bi_2WO_6 and NH_2-UiO-66 via Bi-W-O-N-C-O-Zr network, which favored in broadening the spectral response range, reduced photogenerated electron-hole pair recombination, and faster photogenerated charge carrier transfer in the system. Also, the heterojunction formation with Z-scheme mechanism and high surface reactive sites offered strong oxidative and reduction properties to Bi_2WO_6/NH_2-UiO-66 composite. Further, the strong interfacial interaction between NH_2-UiO-66 and Bi_2WO_6 established by amine groups provided a better stability to the Bi_2WO_6/NH_2-UiO-66 composite.

Acknowledgements

This work was supported by the Natural Science and Engineering Research Council of Canada (NSERC) through the Strategic Project (SP), and Discovery Grants. The authors would like to thank Exp Inc. and SiliCycle Inc. for their support.

6.5. Supporting information

6.5.1. Elemental composition

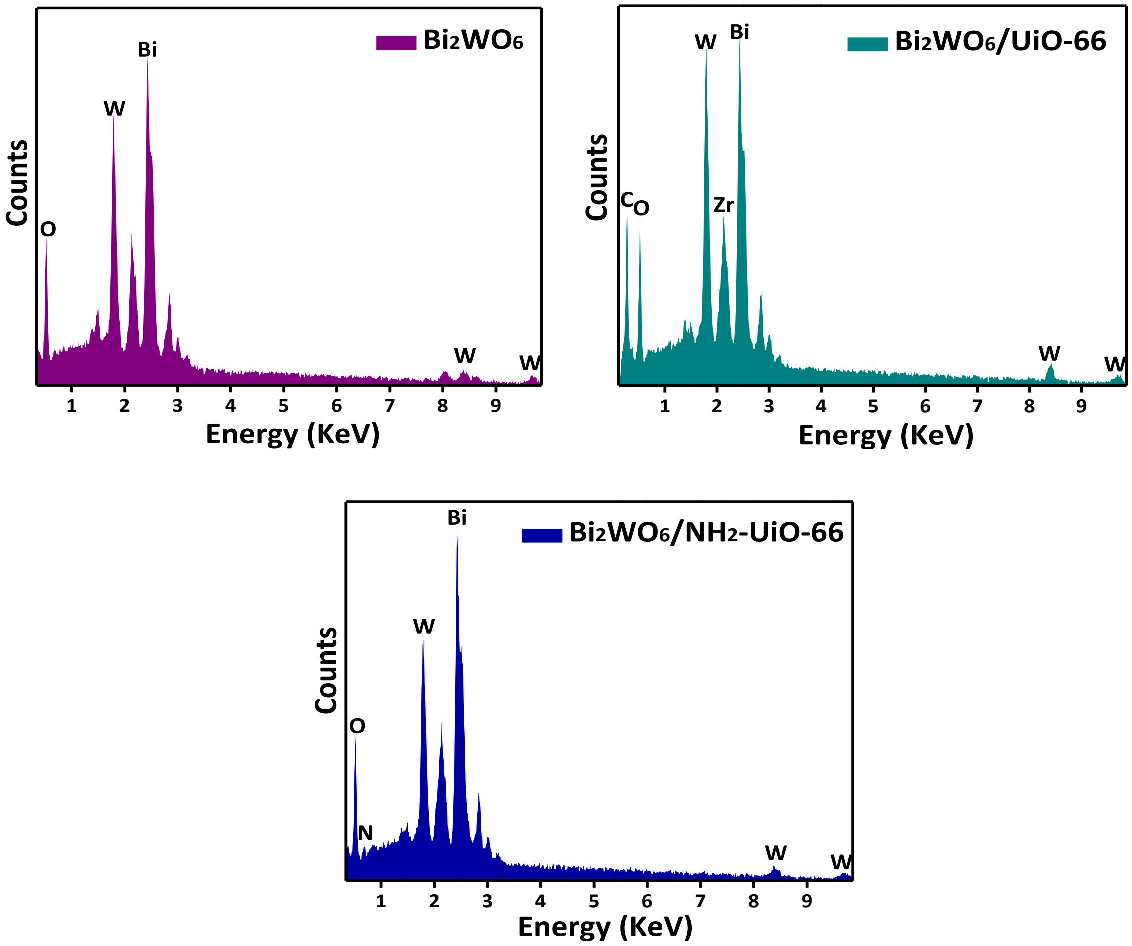

Figure S6.1. EDS spectra of bare-Bi_2WO_6, Bi_2WO_6/UiO-66 and Bi_2WO_6/NH_2-UiO-66 composites.

6.5.2. Photocatalytic degradation of ciprofloxacin

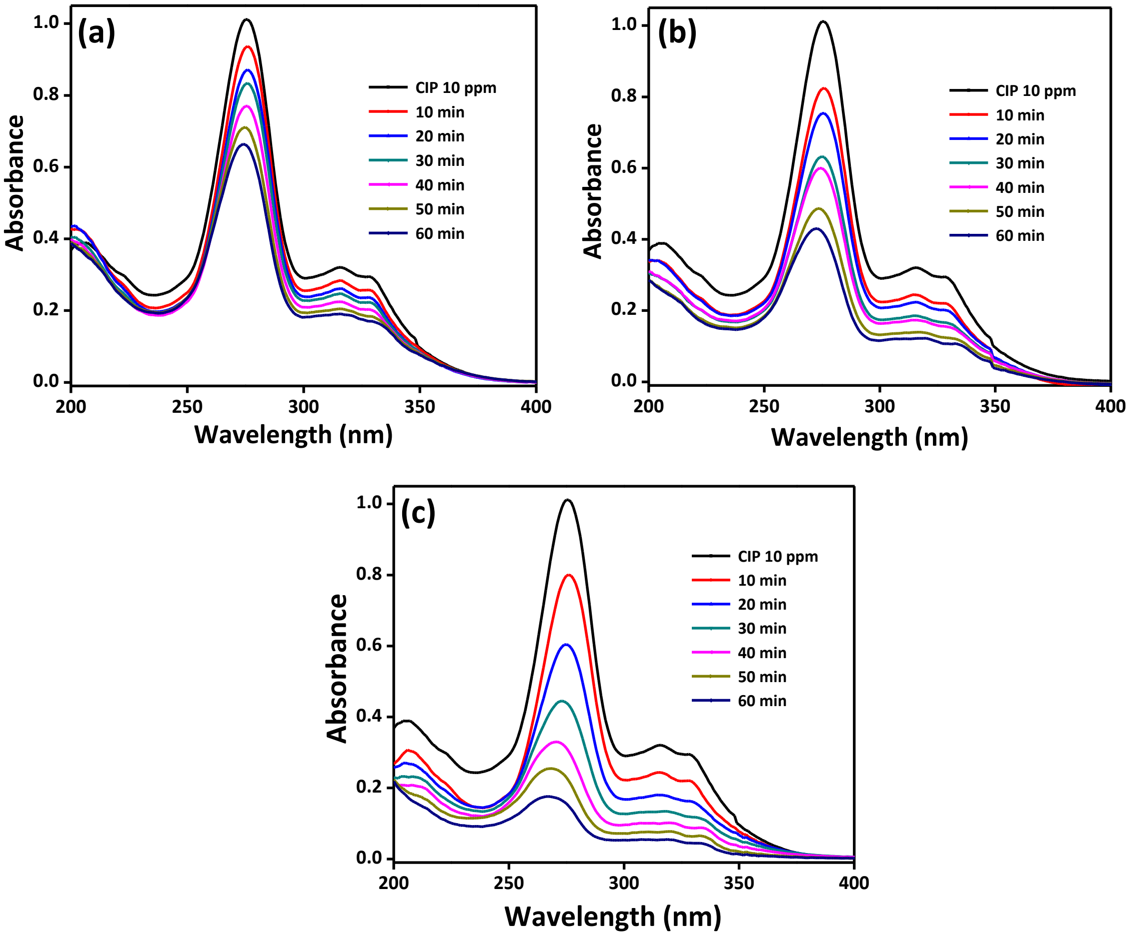

Figure S6.2. UV-vis absorbance spectra of degradation of ciprofloxacin in presence of (a) bare-Bi_2WO_6, (b) Bi_2WO_6/UiO-66 and (c) Bi_2WO_6/NH_2-UiO-66 composites.

6.5.3. Mott-Schottky

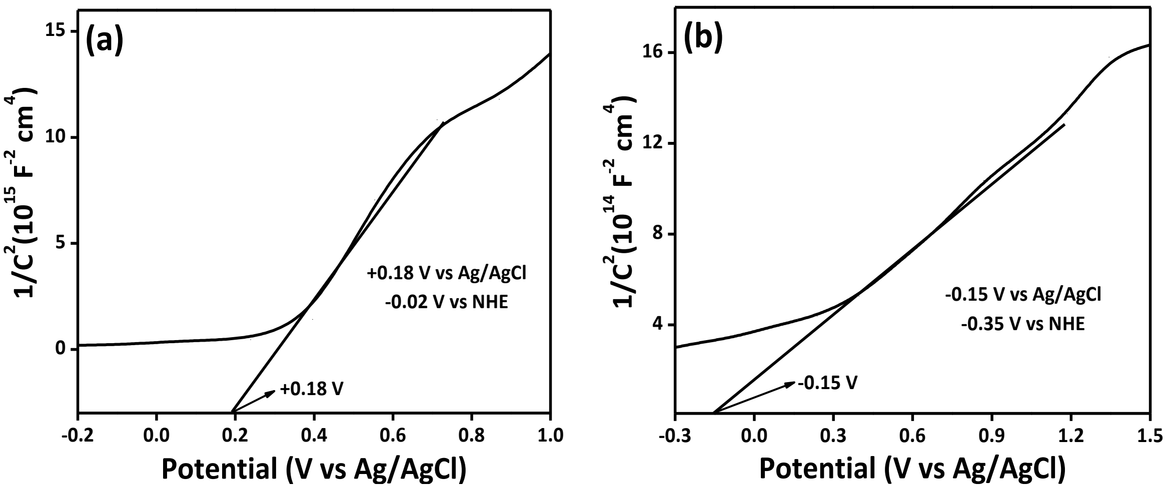

Figure S6.3. Mott-Schottky plot of (a) Bi_2WO_6 and (b) NH_2-UiO-66.

6.5.4. Tauc plot

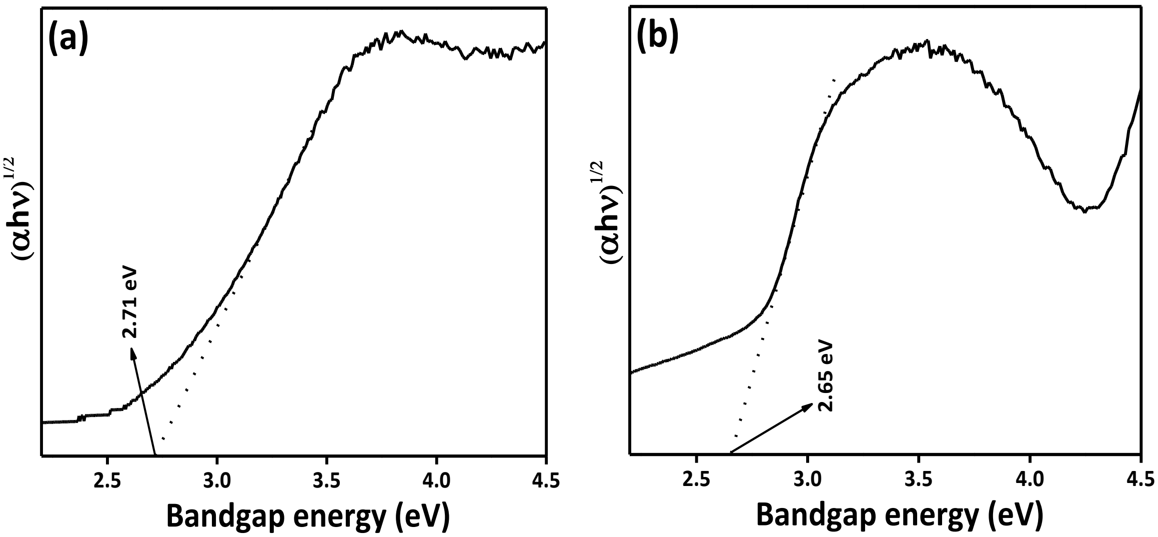

Figure S6.4. Tauc plot of (a) Bi_2WO_6 and (b) NH_2-UiO-66.

6.5.5. Reusability study

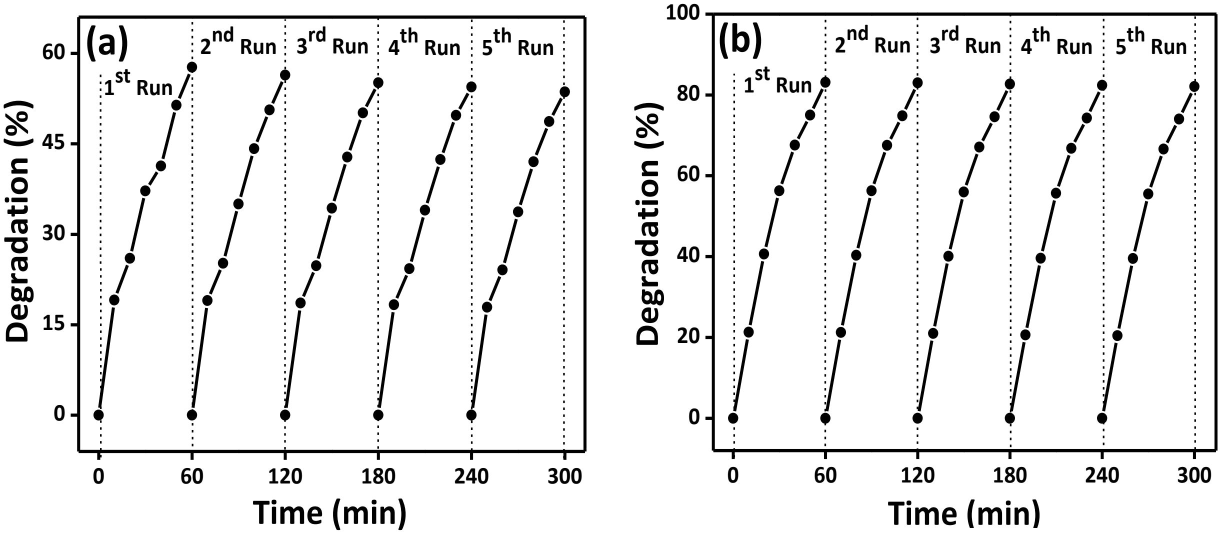

Figure S6.5. Reusability study of (a) Bi_2WO_6/UiO-66 and (b) Bi_2WO_6/NH_2-UiO-66 composites.

Conclusion and future work

7.1 General conclusion

Photocatalysis is a promising solution to address rising concerns and paves path for the complete degradation of emerging antibiotic pollutants under solar light irradiation. In particular, the design of nanostructured and nanocomposite photocatalysts has been found to exhibit higher antibiotic degradation performance due to their distinct characteristic properties such as superior structural, surface and interfacial properties. These features yielded improved photoabsorbance, charge separation, charge transfer, redox properties and photostability of the material. Our strategies comprise construction of nanostructured materials and integration/coupling of other materials to develop hybrid nanocomposites. As a result, we recently developed $CaBiO_3$, $BiVO_4$-APS-C_{60} and Bi_2WO_6/NH_2-UiO-66 nanostructured hybrid photocatalyst towards the degradation of antibiotic pollutants in water. The overall goal of this thesis was to develop ideal strategies for the development of efficient photocatalysts towards antibiotic pollutants.

The development of new ferroelectric perovskite material $CaBiO_3$ with distinct Bi^{3+} and Bi^{5+} multi-charge disproportion was potentially explored on degradation of ciprofloxacin and tetracycline antibiotic under solar light. The Bi^{3+}/Bi^{5+} charge disproportion and well-organized crystal arrangement of $CaBiO_3$ resulted in an efficient visible photo-absorbance and higher photo-generated charge carrier generation and separation. The incorporation of Ca^{2+} into BiO_6 crystal lattices potentially altered the band structure of $CaBiO_3$ system, and the established band energy potentials were found more suitable for photocatalytic redox reactions. Thus, the developed $CaBiO_3$ materials exhibited nanostructure with higher surface area which provided enhanced surface properties for catalytic reaction.

An efficient $BiVO_4$-APS-C_{60} composite was developed by integrating the aminosilicate-functionalized-C_{60} QDs on the surface of ultrathin $BiVO_4$ nanolayers, and it showed efficient photocatalytic activity towards ciprofloxacin degradation under solar light. The fine dispersion of aminosilicate functionalized-QDs considerably decreased inter-layer thickness and aggregation in $BiVO_4$ layers, and it barely influenced photo-absorption properties of the composite. Besides, the aminosilicate established a strong interfacial interaction between C_{60}

and $BiVO_4$ via the Bi-V-O-Si-C network, which provided a remarkable charge transfer efficiency and stability for the $BiVO_4$-APS-C_{60} composite.

The development of Bi_2WO_6/NH_2-UiO-66 nanocomposite exhibited superior photocatalytic activity for ciprofloxacin degradation under solar light irradiation. The enhanced photocatalytic performance was attributed to the extended photoabsorbance, reduced charge recombination, and faster charge transfer due to the formation of Bi_2WO_6/NH_2-UiO-66 heterojunction with strong interface contact. The heterojunction formation with Z-scheme charge transfer mechanism and high surface reactive sites offered strong redox properties to Bi_2WO_6/NH_2-UiO-66 composite. Besides, the amine linkage established a strong interfacial interaction between NH_2-UiO-66 and Bi_2WO_6, which provided better stability to the Bi_2WO_6/NH_2-UiO-66 composite.

7.2 Future outlook

Photocatalysis involves solar energy assisted active free radicals' generation and it accomplishes the potential degradation of the emerging pharmaceutical pollutants. The semiconductor photocatalyst mainly determines the efficiency of the photocatalytic process. In the past few decades, a wide range of materials were developed and explored for potential application in antibiotic degradation. However, the development of nanostructured hybrid photocatalysts revealed superior catalytic properties which offers extended photoabsorbance, large surface area, more active sites and enhanced photoinduced charge separation and mobility. Therefore, we propose to develop the following new nanostructured and nanocomposite materials as potential photocatalytic material towards the degradation of the pharmaceutical pollutants in presence of solar light.

$MBiO_3$ (M = Cd, Mg and Zn) materials: The design of $MBiO_3$ photocatalytic materials such as $CdBiO_3$, $MgBiO_3$ and $ZnBiO_3$ also provides effective Bi^{3+}/Bi^{5+} charge disproportionation and well-organized BiO_6 octahedral crystal arrangement, which should result in high photo-generated charge carrier separation and efficient visible photo-absorbance to $MBiO_3$ system. The effective Cd^{2+}, Mg^{2+} and Zn^{2+} metal ion incorporation into bismuthate (BiO_6) crystal lattices could potentially alter the band structure of $MBiO_3$ and could establish strong redox property to photocatalytic antibiotic degradation.

Black metal oxides: The development of black metal oxides such as black titanium dioxide (TiO_{2-x}), black $BiVO_4$ and tungstic oxide (WO_{3-x}) offers moderate oxygen vacancies and increase the donor concentration, which ultimately favors the efficient charge separation and transport. Further, their lower valence band helps in achieving a narrow band gap and broadened photo-absorption range. Therefore, black metal oxides tend to show an enhanced solar energy utilization and high charge carrier migration for photocatalytic antibiotic removal.

Bismuth composites: The bismuth-based $BiVO_4$, Bi_2WO_6, Bi_2MoO_6 and BiOX (X= Cl, Br and I) ultrathin materials designs have received great interest in photocatalysis due to their unique structure and surface properties, which give interesting visible light absorption, good charge separation and high surface reactive site. The designing of bismuth-based composites with metals, semiconductors, carbon materials and metal-organic frameworks could potentially improve the photophysical, structural and surface properties towards photocatalytic degradation of antibiotics.

Photocatalytic antibiotic degradation: Achieve a complete mineralization of antibiotics and study their degradation pathways and mechanism. Further, to extend the developed materials towards the degradation of other antibiotic pollutants such as cefuroxime, amoxicillin, sulfamethoxazole, chloramphenicol etc., from water and modify the developed materials towards simultaneous degradation of multiple pharmaceutical pollutants.

References

[1] A. Pal, K.Y.-H. Gin, A.Y.-C. Lin, M. Reinhard, Impacts of emerging organic contaminants on freshwater resources: review of recent occurrences, sources, fate and effects, Science of the total environment, 408 (2010) 6062-6069.

[2] A. Küster, N. Adler, Pharmaceuticals in the environment: scientific evidence of risks and its regulation, Philosophical Transactions of the Royal Society B: Biological Sciences, 369 (2014) 20130587.

[3] T. aus der Beek, F.A. Weber, A. Bergmann, S. Hickmann, I. Ebert, A. Hein, A. Küster, Pharmaceuticals in the environment-global occurrences and perspectives, Environmental toxicology and chemistry, 35 (2016) 823-835.

[4] S.K. Khetan, T.J. Collins, Human pharmaceuticals in the aquatic environment: a challenge to green chemistry, Chemical reviews, 107 (2007) 2319-2364.

[5] M. Patel, R. Kumar, K. Kishor, T. Mlsna, C.U. Pittman Jr, D. Mohan, Pharmaceuticals of emerging concern in aquatic systems: chemistry, occurrence, effects, and removal methods, Chemical reviews, 119 (2019) 3510-3673.

[6] A.S. Oberoi, Y. Jia, H. Zhang, S.K. Khanal, H. Lu, Insights into the fate and removal of antibiotics in engineered biological treatment systems: a critical review, Environmental Science & Technology, 53 (2019) 7234-7264.

[7] J.L. Martínez, Antibiotics and antibiotic resistance genes in natural environments, Science, 321 (2008) 365-367.

[8] M.E. de Kraker, A.J. Stewardson, S. Harbarth, Will 10 million people die a year due to antimicrobial resistance by 2050?, PLoS medicine, 13 (2016).

[9] V. Homem, L. Santos, Degradation and removal methods of antibiotics from aqueous matrices-a review, Journal of environmental management, 92 (2011) 2304-2347.

[10] C. Gadipelly, A. Pérez-González, G.D. Yadav, I. Ortiz, R. Ibáñez, V.K. Rathod, K.V. Marathe, Pharmaceutical industry wastewater: review of the technologies for water treatment and reuse, Industrial & Engineering Chemistry Research, 53 (2014) 11571-11592.

[11] M.J. Calvete, G. Piccirillo, C.S. Vinagreiro, M.M. Pereira, Hybrid materials for heterogeneous photocatalytic degradation of antibiotics, Coordination Chemistry Reviews, 395 (2019) 63-85.

[12] D. Li, W. Shi, Recent developments in visible-light photocatalytic degradation of antibiotics, Chinese Journal of Catalysis, 37 (2016) 792-799.

[13] K. Rokesh, M. Sakar, T.-O. Do, Calcium bismuthate ($CaBiO_3$): a potential sunlight-driven perovskite photocatalyst for the degradation of emerging pharmaceutical contaminants, ChemPhotoChem, 4 (2020) 373-380.

[14] C.-C. Nguyen, D.T. Nguyen, T.-O. Do, A novel route to synthesize C/Pt/TiO_2 phase tunable anatase-rutile TiO_2 for efficient sunlight-driven photocatalytic applications, Applied Catalysis B: Environmental, 226 (2018) 46-52.

[15] S. Bagheri, A. TermehYousefi, T.-O. Do, Photocatalytic pathway toward degradation of environmental pharmaceutical pollutants: structure, kinetics and mechanism approach, Catalysis Science & Technology, 7 (2017) 4548-4569.

[16] C.C. Nguyen, N.N. Vu, S. Chabot, S. Kaliaguine, T.O. Do, Role of CxNy-triazine in photocatalysis for efficient hydrogen generation and organic pollutant degradation under solar light irradiation, Solar RRL, 1 (2017) 1700012.

[17] S. Banerjee, S.C. Pillai, P. Falaras, K.E. O'shea, J.A. Byrne, D.D. Dionysiou, New insights into the mechanism of visible light photocatalysis, The journal of physical chemistry letters, 5 (2014) 2543-2554.

[18] T.-O. Do, S. Mohan, Special Issue on "emerging trends in TiO_2 photocatalysis and applications", Multidisciplinary Digital Publishing Institute, 2020.

[19] M. Sakar, C.-C. Nguyen, M.-H. Vu, T.-O. Do, Materials and mechanisms of photo-assisted chemical reactions under light and dark conditions: can day-night photocatalysis be achieved?, ChemSusChem, 11 (2018) 809-820.

[20] S. Sarkar, R. Das, H. Choi, C. Bhattacharjee, Involvement of process parameters and various modes of application of TiO_2 nanoparticles in heterogeneous photocatalysis of pharmaceutical wastes-a short review, RSC advances, 4 (2014) 57250-57266.

[21] C.C. Nguyen, N.N. Vu, T.-O. Do, Recent advances in the development of sunlight-driven hollow structure photocatalysts and their applications, Journal of Materials Chemistry A, 3 (2015) 18345-18359.

[22] M. Sakar, R. Mithun Prakash, T.-O. Do, Insights into the TiO_2-based photocatalytic systems and their mechanisms, Catalysts, 9 (2019) 680.

[23] M.R. Hoffmann, S.T. Martin, W. Choi, D.W. Bahnemann, Environmental applications of semiconductor photocatalysis, Chemical reviews, 95 (1995) 69-96.

[24] M. Sakar, S. Balakumar, P. Saravanan, S. Bharathkumar, Particulates vs. fibers: dimension featured magnetic and visible light driven photocatalytic properties of Sc modified multiferroic bismuth ferrite nanostructures, Nanoscale, 8 (2016) 1147-1160.

[25] M. Mokhtarifar, D.-T. Nguyen, M.V. Diamanti, R. Kaveh, M. Asa, S. Mohan, M. Pedeferri, T.-O. Do, Fabrication of dual-phase TiO_2/WO_3 with post-illumination photocatalytic memory, New Journal of Chemistry, (2020).

[26] C.-C. Nguyen, C.-T. Dinh, T.-O. Do, Hollow Sr/Rh-codoped TiO_2 photocatalyst for efficient sunlight-driven organic compound degradation, RSC Advances, 7 (2017) 3480-3487.

[27] H. Tong, S. Ouyang, Y. Bi, N. Umezawa, M. Oshikiri, J. Ye, Nano-photocatalytic materials: possibilities and challenges, Advanced materials, 24 (2012) 229-251.

[28] Y. Gan, Y. Wei, J. Xiong, G. Cheng, Impact of post-processing modes of precursor on adsorption and photocatalytic capability of mesoporous TiO_2 nanocrystallite aggregates towards ciprofloxacin removal, Chemical Engineering Journal, 349 (2018) 1-16.

[29] J. Xiong, W. Li, Y. Gan, Y. Wei, G. Cheng, S. Dou, Z. Li, Extremely rapid engineering of zinc oxide nanoaggregates with structure-dependent catalytic capability towards removal of ciprofloxacin antibiotic, Inorganic Chemistry Frontiers, 5 (2018) 2432-2444.

[30] J. Liu, G. Zhang, C.Y. Jimmy, Y. Guo, In situ synthesis of Zn_2GeO_4 hollow spheres and their enhanced photocatalytic activity for the degradation of antibiotic metronidazole, Dalton Transactions, 42 (2013) 5092-5099.

[31] J. Di, J. Xiong, H. Li, Z. Liu, Ultrathin 2D photocatalysts: electronic-structure tailoring, hybridization, and applications, Advanced materials, 30 (2018) 1704548.

[32] Y. Sun, S. Gao, F. Lei, C. Xiao, Y. Xie, Ultrathin two-dimensional inorganic materials: new opportunities for solid state nanochemistry, Accounts of chemical research, 48 (2015) 3-12.

[33] X. Jiao, K. Zheng, L. Liang, X. Li, Y. Sun, Y. Xie, Fundamentals and challenges of ultrathin 2D photocatalysts in boosting CO_2 photoreduction, Chemical Society Reviews, 49 (2020) 6592-6604.

[34] H. Wang, X. Zhang, Y. Xie, Recent progress in ultrathin two-dimensional semiconductors for photocatalysis, Materials Science and Engineering: R: Reports, 130 (2018) 1-39.

[35] S. Qamar, F. Lei, L. Liang, S. Gao, K. Liu, Y. Sun, W. Ni, Y. Xie, Ultrathin TiO_2 flakes optimizing solar light driven CO_2 reduction, Nano Energy, 26 (2016) 692-698.

[36] S. Sun, W. Wang, L. Zhang, E. Gao, D. Jiang, Y. Sun, Y. Xie, Ultrathin {001}-oriented bismuth tungsten oxide nanosheets as highly efficient photocatalysts, ChemSusChem, 6 (2013) 1873-1877.

[37] C.-C. Nguyen, N.-N. Vu, T.-O. Do, Efficient hollow double-shell photocatalysts for the degradation of organic pollutants under visible light and in darkness, Journal of Materials Chemistry A, 4 (2016) 4413-4419.

[38] D.-T. Nguyen, C.-C. Nguyen, M. St-Jean, S.p. Chabot, S. Kaliaguine, T.-O. Do, All in one: contributions of Ni dopants and Ni/NiS dual cocatalysts to the enhanced efficiency of TiO_2 photocatalyst for the degradation of organic pollutants, ACS Applied Nano Materials, 1 (2018) 6864-6873.

[39] C.-T. Dinh, T.-D. Nguyen, F. Kleitz, T.-O. Do, A new route to size and population control of silver clusters on colloidal TiO_2 nanocrystals, ACS applied materials & interfaces, 3 (2011) 2228-2234.

[40] F. Wang, Q. Li, D. Xu, Recent progress in semiconductor-based nanocomposite photocatalysts for solar-to-chemical energy conversion, Advanced Energy Materials, 7 (2017) 1700529.

[41] C. Xu, P.R. Anusuyadevi, C. Aymonier, R. Luque, S. Marre, Nanostructured materials for photocatalysis, Chemical Society Reviews, 48 (2019) 3868-3902.

[42] M. Sakar, S. Balakumar, Reverse Ostwald ripening process induced dispersion of Cu_2O nanoparticles in silver-matrix and their interfacial mechanism mediated sunlight driven photocatalytic properties, Journal of Photochemistry and Photobiology A: Chemistry, 356 (2018) 150-158.

[43] S. Mohan, B. Subramanian, G. Sarveswaran, A prototypical development of plasmonic multiferroic bismuth ferrite particulate and fiber nanostructures and their remarkable photocatalytic activity under sunlight, Journal of Materials Chemistry C, 2 (2014) 6835-6842.

[44] M.R. Khan, T.W. Chuan, A. Yousuf, M. Chowdhury, C.K. Cheng, Schottky barrier and surface plasmonic resonance phenomena towards the photocatalytic reaction: study of their mechanisms to enhance photocatalytic activity, Catalysis Science & Technology, 5 (2015) 2522-2531.

[45] J. Fang, W. Wang, C. Zhu, L. Fang, J. Jin, Y. Ni, C. Lu, Z. Xu, CdS/Pt photocatalytic activity boosted by high-energetic photons based on efficient triplet-triplet annihilation upconversion, Applied Catalysis B: Environmental, 217 (2017) 100-107.

[46] T. Cai, L. Wang, Y. Liu, S. Zhang, W. Dong, H. Chen, X. Yi, J. Yuan, X. Xia, C. Liu, Ag_3PO_4/Ti_3C_2 MXene interface materials as a Schottky catalyst with enhanced photocatalytic activities and anti-photocorrosion performance, Applied Catalysis B: Environmental, 239 (2018) 545-554.

[47] E. Jiang, X. Liu, H. Che, C. Liu, H. Dong, G. Che, Visible-light-driven Ag/Bi_3O_4Cl nanocomposite photocatalyst with enhanced photocatalytic activity for degradation of tetracycline, RSC Advances, 8 (2018) 37200-37207.

[48] C. Wang, Y. Wu, J. Lu, J. Zhao, J. Cui, X. Wu, Y. Yan, P. Huo, Bioinspired synthesis of photocatalytic nanocomposite membranes based on synergy of Au-TiO_2 and polydopamine for degradation of tetracycline under visible light, ACS Applied Materials & Interfaces, 9 (2017) 23687-23697.

[49] W. Zhu, J. Liu, S. Yu, Y. Zhou, X. Yan, Ag loaded WO_3 nanoplates for efficient photocatalytic degradation of sulfanilamide and their bactericidal effect under visible light irradiation, Journal of Hazardous Materials, 318 (2016) 407-416.

[50] B. Luo, D. Xu, D. Li, G. Wu, M. Wu, W. Shi, M. Chen, Fabrication of a Ag/Bi_3TaO_7 plasmonic photocatalyst with enhanced photocatalytic activity for degradation of tetracycline, ACS Applied Materials & Interfaces, 7 (2015) 17061-17069.

[51] J. Xue, S. Ma, Y. Zhou, Z. Zhang, M. He, Facile photochemical synthesis of Au/Pt/g-C_3N_4 with plasmon-enhanced photocatalytic activity for antibiotic degradation, ACS applied materials & interfaces, 7 (2015) 9630-9637.

[52] H. Li, Y. Zhou, W. Tu, J. Ye, Z. Zou, State-of-the-art progress in diverse heterostructured photocatalysts toward promoting photocatalytic performance, Advanced Functional Materials, 25 (2015) 998-1013.

[53] H. Wang, L. Zhang, Z. Chen, J. Hu, S. Li, Z. Wang, J. Liu, X. Wang, Semiconductor heterojunction photocatalysts: design, construction, and photocatalytic performances, Chemical Society Reviews, 43 (2014) 5234-5244.

[54] L. Li, P.A. Salvador, G.S. Rohrer, Photocatalysts with internal electric fields, Nanoscale, 6 (2014) 24-42.

[55] F. Guo, W. Shi, H. Wang, M. Han, H. Li, H. Huang, Y. Liu, Z. Kang, Facile fabrication of a CoO/g-C_3N_4 p-n heterojunction with enhanced photocatalytic activity and stability for

tetracycline degradation under visible light, Catalysis Science & Technology, 7 (2017) 3325-3331.

[56] C. Lai, M. Zhang, B. Li, D. Huang, G. Zeng, L. Qin, X. Liu, H. Yi, M. Cheng, L. Li, Fabrication of CuS/$BiVO_4$ (0 4 0) binary heterojunction photocatalysts with enhanced photocatalytic activity for ciprofloxacin degradation and mechanism insight, Chemical Engineering Journal, 358 (2019) 891-902.

[57] P. Mondal, J. Satra, U.K. Ghorui, N. Saha, D.N. Srivastava, B. Adhikary, Facile fabrication of novel hetero-structured organic-inorganic high-performance nanocatalyst: a smart system for enhanced catalytic activity toward ciprofloxacin degradation and oxygen reduction, ACS Applied Nano Materials, 1 (2018) 6015-6026.

[58] P. Zhou, J. Yu, M. Jaroniec, All-solid-state Z-scheme photocatalytic systems, Advanced Materials, 26 (2014) 4920-4935.

[59] J. Low, C. Jiang, B. Cheng, S. Wageh, A.A. Al-Ghamdi, J. Yu, A review of direct Z-scheme photocatalysts, Small Methods, 1 (2017) 1700080.

[60] X. Hu, X. Liu, J. Tian, Y. Li, H. Cui, Towards full-spectrum (UV, visible, and near-infrared) photocatalysis: achieving an all-solid-state Z-scheme between Ag_2O and TiO_2 using reduced graphene oxide as the electron mediator, Catalysis Science & Technology, 7 (2017) 4193-4205.

[61] Z. Pan, W. Ma, L. Wang, Construction of a magnetic Z-scheme photocatalyst with enhanced oxidation/reduction abilities and recyclability for the degradation of tetracycline, RSC Advances, 6 (2016) 114374-114382.

[62] K. Wang, J. Li, G. Zhang, Ag-bridged Z-scheme 2D/2D $Bi_5FeTi_3O_{15}$/g-C_3N_4 heterojunction for enhanced photocatalysis: mediator-induced interfacial charge transfer and mechanism insights, ACS applied materials & interfaces, 11 (2019) 27686-27696.

[63] X. Lu, W. Che, X. Hu, Y. Wang, A. Zhang, F. Deng, S. Luo, D.D. Dionysiou, The facile fabrication of novel visible-light-driven Z-scheme $CuInS_2$/Bi_2WO_6 heterojunction with intimate interface contact by in situ hydrothermal growth strategy for extraordinary photocatalytic performance, Chemical Engineering Journal, 356 (2019) 819-829.

[64] W.-K. Jo, T. Sivakumar Natarajan, Facile synthesis of novel redox-mediator-free direct Z-scheme $CaIn_2S_4$ marigold-flower-like/TiO_2 photocatalysts with superior photocatalytic efficiency, ACS Applied Materials & Interfaces, 7 (2015) 17138-17154.

[65] C. Li, S. Yu, H. Che, X. Zhang, J. Han, Y. Mao, Y. Wang, C. Liu, H. Dong, Fabrication of Z-scheme heterojunction by anchoring mesoporous γ-Fe_2O_3 nanospheres on g-C_3N_4 for

degrading tetracycline hydrochloride in water, ACS Sustainable Chemistry & Engineering, 6 (2018) 16437-16447.

[66] Q. Xiang, J. Yu, M. Jaroniec, Graphene-based semiconductor photocatalysts, Chemical Society Reviews, 41 (2012) 782-796.

[67] S.J. Phang, L.-L. Tan, Recent advances in carbon quantum dot (CQD)-based two dimensional materials for photocatalytic applications, Catalysis Science & Technology, 9 (2019) 5882-5905.

[68] W. Zhao, Y. Wang, Y. Yang, J. Tang, Y. Yang, Carbon spheres supported visible-light-driven CuO-$BiVO_4$ heterojunction: preparation, characterization, and photocatalytic properties, Applied Catalysis B: Environmental, 115 (2012) 90-99.

[69] X. Li, J. Yu, S. Wageh, A.A. Al-Ghamdi, J. Xie, Graphene in photocatalysis: a review, Small, 12 (2016) 6640-6696.

[70] Q. Xiang, B. Cheng, J. Yu, Graphene-based photocatalysts for solar-fuel generation, Angewandte Chemie International Edition, 54 (2015) 11350-11366.

[71] K. Chakraborty, T. Pal, S. Ghosh, RGO-ZnTe: a graphene based composite for tetracycline degradation and their synergistic effect, ACS Applied Nano Materials, 1 (2018) 3137-3144.

[72] W. Fan, Z. Zhu, Y. Yu, Z. Liu, C. Li, P. Huo, Y. Qiu, Y. Yan, Fabrication of magnetic g-C_3N_4 for effectively enhanced tetracycline degradation with RGO as mediator, New Journal of Chemistry, 42 (2018) 15974-15984.

[73] S. Zhang, J. Xu, J. Hu, C. Cui, H. Liu, Interfacial growth of TiO_2-rGO composite by pickering emulsion for photocatalytic degradation, Langmuir, 33 (2017) 5015-5024.

[74] Y.-Y. Bai, F.-R. Wang, J.-K. Liu, A new complementary catalyst and catalytic mechanism: Ag_2MoO_4/Ag/AgBr/GO heterostructure, Industrial & Engineering Chemistry Research, 55 (2016) 9873-9879.

[75] S. Sharma, A. Umar, S.K. Mehta, A.O. Ibhadon, S.K. Kansal, Solar light driven photocatalytic degradation of levofloxacin using TiO_2/carbon-dot nanocomposites, New Journal of Chemistry, 42 (2018) 7445-7456.

[76] W. Liu, Y. Li, F. Liu, W. Jiang, D. Zhang, J. Liang, Visible-light-driven photocatalytic degradation of diclofenac by carbon quantum dots modified porous g-C_3N_4: mechanisms, degradation pathway and DFT calculation, Water Research, 150 (2019) 431-441.

[77] Y. Wang, F. Wang, Y. Feng, Z. Xie, Q. Zhang, X. Jin, H. Liu, Y. Liu, W. Lv, G. Liu, Facile synthesis of carbon quantum dots loaded with mesoporous g-C_3N_4 for synergistic absorption and visible light photodegradation of fluoroquinolone antibiotics, Dalton Transactions, 47 (2018) 1284-1293.

[78] J. Di, J. Xia, M. Ji, H. Li, H. Xu, H. Li, R. Chen, The synergistic role of carbon quantum dots for the improved photocatalytic performance of Bi_2MoO_6, Nanoscale, 7 (2015) 11433-11443.

[79] Z. Li, L. Zhu, W. Wu, S. Wang, L. Qiang, Highly efficient photocatalysis toward tetracycline under simulated solar-light by Ag^+-CDs-Bi_2WO_6: synergistic effects of silver ions and carbon dots, Applied Catalysis B: Environmental, 192 (2016) 277-285.

[80] F. Ming, J. Hong, X. Xu, Z. Wang, Dandelion-like ZnS/carbon quantum dots hybrid materials with enhanced photocatalytic activity toward organic pollutants, RSC Advances, 6 (2016) 31551-31558.

[81] A.M. Huerta-Flores, D. Sánchez-Martínez, M. del Rocío Hernández-Romero, M.E. Zarazúa-Morín, L.M. Torres-Martínez, Visible-light-driven $BaBiO_3$ perovskite photocatalysts: effect of physicochemical properties on the photoactivity towards water splitting and the removal of rhodamine B from aqueous systems, Journal of Photochemistry and Photobiology A: Chemistry, 368 (2019) 70-77.

[82] C. Dong, S. Lu, S. Yao, R. Ge, Z. Wang, Z. Wang, P. An, Y. Liu, B. Yang, H. Zhang, Colloidal synthesis of ultrathin monoclinic $BiVO_4$ nanosheets for Z-scheme overall water splitting under visible light, ACS Catalysis, 8 (2018) 8649-8658.

[83] Y. Zhou, Y. Zhang, M. Lin, J. Long, Z. Zhang, H. Lin, J.C.-S. Wu, X. Wang, Monolayered Bi_2WO_6 nanosheets mimicking heterojunction interface with open surfaces for photocatalysis, Nature communications, 6 (2015) 1-8.

[84] J. Tang, Z. Zou, J. Ye, Efficient photocatalysis on $BaBiO_3$ driven by visible light, The Journal of Physical Chemistry C, 111 (2007) 12779-12785.

[85] K. Rokesh, M. Sakar, T.-O. Do, Calcium bismuthate ($CaBiO_3$): a potential sunlight-driven perovskite photocatalyst for the degradation of emerging pharmaceutical contaminants, ChemPhotoChem, 4(5) (2020) 373-380.

[86] Y. Sun, C. Wu, R. Long, Y. Cui, S. Zhang, Y. Xie, Synthetic loosely packed monoclinic $BiVO_4$ nanoellipsoids with novel multiresponses to visible light, trace gas and temperature, Chemical communications, (2009) 4542-4544.

[87] J.K. Cooper, S. Gul, F.M. Toma, L. Chen, P.-A. Glans, J. Guo, J.W. Ager, J. Yano, I.D. Sharp, Electronic structure of monoclinic $BiVO_4$, Chemistry of Materials, 26 (2014) 5365-5373.

[88] S. Sun, W. Wang, D. Li, L. Zhang, D. Jiang, Solar light driven pure water splitting on quantum sized $BiVO_4$ without any cocatalyst, ACS Catalysis, 4 (2014) 3498-3503.

[89] G. Xi, J. Ye, Synthesis of bismuth vanadate nanoplates with exposed {001} facets and enhanced visible-light photocatalytic properties, Chemical Communications, 46 (2010) 1893-1895.

[90] N. Zhang, R. Ciriminna, M. Pagliaro, Y.-J. Xu, Nanochemistry-derived Bi_2WO_6 nanostructures: towards production of sustainable chemicals and fuels induced by visible light, Chemical Society Reviews, 43 (2014) 5276-5287.

[91] C. Li, G. Chen, J. Sun, J. Rao, Z. Han, Y. Hu, Y. Zhou, A novel mesoporous single-crystal-like Bi_2WO_6 with enhanced photocatalytic activity for pollutants degradation and oxygen production, ACS applied materials & interfaces, 7 (2015) 25716-25724.

[92] T. Schwartz, W. Kohnen, B. Jansen, U. Obst, Detection of antibiotic-resistant bacteria and their resistance genes in wastewater, surface water, and drinking water biofilms, FEMS microbiology ecology, 43 (2003) 325-335.

[93] R. Anjali, S. Shanthakumar, Insights on the current status of occurrence and removal of antibiotics in wastewater by advanced oxidation processes, Journal of environmental management, 246 (2019) 51-62.

[94] M.B. Ahmed, J.L. Zhou, H.H. Ngo, W. Guo, Adsorptive removal of antibiotics from water and wastewater: progress and challenges, Science of the Total Environment, 532 (2015) 112-126.

[95] S.-R. Zhu, Q. Qi, Y. Fang, W.-N. Zhao, M.-K. Wu, L. Han, Covalent triazine framework modified BiOBr nanoflake with enhanced photocatalytic activity for antibiotic removal, Crystal Growth & Design, 18 (2017) 883-891.

[96] H. Fujito, H. Kunioku, D. Kato, H. Suzuki, M. Higashi, H. Kageyama, R. Abe, Layered perovskite oxychloride Bi_4NbO_8Cl: a stable visible light responsive photocatalyst for water splitting, Journal of the American Chemical Society, 138 (2016) 2082-2085.

[97] N.N. Vu, C.C. Nguyen, S. Kaliaguine, T.O. Do, Reduced Cu/Pt-$HCa_2Ta_3O_{10}$ perovskite nanosheets for sunlight-driven conversion of CO_2 into valuable fuels, Advanced Sustainable Systems, 1 (2017) 1700048.

[98] R. Hailili, Z.-Q. Wang, Y. Li, Y. Wang, V.K. Sharma, X.-Q. Gong, C. Wang, Oxygen vacancies induced visible-light photocatalytic activities of $CaCu_3Ti_4O_{12}$ with controllable morphologies for antibiotic degradation, Applied Catalysis B: Environmental, 221 (2018) 422-432.

[99] R. Hailili, Z.-Q. Wang, M. Xu, Y. Wang, X.-Q. Gong, T. Xu, C. Wang, Layered nanostructured ferroelectric perovskite $Bi_5FeTi_3O_{15}$ for visible light photodegradation of antibiotics, Journal of Materials Chemistry A, 5 (2017) 21275-21290.

[100] S. Tu, H. Huang, T. Zhang, Y. Zhang, Controllable synthesis of multi-responsive ferroelectric layered perovskite-like $Bi_4Ti_3O_{12}$: photocatalysis and piezoelectric-catalysis and mechanism insight, Applied Catalysis B: Environmental, 219 (2017) 550-562.

[101] P. Kanhere, Z. Chen, A review on visible light active perovskite-based photocatalysts, Molecules, 19 (2014) 19995-20022.

[102] T. Takei, R. Haramoto, Q. Dong, N. Kumada, Y. Yonesaki, N. Kinomura, T. Mano, S. Nishimoto, Y. Kameshima, M. Miyake, Photocatalytic activities of various pentavalent bismuthates under visible light irradiation, Journal of Solid State Chemistry, 184 (2011) 2017-2022.

[103] T. Kako, Z. Zou, M. Katagiri, J. Ye, Decomposition of organic compounds over $NaBiO_3$ under visible light irradiation, Chemistry of materials, 19 (2007) 198-202.

[104] H. Zheng, T. Zhang, Y. Zhu, B. Liang, W. Jiang, $KBiO_3$ as an effective visible-light-driven photocatalyst: degradation mechanism for different organic pollutants, ChemPhotoChem, 2 (2018) 442-449.

[105] X. Yu, J. Zhou, Z. Wang, W. Cai, Preparation of visible light-responsive $AgBiO_3$ bactericide and its control effect on the Microcystis aeruginosa, Journal of Photochemistry and Photobiology B: Biology, 101 (2010) 265-270.

[106] K. Foyevtsova, A. Khazraie, I. Elfimov, G.A. Sawatzky, Hybridization effects and bond disproportionation in the bismuth perovskites, Physical Review B, 91 (2015) 121114.

[107] Y. Ding, G. Zhang, X. Wang, L. Zhu, H. Tang, Chemical and photocatalytic oxidative degradation of carbamazepine by using metastable Bi^{3+} self-doped $NaBiO_3$ nanosheets as a bifunctional material, Applied Catalysis B: Environmental, 202 (2017) 528-538.

[108] J. Ge, W.-J. Yin, Y. Yan, Solution-processed Nb-substituted $BaBiO_3$ double perovskite thin films for photoelectrochemical water reduction, Chemistry of Materials, 30 (2018) 1017-1031.

[109] T. Zhang, Y. Ding, H. Tang, Generation of singlet oxygen over Bi (V)/Bi (III) composite and its use for oxidative degradation of organic pollutants, Chemical Engineering Journal, 264 (2015) 681-689.

[110] Y. Ding, F. Yang, L. Zhu, N. Wang, H. Tang, Bi^{3+} self doped $NaBiO_3$ nanosheets: facile controlled synthesis and enhanced visible light photocatalytic activity, Applied Catalysis B: Environmental, 164 (2015) 151-158.

[111] J. He, C. Franchini, J.M. Rondinelli, Ferroelectric oxides with strong visible-light absorption from charge ordering, Chemistry of Materials, 29 (2017) 2445-2451.

[112] J. Kim, X. Chen, P.-C. Shih, H. Yang, Porous perovskite-type lanthanum cobaltite as electrocatalysts toward oxygen eevolution reaction, ACS Sustainable Chemistry & Engineering, 5 (2017) 10910-10917.

[113] A. Walsh, Y. Yan, M.N. Huda, M.M. Al-Jassim, S.-H. Wei, Band edge electronic structure of $BiVO_4$: elucidating the role of the Bi s and V d orbitals, Chemistry of Materials, 21 (2009) 547-551.

[114] X. Chang, G. Yu, J. Huang, Z. Li, S. Zhu, P. Yu, C. Cheng, S. Deng, G. Ji, Enhancement of photocatalytic activity over $NaBiO_3$/BiOCl composite prepared by an in situ formation strategy, Catalysis Today, 153 (2010) 193-199.

[115] X. Chang, J. Huang, C. Cheng, W. Sha, X. Li, G. Ji, S. Deng, G. Yu, Photocatalytic decomposition of 4-t-octylphenol over $NaBiO_3$ driven by visible light: catalytic kinetics and corrosion products characterization, Journal of Hazardous Materials, 173 (2010) 765-772.

[116] N. Kumar, S.L. Golledge, D.P. Cann, Synthesis and electrical properties of $BaBiO_3$ and high resistivity $BaTiO_3$-$BaBiO_3$ ceramics, Journal of Advanced Dielectrics, 06 (2016) 1650032.

[117] K. Rokesh, M. Sakar, T.-O. Do, 2-(aminomethyl pyridine)SbI_5: an emerging visible-light driven organic-inorganic hybrid perovskite for photoelectrochemical and photocatalytic applications, Materials Letters, 242 (2019) 99-102.

[118] A. Bhatia, G. Hautier, T. Nilgianskul, A. Miglio, J. Sun, H.J. Kim, K.H. Kim, S. Chen, G.-M. Rignanese, X. Gonze, J. Suntivich, High-mobility bismuth-based transparent p-type oxide from high-throughput material screening, Chemistry of Materials, 28 (2016) 30-34.

[119] K. Wang, G. Zhang, J. Li, Y. Li, X. Wu, 0D/2D Z-scheme heterojunctions of bismuth tantalate quantum dots/ultrathin g-C_3N_4 nanosheets for highly efficient visible light photocatalytic degradation of antibiotics, ACS applied materials & interfaces, 9 (2017) 43704-43715.

[120] B. Ji, J. Zhang, C. Zhang, N. Li, T. Zhao, F. Chen, L. Hu, S. Zhang, Z. Wang, Vertically aligned ZnO@ZnS nanorod chip with improved photocatalytic activity for antibiotics degradation, ACS Applied Nano Materials, 1 (2018) 793-799.

[121] S. Subudhi, S. Mansingh, G. Swain, A. Behera, D. Rath, K. Parida, HPW-anchored UiO-66 metal-organic framework: a promising photocatalyst effective toward tetracycline hydrochloride degradation and H_2 evolution via Z-scheme charge dynamics, Inorganic Chemistry, 58 (2019) 4921-4934.

[122] J. Di, J. Xia, M. Ji, S. Yin, H. Li, H. Xu, Q. Zhang, H. Li, Controllable synthesis of $Bi_4O_5Br_2$ ultrathin nanosheets for photocatalytic removal of ciprofloxacin and mechanism insight, Journal of Materials Chemistry A, 3 (2015) 15108-15118.

[123] J. Sun, H. Xu, D. Li, Z. Zou, Q. Wu, G. Liu, J. Yang, L. Sun, D. Xia, Ultrasound-assisted synthesis of a feathery-shaped BiOCl with abundant oxygen vacancies and efficient visible-light photoactivity, New Journal of Chemistry, 42 (2018) 19571-19577.

[124] S. Yin, T. Wu, M. Li, J. Di, M. Ji, B. Wang, Y. Chen, J. Xia, H. Li, Controllable synthesis of perovskite-like $PbBiO_2Cl$ hollow microspheres with enhanced photocatalytic activity for antibiotic removal, CrystEngComm, 19 (2017) 4777-4788.

[125] W. Wang, P. Xu, M. Chen, G. Zeng, C. Zhang, C. Zhou, Y. Yang, D. Huang, C. Lai, M. Cheng, L. Hu, W. Xiong, H. Guo, M. Zhou, Alkali metal-assisted synthesis of graphite carbon nitride with tunable band-gap for enhanced visible-light-driven photocatalytic performance, ACS Sustainable Chemistry & Engineering, 6 (2018) 15503-15516.

[126] J. Hou, D. Dai, R. Wei, X. Wu, X. Wang, M. Tahir, J.-J. Zou, Narrowing the band gap of BiOCl for the hydroxyl radical generation of photocatalysis under visible light, ACS Sustainable Chemistry & Engineering, 7 (2019) 16569-16576.

[127] A. Dehghan, M.H. Dehghani, R. Nabizadeh, N. Ramezanian, M. Alimohammadi, A.A. Najafpoor, Adsorption and visible-light photocatalytic degradation of tetracycline hydrochloride from aqueous solutions using 3D hierarchical mesoporous BiOI: synthesis and characterization, process optimization, adsorption and degradation modeling, Chemical Engineering Research and Design, 129 (2018) 217-230.

[128] Y. Deng, L. Tang, C. Feng, G. Zeng, J. Wang, Y. Lu, Y. Liu, J. Yu, S. Chen, Y. Zhou, Construction of plasmonic Ag and nitrogen-doped graphene quantum dots codecorated ultrathin graphitic carbon nitride nanosheet composites with enhanced photocatalytic activity: full-spectrum response ability and mechanism insight, ACS Applied Materials & Interfaces, 9 (2017) 42816-42828.

[129] A.M. Huerta-Flores, D. Sanchez-Martinez, M. del Rocío Hernández-Romero, M.E. Zarazúa-Morín, L.M. Torres-Martínez, Visible-light-driven $BaBiO_3$ perovskite photocatalysts: effect of physicochemical properties on the photoactivity towards water splitting and the removal of rhodamine B from aqueous systems, Journal of Photochemistry and Photobiology A: Chemistry, 368 (2019) 70-77.

[130] K. Yu, S. Yang, H. He, C. Sun, C. Gu, Y. Ju, Visible light-driven photocatalytic degradation of rhodamine B over $NaBiO_3$: pathways and mechanism, The Journal of Physical Chemistry A, 113 (2009) 10024-10032.

[131] R. Ramachandran, M. Sathiya, K. Ramesha, A. Prakash, G. Madras, A. Shukla, Photocatalytic properties of $KBiO_3$ and $LiBiO_3$ with tunnel structures, Journal of Chemical Sciences, 123 (2011) 517-524.

[132] M.E. de Kraker, A.J. Stewardson, S. Harbarth, Will 10 million people die a year due to antimicrobial resistance by 2050?, PLoS medicine, 13 (2016) e1002184.

[133] J. Yu, Y. Kang, W. Yin, J. Fan, Z. Guo, Removal of antibiotics from aqueous solutions by a carbon adsorbent derived from protein-waste-doped biomass, ACS Omega, 5 (2020) 19187-19193.

[134] K.-J. Choi, S.-G. Kim, S.-H. Kim, Removal of antibiotics by coagulation and granular activated carbon filtration, Journal of Hazardous Materials, 151 (2008) 38-43.

[135] F. Polesel, H.R. Andersen, S. Trapp, B.G. Plósz, Removal of antibiotics in biological wastewater treatment systems-a critical assessment using the activated sludge modeling framework for xenobiotics (ASM-X), Environmental Science & Technology, 50 (2016) 10316-10334.

[136] R. Kaur, J.P. Kushwaha, N. Singh, Electro-catalytic oxidation of ofloxacin antibiotic in continuous reactor: evaluation, transformation products and pathway, Journal of The Electrochemical Society, 166 (2019) H250.

[137] K. Rokesh, M. Sakar, T.-O. Do, Emerging hybrid nanocomposite photocatalysts for the degradation of antibiotics: insights into their designs and mechanisms, Nanomaterials, 11 (2021) 572.

[138] S. Dong, J. Feng, M. Fan, Y. Pi, L. Hu, X. Han, M. Liu, J. Sun, J. Sun, Recent developments in heterogeneous photocatalytic water treatment using visible light-responsive photocatalysts: a review, RSC Advances, 5 (2015) 14610-14630.

[139] S.N. Ahmed, W. Haider, Heterogeneous photocatalysis and its potential applications in water and wastewater treatment: a review, Nanotechnology, 29 (2018) 342001.

[140] S. Wang, L. Wang, W. Huang, Bismuth-based photocatalysts for solar energy conversion, Journal of Materials Chemistry A, (2020).

[141] S. Gao, B. Gu, X. Jiao, Y. Sun, X. Zu, F. Yang, W. Zhu, C. Wang, Z. Feng, B. Ye, Y. Xie, Highly efficient and exceptionally durable CO_2 photoreduction to methanol over freestanding defective single-unit-cell bismuth vanadate layers, Journal of the American Chemical Society, 139 (2017) 3438-3445.

[142] B. Yuan, R. Chong, B. Zhang, J. Li, Y. Liu, C. Li, Photocatalytic aerobic oxidation of amines to imines on $BiVO_4$ under visible light irradiation, Chemical Communications, 50 (2014) 15593-15596.

[143] T. Wang, C. Li, J. Ji, Y. Wei, P. Zhang, S. Wang, X. Fan, J. Gong, Reduced graphene oxide (rGO)/$BiVO_4$ composites with maximized interfacial coupling for visible light photocatalysis, ACS Sustainable Chemistry & Engineering, 2 (2014) 2253-2258.

[144] H. Hirakawa, S. Shiota, Y. Shiraishi, H. Sakamoto, S. Ichikawa, T. Hirai, Au nanoparticles supported on $BiVO_4$: effective inorganic photocatalysts for H_2O_2 production from water and O_2 under visible light, ACS Catalysis, 6 (2016) 4976-4982.

[145] J. Bian, J. Feng, Z. Zhang, Z. Li, Y. Zhang, Y. Liu, S. Ali, Y. Qu, L. Bai, J. Xie, Dimension-matched zinc phthalocyanine/$BiVO_4$ ultrathin nanocomposites for CO_2 reduction as efficient wide-visible-light-driven photocatalysts via a cascade charge transfer, Angewandte Chemie International Edition, 58 (2019) 10873-10878.

[146] S. Zhu, T. Xu, H. Fu, J. Zhao, Y. Zhu, Synergetic effect of Bi_2WO_6 photocatalyst with C_{60} and enhanced photoactivity under visible irradiation, Environmental science & technology, 41 (2007) 6234-6239.

[147] H. Fu, T. Xu, S. Zhu, Y. Zhu, Photocorrosion inhibition and enhancement of photocatalytic activity for ZnO via hybridization with C_{60}, Environmental science & technology, 42 (2008) 8064-8069.

[148] Y. Pan, X. Liu, W. Zhang, Z. Liu, G. Zeng, B. Shao, Q. Liang, Q. He, X. Yuan, D. Huang, Advances in photocatalysis based on fullerene C_{60} and its derivatives: properties, mechanism, synthesis, and applications, Applied Catalysis B: Environmental, 265 (2020) 118579.

[149] J. Lee, S. Hong, Y. Mackeyev, C. Lee, E. Chung, L.J. Wilson, J.-H. Kim, P.J. Alvarez, Photosensitized oxidation of emerging organic pollutants by tetrakis C_{60} aminofullerene-derivatized silica under visible light irradiation, Environmental science & technology, 45 (2011) 10598-10604.

[150] W. Whitnall, L. Cademartiri, G.A. Ozin, C_{60}-PMO: periodic mesoporous buckyballsilica, Journal of the American Chemical Society, 129 (2007) 15644-15649.

[151] Z. Lian, P. Xu, W. Wang, D. Zhang, S. Xiao, X. Li, G. Li, C_{60}-decorated CdS/TiO_2 mesoporous architectures with enhanced photostability and photocatalytic activity for H_2 evolution, ACS applied materials & interfaces, 7 (2015) 4533-4540.

[152] J. Yu, T. Ma, G. Liu, B. Cheng, Enhanced photocatalytic activity of bimodal mesoporous titania powders by C_{60} modification, Dalton Transactions, 40 (2011) 6635-6644.

[153] Q. Yuan, L. Chen, M. Xiong, J. He, S.-L. Luo, C.-T. Au, S.-F. Yin, Cu_2O/$BiVO_4$ heterostructures: synthesis and application in simultaneous photocatalytic oxidation of organic dyes and reduction of Cr(VI) under visible light, Chemical Engineering Journal, 255 (2014) 394-402.

[154] Z. Jiang, Y. Liu, T. Jing, B. Huang, X. Zhang, X. Qin, Y. Dai, M.-H. Whangbo, Enhancing the photocatalytic activity of $BiVO_4$ for oxygen evolution by Ce doping: Ce^{3+} ions as hole traps, The Journal of Physical Chemistry C, 120 (2016) 2058-2063.

[155] N.N. Rabin, M.R. Karim, M.S. Islam, H. Omagari, N. Kameda, Y. Shudo, R. Ohtani, M. Nakamura, S. Hayami, Oxidation route dependent proton conductivities of oxidized fullerenes, New Journal of Chemistry, 41 (2017) 14708-14712.

[156] U. García-Pérez, S. Sepúlveda-Guzmán, A. Martínez-De La Cruz, Nanostructured $BiVO_4$ photocatalysts synthesized via a polymer-assisted coprecipitation method and their photocatalytic properties under visible-light irradiation, Solid state sciences, 14 (2012) 293-298.

[157] B. Chai, X. Liao, F. Song, H. Zhou, Fullerene modified C_3N_4 composites with enhanced photocatalytic activity under visible light irradiation, Dalton Transactions, 43 (2014) 982-989.

[158] P. Prasad, K.S. Prasad, N. Thakur, FTIR signatures of type-II clathrates of carbon dioxide in natural quartz veins, Current science, (2006) 1544-1547.

[159] Y. Geng, P. Zhang, S. Kuang, Fabrication and enhanced visible-light photocatalytic activities of $BiVO_4$/Bi_2WO_6 composites, RSC Advances, 4 (2014) 46054-46059.

[160] S. Sun, W. Wang, L. Zhang, E. Gao, D. Jiang, Y. Sun, Y. Xie, Ultrathin {001}-oriented bismuth tungsten oxide nanosheets as highly efficient photocatalysts, ChemSusChem, 6 (2013) 1873-1877.

[161] X.a. Dong, W. Zhang, W. Cui, Y. Sun, H. Huang, Z. Wu, F. Dong, Pt quantum dots deposited on N-doped $(BiO)_2CO_3$: enhanced visible light photocatalytic NO removal and reaction pathway, Catalysis Science & Technology, 7 (2017) 1324-1332.

[162] Q. Cai, Z. Hu, Q. Zhang, B. Li, Z. Shen, Fullerene (C_{60})/CdS nanocomposite with enhanced photocatalytic activity and stability, Applied Surface Science, 403 (2017) 151-158.

[163] M. Zhou, K. Hou, Solution-processable ZnO/3-aminopropyltriethoxysilane hybrid cathode interlayer for non-fullerene organic solar cells, Thin Solid Films, 692 (2019) 137577.

[164] Q. Li, Z. Guan, D. Wu, X. Zhao, S. Bao, B. Tian, J. Zhang, Z-scheme BiOCl-Au-CdS heterostructure with enhanced sunlight-driven photocatalytic activity in degrading water dyes and antibiotics, ACS Sustainable Chemistry & Engineering, 5 (2017) 6958-6968.

[165] D. Long, W. Chen, X. Rao, S. Zheng, Y. Zhang, Synergetic effect of C_{60}/g-C_3N_4 nanowire composites for enhanced photocatalytic H_2 evolution under visible light irradiation, ChemCatChem, 12 (2020) 2022-2031.

[166] Y. Liu, Q. Wu, Y. Zhao, Biomimetic synthesis of Ag_3PO_4-NPs/Cu-NWs with visible-light-enhanced photocatalytic activity for degradation of the antibiotic ciprofloxacin, Dalton Transactions, 46 (2017) 6425-6432.

[167] P.V. Kamat, I. Bedja, S. Hotchandani, Photoinduced charge transfer between carbon and semiconductor clusters. one-electron reduction of C_{60} in colloidal TiO_2 semiconductor suspensions, The Journal of Physical Chemistry, 98 (1994) 9137-9142.

[168] W. Xiao, P. Zhao, S. Deng, N. Zhang, Anchoring $H_3PW_{12}O_{40}$ on 3-aminopropyltriethoxysilane modified graphene oxide: enhanced adsorption capacity and photocatalytic activity toward methyl orange, New Journal of Chemistry, 39 (2015) 3719-3727.

[169] J.W. Arbogast, A.P. Darmanyan, C.S. Foote, F.N. Diederich, R.L. Whetten, Y. Rubin, M.M. Alvarez, S.J. Anz, Photophysical properties of sixty atom carbon molecule (C_{60}), The Journal of Physical Chemistry, 95 (1991) 11-12.

[170] J. Li, Y. Ma, Z. Ye, M. Zhou, H. Wang, C. Ma, D. Wang, P. Huo, Y. Yan, Fast electron transfer and enhanced visible light photocatalytic activity using multi-dimensional components of carbon quantum dots@3D daisy-like In_2S_3/single-wall carbon nanotubes, Applied Catalysis B: Environmental, 204 (2017) 224-238.

[171] N.N. Rabin, J. Morshed, H. Akhter, M.S. Islam, M.A. Hossain, M. Elias, M.M. Alam, M.R. Karim, M.A. Hasnat, M.N. uddin, I.A. Siddiquey, Surface modification of the ZnO nanoparticles with γ-aminopropyltriethoxysilane and study of their photocatalytic activity,

optical properties and antibacterial activities, International Journal of Chemical Reactor Engineering, 14 (2016) 785-794.

[172] K. He, C. Shen, Y. Zhu, X. Chen, Z. Bi, T. Marimuthu, G. Xu, X. Xu, Stable luminescent $CsPbI_3$ quantum dots passivated by (3-aminopropyl)triethoxysilane, Langmuir, 36 (2020) 10210-10217.

[173] X. Lu, Y. Wang, X. Zhang, G. Xu, D. Wang, J. Lv, Z. Zheng, Y. Wu, NiS and MoS_2 nanosheet co-modified graphitic C_3N_4 ternary heterostructure for high efficient visible light photodegradation of antibiotic, Journal of hazardous materials, 341 (2018) 10-19.

[174] Y. Liu, Q. Wu, Y. Zhao, Biomimetic synthesis of Ag_3PO_4-NPs/Cu-NWs with visible-light-enhanced photocatalytic activity for degradation of the antibiotic ciprofloxacin, Dalton Transactions, 46 (2017) 6425-6432.

[175] K. Wang, Y. Li, G. Zhang, J. Li, X. Wu, 0D Bi nanodots/2D Bi_3NbO_7 nanosheets heterojunctions for efficient visible light photocatalytic degradation of antibiotics: enhanced molecular oxygen activation and mechanism insight, Applied Catalysis B: Environmental, 240 (2019) 39-49.

[176] C. Lai, M. Zhang, B. Li, D. Huang, G. Zeng, L. Qin, X. Liu, H. Yi, M. Cheng, L. Li, Z. Chen, L. Chen, Fabrication of CuS/$BiVO_4$ (0 4 0) binary heterojunction photocatalysts with enhanced photocatalytic activity for ciprofloxacin degradation and mechanism insight, Chemical Engineering Journal, 358 (2019) 891-902.

[177] S. Yang, D. Xu, B. Chen, B. Luo, W. Shi, In-situ synthesis of a plasmonic Ag/AgCl/Ag_2O heterostructures for degradation of ciprofloxacin, Applied Catalysis B: Environmental, 204 (2017) 602-610.

[178] C. Li, Z. Sun, W. Zhang, C. Yu, S. Zheng, Highly efficient g-C_3N_4/TiO_2/kaolinite composite with novel three-dimensional structure and enhanced visible light responding ability towards ciprofloxacin and S. aureus, Applied Catalysis B: Environmental, 220 (2018) 272-282.

[179] C. Gadipelly, A. Pérez-González, G.D. Yadav, I. Ortiz, R. Ibáñez, V.K. Rathod, K.V. Marathe, Pharmaceutical industry wastewater: review of the technologies for water treatment and reuse, Industrial & Engineering Chemistry Research, 53 (2014) 11571-11592.

[180] A. Majumdar, A. Pal, Recent advancements in visible-light-assisted photocatalytic removal of aqueous pharmaceutical pollutants, Clean Technologies and Environmental Policy, 22 (2020) 11-42.

[181] X. Yang, Z. Chen, W. Zhao, C. Liu, X. Qian, M. Zhang, G. Wei, E. Khan, Y.H. Ng, Y.S. Ok, Recent advances in photodegradation of antibiotic residues in water, Chemical Engineering Journal, (2020) 126806.

[182] A. Kaur, S.K. Kansal, Bi_2WO_6 nanocuboids: an efficient visible light active photocatalyst for the degradation of levofloxacin drug in aqueous phase, Chemical engineering journal, 302 (2016) 194-203.

[183] J. Di, J. Xia, Y. Ge, L. Xu, H. Xu, M. He, Q. Zhang, H. Li, Reactable ionic liquid-assisted rapid synthesis of BiOI hollow microspheres at room temperature with enhanced photocatalytic activity, Journal of Materials Chemistry A, 2 (2014) 15864-15874.

[184] X. Zhang, R. Li, M. Jia, S. Wang, Y. Huang, C. Chen, Degradation of ciprofloxacin in aqueous bismuth oxybromide (BiOBr) suspensions under visible light irradiation: a direct hole oxidation pathway, Chemical Engineering Journal, 274 (2015) 290-297.

[185] X. Xu, X. Ding, X. Yang, P. Wang, S. Li, Z. Lu, H. Chen, Oxygen vacancy boosted photocatalytic decomposition of ciprofloxacin over Bi_2MoO_6: oxygen vacancy engineering, biotoxicity evaluation and mechanism study, Journal of hazardous materials, 364 (2019) 691-699.

[186] M. Shang, W. Wang, H. Xu, New Bi_2WO_6 nanocages with high visible-light-driven photocatalytic activities prepared in refluxing EG, Crystal Growth and Design, 9 (2009) 991-996.

[187] T. Saison, P. Gras, N. Chemin, C. Chanéac, O. Durupthy, V. Brezova, C. Colbeau-Justin, J.-P. Jolivet, New insights into Bi_2WO_6 properties as a visible-light photocatalyst, The Journal of Physical Chemistry C, 117 (2013) 22656-22666.

[188] H. Lv, Y. Liu, J. Hu, Z. Li, Y. Lu, Ionic liquid-assisted hydrothermal synthesis of Bi_2 WO_6-reduced graphene oxide composites with enhanced photocatalytic activity, RSC Advances, 4 (2014) 63238-63245.

[189] J. Zhang, T. Chen, H. Lu, Z. Yang, F. Yin, J. Gao, Q. Liu, Y. Tu, Hierarchical Bi_2WO_6 architectures decorated with Pd nanoparticles for enhanced visible-light-driven photocatalytic activities, Applied Surface Science, 404 (2017) 282-290.

[190] J. Hu, D. Chen, Z. Mo, N. Li, Q. Xu, H. Li, J. He, H. Xu, J. Lu, Z-scheme 2D/2D heterojunction of black phosphorus/monolayer Bi_2WO_6 nanosheets with enhanced photocatalytic activities, Angewandte Chemie International Edition, 58 (2019) 2073-2077.

[191] J. Bai, X. Ren, X. Chen, P. Lu, M. Fu, Oxygen vacancy-enhanced ultrathin Bi_2O_3-Bi_2WO_6 nanosheets' photocatalytic performances under visible light irradiation, Langmuir, 37 (2021) 5049-5058.

[192] S. Yin, Y. Chen, M. Li, Q. Hu, Y. Ding, Y. Shao, J. Di, J. Xia, H. Li, Construction of NH_2-MIL-125(Ti)/Bi_2WO_6 composites with accelerated charge separation for degradation of organic contaminants under visible light irradiation, Green Energy & Environment, 5 (2020) 203-213.

[193] Q. Li, L. Li, X. Long, Y. Tu, L. Ling, J. Gu, L. Hou, Y. Xu, N. Liu, Z. Li, Rational design of MIL-88A(Fe)/Bi_2WO_6 heterojunctions as an efficient photocatalyst for organic pollutant degradation under visible light irradiation, Optical Materials, 118 (2021) 111260.

[194] Q. Wang, D. Astruc, State of the art and prospects in metal-organic framework (MOF)-based and MOF-derived nanocatalysis, Chemical reviews, 120 (2019) 1438-1511.

[195] J. Wu, X. Fang, Y. Zhu, N. Ma, W. Dai, Well-designed TiO_2@UiO-66-NH_2 nanocomposite with superior photocatalytic activity for tetracycline under restricted space, Energy & Fuels, 34 (2020) 12911-12917.

[196] S. Subudhi, G. Swain, S.P. Tripathy, K. Parida, UiO-66-NH_2 metal-organic frameworks with embedded MoS_2 nanoflakes for visible-light-mediated H_2 and O_2 evolution, Inorganic Chemistry, 59 (2020) 9824-9837.

[197] X. Zhang, Y. Yang, W. Huang, Y. Yang, Y. Wang, C. He, N. Liu, M. Wu, L. Tang, g-C_3N_4/UiO-66 nanohybrids with enhanced photocatalytic activities for the oxidation of dye under visible light irradiation, Materials Research Bulletin, 99 (2018) 349-358.

[198] J. Ding, Z. Yang, C. He, X. Tong, Y. Li, X. Niu, H. Zhang, UiO-66 (Zr) coupled with Bi_2MoO_6 as photocatalyst for visible-light promoted dye degradation, Journal of colloid and interface science, 497 (2017) 126-133.

[199] Y. Wang, L. Guo, Y. Zeng, H. Guo, S. Wan, M. Ou, S. Zhang, Q. Zhong, Amino-assisted NH_2-UiO-66 anchored on porous g-C_3N_4 for enhanced visible-light-driven CO_2 reduction, ACS Applied Materials & Interfaces, 11 (2019) 30673-30681.

[200] K. Rokesh, M. Sakar, T.-O. Do, Calcium bismuthate ($CaBiO_3$): a potential sunlight-driven perovskite photocatalyst for the degradation of emerging pharmaceutical contaminants, ChemPhotoChem, 4 (2020) 373-380.

[201] J. Wu, X. Fang, Y. Zhu, N. Ma, W. Dai, Well-designed TiO_2@UiO-66-NH_2 Nanocomposite with superior photocatalytic activity for tetracycline under restricted space, Energy & Fuels, 34 (2020) 12911-12917.

[202] L. Liang, F. Lei, S. Gao, Y. Sun, X. Jiao, J. Wu, S. Qamar, Y. Xie, Single unit cell bismuth tungstate layers realizing robust solar CO_2 reduction to methanol, Angewandte Chemie International Edition, 54 (2015) 13971-13974.

[203] X. Zhang, H. Zhou, W. Cao, C. Chen, C. Jiang, Y. Wang, Preparation and mechanism investigation of Bi_2WO_6/UiO-66-NH_2 Z-scheme heterojunction with enhanced visible light catalytic activity, Inorganic Chemistry Communications, 120 (2020) 108162.

[204] L. Liu, Y. Qi, J. Lu, S. Lin, W. An, J. Hu, Y. Liang, W. Cui, Dramatic activity of a Bi_2WO_6@gC_3N_4 photocatalyst with a core@ shell structure, RSC Advances, 5 (2015) 99339-99346.

[205] T. Yang, T. Ma, L. Yang, W. Dai, S. Zhang, S. Luo, A self-supporting UiO-66 photocatalyst with Pd nanoparticles for efficient degradation of tetracycline, Applied Surface Science, 544 (2021) 148928.

[206] S. Safa, M. Khajeh, A.R. Oveisi, R. Azimirad, Graphene quantum dots incorporated UiO-66-NH_2 as a promising photocatalyst for degradation of long-chain oleic acid, Chemical Physics Letters, 762 (2021) 138129.

[207] A. Crake, K.C. Christoforidis, A. Kafizas, S. Zafeiratos, C. Petit, CO_2 capture and photocatalytic reduction using bifunctional TiO_2/MOF nanocomposites under UV-vis irradiation, Applied Catalysis B: Environmental, 210 (2017) 131-140.

[208] M. Qamar, R.B. Elsayed, K.R. Alhooshani, M.I. Ahmed, D.W. Bahnemann, Highly efficient and selective oxidation of aromatic alcohols photocatalyzed by nanoporous hierarchical Pt/Bi_2WO_6 in organic solvent-free environment, ACS applied materials & interfaces, 7 (2015) 1257-1269.

[209] S.-Q. Wang, X.-Y. Zhang, X.-Y. Dao, X.-M. Cheng, W.-Y. Sun, Cu_2O@Cu@UiO-66-NH_2 ternary nanocubes for photocatalytic CO_2 reduction, ACS Applied Nano Materials, 3 (2020) 10437-10445.

[210] J. Meng, Q. Chen, J. Lu, H. Liu, Z-scheme photocatalytic CO_2 reduction on a heterostructure of oxygen-defective ZnO/reduced graphene oxide/UiO-66-NH_2 under visible light, ACS applied materials & interfaces, 11 (2018) 550-562.

[211] Q. Hu, Y. Chen, M. Li, Y. Zhang, B. Wang, Y. Zhao, J. Xia, S. Yin, H. Li, Construction of NH_2-UiO-66/BiOBr composites with boosted photocatalytic activity for the removal of contaminants, Colloids and Surfaces A: Physicochemical and Engineering Aspects, 579 (2019) 123625.

[212] J. Meng, Q. Chen, J. Lu, H. Liu, Z-scheme photocatalytic CO_2 reduction on a heterostructure of oxygen-defective ZnO/reduced graphene oxide/UiO-66-NH_2 under visible light, ACS Applied Materials & Interfaces, 11 (2019) 550-562.

[213] B. Shao, Z. Liu, G. Zeng, Z. Wu, Y. Liu, M. Cheng, M. Chen, Y. Liu, W. Zhang, H. Feng, Nitrogen-doped hollow mesoporous carbon spheres modified g-C_3N_4/Bi_2O_3 direct dual semiconductor photocatalytic system with enhanced antibiotics degradation under visible light, ACS Sustainable Chemistry & Engineering, 6 (2018) 16424-16436.

[214] C.-N. Ri, K. Song-Gol, J. Ju-Yong, S.-N. Pak, S.-C. Ri, J.-H. Ri, Construction of the Bi_2WO_6/$Bi_4V_2O_{11}$ heterojunction for highly efficient visible-light-driven photocatalytic reduction of Cr (vi), New Journal of Chemistry, 42 (2018) 647-653.

[215] M.B. Hussain, R. Mehmood, U. Azhar, J. Wang, L. Song, BiOCl-coated UiO-66-NH_2 metal-organic framework nanoparticles for visible-light photocatalytic Cr (VI) reduction, ACS Applied Nano Materials, 4 (2021) 4037-4047.

[216] B. Li, C. Lai, G. Zeng, L. Qin, H. Yi, D. Huang, C. Zhou, X. Liu, M. Cheng, P. Xu, Facile hydrothermal synthesis of Z-scheme $Bi_2Fe_4O_9$/Bi_2WO_6 heterojunction photocatalyst with enhanced visible light photocatalytic activity, ACS applied materials & interfaces, 10 (2018) 18824-18836.

[217] C. Zhao, Y. Li, H. Chu, X. Pan, L. Ling, P. Wang, H. Fu, C.-C. Wang, Z. Wang, Construction of direct Z-scheme Bi_5O_7I/UiO-66-NH_2 heterojunction photocatalysts for enhanced degradation of ciprofloxacin: mechanism insight, pathway analysis and toxicity evaluation, Journal of Hazardous Materials, (2021) 126466.

[218] X. Wei, C.-C. Wang, Y. Li, P. Wang, Q. Wei, The Z-scheme NH_2-UiO-66/PTCDA composite for enhanced photocatalytic Cr (VI) reduction under low-power LED visible light, Chemosphere, 280 (2021) 130734.

List of publications and presentations

Publications

1. **K. Rokesh**, M. Sakar and Trong-On Do, Amine-functionalized metal-organic framework integrated bismuth tungstate (Bi_2WO_6/NH_2-UiO-66) composite for the enhanced solar-driven photocatalytic degradation of ciprofloxacin molecules, New Journal of Chemistry **2021,** 10.1039/D1NJ03977F.

2. **K. Rokesh**, M. Sakar and Trong-On Do, Integration of aminosilicate functionalized-fullerene (C_{60}) QDs on bismuth vanadate ($BiVO_4$) nanolayers for the photocatalytic degradation of pharmaceutical pollutants, Catalysis Today **2021,** 10.1016/j.cattod.2021.10.006.

3. **K. Rokesh**, M. Sakar and Trong-On Do, Nanocomposite photocatalysts for the degradation of contaminants of emerging concerns, Springer Publisher, **2021**, 85-112.

4. **K. Rokesh**, M. Sakar and Trong-On Do, Design of photocatalysts for the degradation of emerging pharmaceutical contaminants in water, Elsevier Publisher, **2021**, 475-502.

5. **K. Rokesh**, M. Sakar and Trong-On Do, Emerging hybrid nanocomposite photocatalysts for the degradation of antibiotics: Insights into their designs and mechanisms, Nanomaterials **2021**, 11(3), 572.

6. **K. Rokesh**, M. Sakar and Trong-On Do, Calcium bismuthate ($CaBiO_3$): a potential sunlight-driven perovskite photocatalyst for the degradation of emerging pharmaceutical contaminants, ChemPhotoChem **2020,** 4(5), 373-380.

7. **K. Rokesh**, M. Sakar and Trong-On Do, 2-(aminomethyl pyridine)SbI_5: an emerging organic-inorganic hybrid perovskite for photoelectrochemical and photocatalytic applications, Materials Letters **2019**, 242, 99-102.

Conference presentation

1. **K. Rokesh** and Trong-On Do, $CaBiO_3$: a novel visible perovskite photocatalyst for the degradation of emerging pharmaceutical contaminants, 10th Annual Meeting of Centre in Green Chemistry and Catalysis (CGCC-2019), University of Montreal, Montreal, Canada, May 10th, **2019**.